2013-12-02

Formation and Analysis of Zinc Oxide Nanoparticles and Zinc Oxide Hexagonal Prisms and Optical Analysis of Cadmium Selenide Nanoparticles

Jared M. Hancock
Brigham Young University - Provo

Formation and Analysis of Zinc Oxide Nanoparticles and Zinc Oxide Hexagonal Prisms

and

Optical Analysis of Cadmium Selenide Nanoparticles

Jared Matthew Hancock

A dissertation submitted to the faculty of
Brigham Young University
in partial fulfillment of the requirements for the degree of

Doctor of Philosophy

Roger G. Harrison, Chair
Jeffrey K. Farrer
John D. Lamb
Matthew R. Linford
Richard K. Watt

Department of Chemistry and Biochemistry

Brigham Young University

August 2013

ABSTRACT

Formation and Analysis of Zinc Oxide Nanoparticles and Zinc Oxide Hexagonal Prisms

and

Optical Analysis of Cadmium Selenide Nanoparticles

Jared Matthew Hancock
Department of Chemistry and Biochemistry, BYU
Doctor of Philosophy

In this dissertation, methods to synthesize ZnO are reported. First, zinc oxide nanoparticles were synthesized with small amounts of transition metal ions to create materials called dilute magnetic semiconductors (DMS). We employed a low temperature sol-gel method that produces ZnO nanoparticles of reproducible size and incorporates cobalt, nickel, and manganese ions into the nanoparticles. Conditions were controlled such that a range of amounts of Co, Ni, and Mn were incorporated. The incorporation was tracked by color changes in the white ZnO powder to blue for Co, green for Ni and yellow for Mn. XRD measurements showed the nanoparticles were on the order of 10 nm in diameter and had a wurtzite structure. Magnetic measurements showed a change from diamagnetic to paramagnetic behavior with increasing concentration of metal dopants.

Second, formation of ZnO single crystal hexagonal prisms from a sol-gel method is presented. The method required water, zinc acetate, and ethanolamine to create a gel of zinc hydroxide and zinc hydroxide acetate, which upon heating formed single crystal hexagonal prisms. Characterization of the gel was done by XRD as well as XRD high temperature chamber (HTK) to determine the role of temperature in prism formation. SEM images showed hexagonal prisms were of uniform size (0.5 × 2 μm.) TEM and electron diffraction images showed a change from randomly oriented particles to an ordered single crystal after heating. Water and the acetate salt of zinc proved to be critical to prism formation.

Lastly, we report absorption and fluorescence properties of synthesized oligothiophenes and oligothiophene-ruthenium complexes that are bound to CdSe nanoparticles. Their ability to act as sensitizers and charge transfer junctions was tested. It was found that fluorescence of CdSe nanoparticles was quenched when they were bound to the oligothiophenes, and that the fluorescence of the oligothiophenes was also quenched. The fluorescence lifetimes of the quenched species were shortened.

Keywords: ZnO, nanoparticles, hexagonal prims, sol-gel, SEM, TEM, XRD, XRD-HTK, VSM, CdSe

ACKNOWLEDGEMENTS

I would first like to thank those in my research group that offered comments and suggestions as well as those that contributed first hand to my research. The amount of work that they have done for my project is significant. Special thanks to Trevor Smith, Brielle Woolsey, and Will Rankin for all the synthetic reactions and characterizing they preformed through the years. I also appreciate the help from those not working on my project directly, Chad Rogers, Nathan Bair, and Dave Jensen. They all helped in their own way. They convinced me a PhD was the way to go and kept me laughing and positive about my schooling.

I would like to thank my committee members for their willingness to work with me. They always had great suggestions on what could be further done to progress my projects and degree. I appreciate the help given by Jeffrey Farrer in obtaining images on the TEM microscope. A special thank you to my advisor Roger Harrison. His patience and untiring willingness to give me constructive criticism and the perfect advice was very beneficial in completing my projects. His mentoring as a teacher is invaluable.

Lastly I want to thank my parents. They are the reason I am successful in life. They have motivated me and shown me how much more I can do. And even though they were in England some of the time, they provided me with the encouragement I needed to finish.

Table of Contents

Chapter 1: Introduction

The dissertation is comprised of four chapters and an appendix. Since the main focus of the research I conducted was on zinc oxide, the first chapter is a review of zinc oxide, its properties, and ways to characterize ZnO materials. Chapter 2 describes the synthetic sol-gel method of forming ZnO nanoparticles as well as doping of nanoparticles with transition metal ions to create dilute magnetic semiconductors. Chapter 3 reports the controlled synthesis of ZnO hexagonal prisms crystal structures by adding ethanolamine to a zinc acetate solution, precipitation of a gel by adding water, and formation of prisms by heating the gel. Chapter 4 comprises the work I did on optical and fluorescent properties of oligothiophenes and cadmium selenide nanoparticles. Lastly, I've included an appendix with figures not found in the other chapters I recorded while characterizing the ZnO materials.

1.1 ZnO Structure

Zinc oxide is a widely used semiconductor found in our daily lives. From its uses in the rubber and concrete industries to food additives, pigments and UV blockers, ZnO is exploited for its optical and physical properties. ZnO has a wide direct band gap (E_g ~ 3.37 eV at 300 K) and an exciton binding energy of 60 meV. This wide band gap allows devices to operate at higher temperatures and brings the electronic transition energy into the energy range of visible light creating light emitting devices in the visible spectrum, i.e. LEDs and semiconducting lasers.

Although some zinc blende and rock salt forms are known, the most common form of ZnO is the hexagonal wurtzite structure (Figure 1). Each Zn^{2+} ion is coordinated tetrahedrally by four O^{2-} ions and likewise each O^{2-} is coordinated by four Zn^{2+} ions with

lattice constants of a = 3.25 Å and c = 5.21 Å. The ratio of c/a is 1.60, close to the ideal 1.633 for a hexagonal unit cell.

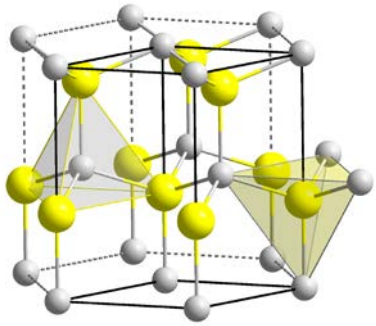

Figure 1. Wurtzite structure of ZnO showing tetrahedral arrangement of O^{2-} ions (yellow) to Zn^{2+} ions (gray).[1]

Research on semiconductor properties of ZnO has been done for decades with reports starting in 1934.[2] Because of the intrinsic properties of ZnO, it is used in a wide range of research including synthesis of nanomaterials, studies of dilute magnetic semiconductors through transition metal doping and formation of ZnO structures.

Semiconducting ZnO nanoparticles have recently gained attention and are researched for their optical properties. Another term for these types of nanoparticles is quantum dots. Quantum dots are described as semiconducting materials whose excitons are confined in all three spatial dimensions. That is, the semiconducting material has properties caused by electrons being confined in a small area. The HOMO-LUMO energy gap is larger from that seen in the bulk material. The band gap of the material can be tuned through synthetic methods. By controlling the size of the nanoparticle, the band gap is influenced, because the band gap is inversely related to the size of the nanoparticle. This has been demonstrated in the literature where changing the size of fluorescent quantum dots showed a change in the light frequency emitted upon fluorescence.[3,4] This

is referred to as interband transitions. Also, the energy levels of the electrons in the LUMO are quantized or have intraband transitions. This quantization signifies that there is no momentum transfer needed for transitions between energy levels. These transitions are typically found in the infrared region.[4]

1.2 Synthesis of ZnO Nanoparticles

In order to exploit the properties of ZnO quantum dots, various methods have been reported to synthesize ZnO nanoparticles.

1.2.1 Nanomaterial preparation methods

Nanomaterials are fabricated by two different methods, top-down and bottom-up. In top-down fabrication, micro-sized objects are used to pattern on a large scale. The size of the pattern is then reduced and nanoscale features are transferred onto the bulk material. Physical techniques, such as photolithography and mechanical stamping are used in top-down methods. The second method, bottom-up fabrication, involves forming materials by controlling the arrangement of atoms or molecules. Bottom-up methods are based on solutions or vapor phases. The bottom-up fabrication techniques include chemical vapor deposition, atomic layer deposition, physical vapor deposition, thermal evaporation, electrodeposition, hydrothermal, sol-gel, and pulsed-laser deposition.

1.2.2 Synthesis of ZnO nanoparticles

To form ZnO nanomaterials using the sol-gel method, a solvent with zinc salt is common. Alcohols are commonly used as solvent, specifically ethanol, although methanol and isopropanol are also used. Commonly, zinc acetate is added to the solvent and then a base is added. Bases are used to control the size and shape of the

nanoparticles. Bases used in synthesizing nanoparticles include inorganic bases, LiOH,[6-8] KOH,[9-12] and NaOH.[13,14] Yunbo et al. used varying concentrations of LiOH to control the size of ZnO nanoparticles.[7] LiOH solutions of 75, 29, 21, and 11.5 mM produced nanoparticles of 4.3, 5.3, 6.4, and 10.6 nm, respectively. This change in size caused a change in band gap; the nanoparticle band gap got closer to that of bulk material as the nanoparticles got larger.

Meulenkamp prepared ZnO nanoparticles with $Zn(OAc)_2 \cdot 2H_2O$ (5 mmol) dissolved in boiling absolute ethanol and then cooled to 0 °C.[6] Then, $LiOH \cdot H_2O$ (7 mmol) was dissolved in ethanol at room temperature, cooled to 0 °C and slowly added to the $Zn(OAc)_2$ solution under vigorous stirring. The reaction mixture was stored at 4 °C. The desired particle size (2.5 to 7 nm) was obtained by aging the ZnO sol at 4 °C or at room temperature.

Wong et al. prepared ZnO nanoparticles with 1 mmol of zinc acetate dissolved in 2-propanol (80 mL) under vigorous stirring at 50 °C and subsequently diluting to a total volume of 920 mL and chilling to 0 °C.[14] An 80 mL aliquot of a 20 mM NaOH solution in 2-propanol was then added to the zinc acetate solution at 0 °C within 1 min under constant stirring. The suspension was then immersed in a preheated water bath for up to 2 hours. Upon removal from the water bath, the suspension was covered and stored at room temperature. These dispersions remained transparent and stable up to a few months at which time they became translucent and a fine white precipitate eventually settled to the bottom of the container. The particles average size was 4 nm.

Organic amines, such as diethanol amine[15] and hexamethylenetetramine[16,17] have also been used to form ZnO nanoparticles. Jang et al. used a kinetically controlled

hydrothermal method to produce ZnO sub-microrods from a zinc salt and hexamethylenetetramine.[17] To control the initial seed formation reaction and suppress the high supersaturation, the Zn^{2+} concentration was restricted using a syringe pump that continuously delivered aqueous Zn^{2+} to the hot amine solution. Zinc oxide nanowires, grown along the *c* axis [0001], were made by hydrolysis of zinc nitrate by the addition of hexamethylenetetramine (< 0.1 M solutions, 5 < pH < 8, and > 80 °C) and the decomposition of zinc acetate in trioctylamine (2.66 mmol zinc acetate and 300°C).[18]

The majority of ZnO nanoparticles are made from zinc acetate. In equations 1.1–1.3, Meulenkamp shows how acetate is a good counter anion to produce ZnO in sol-gel reactions due to its ability to act as a base.[6]

$$Zn–OAc + HOH/OH^- \rightleftharpoons Zn–OH + HOAc/OAc^- \quad (1.1)$$

$$Zn–OH + Zn–OAc \rightleftharpoons Zn–O–Zn + HOAc \quad (1.2)$$

Other zinc salts, such as zinc chloride,[11] zinc citrate, and zinc nitrate[15] have also been used successfully to synthesize ZnO nanoparticles.

1.2.3 ZnO nanoparticles doped with cations

Changing the stoichiometric amounts of metal ions within a metal oxide by doping with another metal cation can lead to new and interesting properties. Dopants range from main group elements to transition metals. Doping ZnO with Cd^{2+} can decrease the band gap (E_g ~ 3.0 eV) whereas doping with Mg^{2+} can increase the band gap (E_g ~ 4.0 eV).[19]

Xiong et al. made ZnO nanoparticles using tetraethylene glycol (TEG), $Zn(C_2H_3O_2)_2 \cdot 2H_2O$, and $LiOH \cdot H_2O$ dissolved together at room temperature.[20] With ultrasonication and $Mg(C_2H_3O_2)_2 \cdot 2H_2O$ powder, Mg^{2+} was added after the original

solution became luminescent. The solution was ultrasonicated for 2 minutes, and the final solution temperature was 180 ± 10 °C. The nanoparticles were precipitated with excess ethyl acetate and dispersed in absolute ethanol. In this case the band gap was tuned from 3.4 eV to 3.8 eV. XRD showed no additional crystal structures beyond the wurtzite ZnO. The group further used inductively coupled plasma atomic emission spectroscopy (ICP-AES) to calculate the Mg/Zn ratios. The addition of $Mg(C_2H_3O_2)_2$ resulted in smaller nanoparticles, 2.5 to 3.1 nm. Also, Fourier transfrom infrared spectroscopy (FTIR) was used to confirm the formation of Zn–O–Mg bonds.

Transition metal ions are used as dopants due to their inherent optical and magnetic properties that can be added to the ZnO material. For example, to dope ZnO with Mn^{2+}, $Mn(C_2H_3O_2)_2 \cdot 4H_2O$ was dissolved in 1 mL of water. The solution was then added to isopropanol while stirring vigorously. After a few hours at room temperature, $Zn(C_2H_3O_2)_2 \cdot 2H_2O$ was added and the solution heated to 50 °C. The solution was cooled in ice and polyvinylpyrollidone was added to it. Polyvinylpryollidone caps nanoparticles and helps control their size. After stirring for a few more hours, NaOH (mixed in i-PrOH) was added dropwise and under ultrasonication. The solvent was removed by rotary evaporator and the material was washed with water to precipitate the $Zn_{1-x}Mn_xO$. Energy-dispersive X-ray spectroscopy (EDS) was used to estimate the Mn content. TEM, UV-Vis, PL, and electron paramagnetic resonance (EPR) measurements were taken. EPR showed the Mn^{2+} environment was in a tetrahedral environment, rather than in the usually preferred octahedral environment. They suggested water was the cause of the 10 nm sized particles. For when no water was used, 5.3 nm nanoparticles formed.[21]

Wurtzite ZnO is a naturally occurring *n*-type semiconductor because of

nonstoichiometric amounts of O and Zn in the crystal structure due to inherent defects such as O vacancies (V_O) and Zn interstitials (Zn_i). Although it is experimentally known that unintentionally doped ZnO is *n*-type, whether the donors are Zn_i or V_O is still being investigated.[18] *N*-type doping of ZnO is relatively easy compared to *p*-type doping. Group III elements Al, Ga, and In as substitutional elements for Zn and Group VII elements Cl and I as substitutional elements for O can be used as *n*-type dopants.[22]

ZnO with *p*-type doping is possible by substituting Zn with Group I elements (Li, Na, and K) or by substituting O with Group V elements (N, P, and As). Li can easily occupy interstitial positions in the ZnO lattice. ZnO clusters of the general formula $[MeZnOR]_4$ were used to form the ZnO for the Zn_4O_4 core.[23] The Zn_4O_4 cores were dissolved in dry THF under anaerobic conditions in Group 1 boro compounds ($LiBF_4$) for Li doping. The resulting solid was heated in pure oxygen to 750°C for 3 hours to yield the oxide powder. XRD showed the ZnO wurtzite structure. Samples with 1–3% Li were most important in *p*-type character. SEM, TEM and other methods were used to confirm Li content.

Chavillon et al. reported that the ammonolysis at temperatures under 350 ˚C of ZnO_2 nanoparticles yields pure wurtzite nitrogen doped ZnO nanoparticles with an extraordinarily large amount of Zn vacancies (up to 20%).[24] The change of ZnO_2 into ZnO generated a Zn-poor zinc oxide in which the O^{2-} and $(O_2)^{2-}$ species coexisted with nitrogen anionic species, proven by Raman spectroscopy and XPS. The combination of a high zinc vacancy concentration with nitrogen doping and the coexistence of oxide and peroxide groups lead to the stabilization of positive charge carriers. Control of the temperature was essential to access *p*-type semiconductor. Once achieved, the *p*-type

character of the nanoparticles was stable for more than 2 years.

1.2.4 ZnO as a dilute magnetic semiconductor

Above room temperature ferromagnetism, if accomplished, could form the basis for charge-based, spin-based, or mixed charge- and spin-based devices. Devices utilizing spin in one form or another are included in the area of spintronics. Spintronics refers to a situation where the spin degree of freedom of the electron is harnessed either by exploiting the spin property in conventional charge-based devices or utilizing the spin alone. For successful incorporation of spin into existing semiconductor technology several technical issues, such as efficient injection, transport, manipulation, and detection of spin polarization and spin-polarized currents must be resolved. Faster and less power-consuming transistors could be realized since flipping the spin takes 10 – 50 times less power and is ten times faster than transporting an electron through a channel in traditional field effect transistors.

Potential applications for ferromagnetic oxide semiconductors include electrically controlled magnetic sensors and actuators, high-density ultralow-power memory and logic materials, advanced optical switches and modulators, spin-polarized light emitters for optical encoding, and devices with integrated magnetic, electronic, and optical functionality.

There are two basic ideas used to understand the magnetic properties of dilute magnetic semiconductors (DMS). The first idea, which is based on general mean-field theory, assumes that the dilute magnetic semiconductor is more-or-less a random alloy. A transition-metal substitutes for one of the Zn^{2+} lattice components. The ferromagnetism occurs through interactions between the local moments of the transition metal atoms,

which are facilitated by free carriers in the material. The spin-spin coupling is also assumed to be a long-range interaction, allowing use of a mean-field approximation.

The second idea suggests that the magnetic atoms form clusters that produce the observed ferromagnetism. It is experimentally difficult to verify the mechanism responsible for the observed magnetic properties. This is due to the dependence on the growth conditions employed for growing the dilute magnetic semiconductor material. It is likely that materials consisting of single-phase random alloys, nanoclusters of the magnetic atoms, precipitates and second-phase formation, or a combination of these could be produced.

The doping of ZnO to produce dilute magnetic semiconductors started in 2002 with Gamelin.[25] Previous synthesis of DMS was confined to II – VI chalcogenides (CdS, CdSe, ZnS, and ZnSe).[26,27] A paper by Garcia et al. reported the existence of room temperature ferromagnetisim in ZnO nanoparticles due to capping with three organic molecules: tryoctylphosphine, dodecylamine, and dodecanethiol.[28] The nanoparticles were made with a sol-gel method.[29] Confirmation of the ZnO nanoparticles was done via XRD and TEM, which also confirmed the wurtzite hcp structure. Photoluminence excitation was done at 385 nm with results for the trioctylphosphine oxide (TOPO) and amine capped nanoparticles at around 550 and 575 nm, respectively. It is believed that the capping molecule alters the electronic structure of the particles. Ferromagnetic behavior was seen after substraction of the diamagnetic baseline from ZnO for the thiol and amine capped materials (2×10^{-3} μ_B and 0.5×10^{-3} μ_B for an averaged 10nm sized particle.) Identical results were shown at 5 K and 300 K.

In another study, the formation of dilute magnetic semiconductor quantum dots (DMS-QD) used DMSO as the solvent for the zinc acetate.[30] Tetramethylammonium hydroxide in ethanol was slowly added to the dissolved zinc acetate solution. Cobalt and nickel acetates were added to the DMSO solution for transition metal doping. Precipitation was achieved by the addition of ethyl acetate or heptanes. TOPO was added to docecylamine-capped nanoparticle powder with heating.

1.3 ZnO structures

ZnO exhibits a wide range of structures that can be grown by tuning the growth rates along the polar surfaces. Structurally, ZnO has three types of fast growth directions: $\langle 2\bar{1}\bar{1}0\rangle$, $\langle 01\bar{1}0\rangle$, and $\pm[0001]$.[31] A large number of nanosized structure morphologies have been formed with ZnO, these include rods,[32] wires,[33] tubes,[34] belts,[35] rings,[36] ribbons,[37] spheres,[38] tetrapods,[39] flowers,[40] and combs.[41] These morphologies result in different physical, chemical, and optical properties of ZnO.

1.3.1 Nanorods, nanowires, and nanoneedles

One-dimensional semiconductor nanowires, nanorods, or nanoneedles have attracted increasing attention due to their physical properties arising from quantum confinement. Self-organized ZnO nanowires, (0001) oriented, have been synthesized on sapphire substrates using a catalyzed vapor-phase transport process with a thin film Au catalyst.[42] The diameters of the wires range from 20 to 150 nm, with more than 95% of them having diameters of 70 – 100 nm. By adjusting the growth time, the nanowires could be grown up to 10 μm in length.

Li et al. prepared ZnO nanoneedles on a silicon wafer through chemical vapor deposition.[43] The diameters of the needle tips were in the range of 20 – 50 nm. High-

resolution TEM revealed that the nanoneedles were single crystals growing along the [0001] direction and exhibiting multiple tip surface perturbations, made of 1 – 3 nm crystals.

1.3.2 ZnO hexagonal prisms

Nanostructures are not the only structures being formed. Large crystals that are hexagonal in shape have recently been formed. Researchers have made ZnO hexagonal prisms with zinc nitrate and sodium dodecylbenzenesulfonate[44] or urea.[45] A solution of zinc acetate was also shown to form large hexagonal crystals of ZnO when paired with cetyltrimethylammonium bromide.[46] Sun et al. formed ZnO hexagonal prisms in an additive-free water solution.[47] NaOH was added to zinc nitrate to form $[Zn(OH)_4]^{2-}$ precursor complex that decompose into ZnO crystals at higher reaction temperature. Excess zinc ion caused formation of hexagonal prisms.

ZnO prisms can also be grown in solution by controlling ligand denticity. Meagley and Garcia showed that the strongest control over shape was seen with a tridentate ligand (citrate), weaker control was observed with bidentate malate, and no control was seen with the monodentate ligand (glycolate).[48] ZnO crystals were formed by hydrolysis and condensation of zinc nitrate (5.0 mM) in water with hexamethylene tetramine ($C_6H_{12}N_4$, 5.0 mM), and the sodium salt of the ligands. Each solution was heated to 90 ˚C for 2 hours and then filtered and washed with water and ethanol. XRD was used to confirm the wurtzite ZnO structure.

1.4 Characterization of ZnO

The majority of the characterization of ZnO is done by utilizing three techniques: X-ray diffraction (XRD), scanning electron microscopy (SEM) and transmission electron microscopy (TEM).

1.4.1 X-ray diffraction

XRD is a non-destructive characterization technique that gives detailed information about the chemical composition and crystallographic structure of solid materials. When X-rays interact at certain angles with electrons of atoms arranged in a regular pattern, constructive interference occurs. Parallel X-rays are diffracted by atomic planes at certain incident angles, called the Bragg angles. These can be used to measure average spacing between layers or rows of atoms by the Bragg law (Eq 1.3)

$$2d \sin(\theta) = n\lambda \tag{1.3}$$

where d is the distance between atomic layers, θ is the Bragg angle, and λ is the wavelength of the X-ray. XRD uses the diffraction of X-rays at the Bragg angle to provide information on the crystal structure of unknown materials. Each material has a unique diffraction pattern, which allows for unknown materials to be identified from a known database. For example, ZnO in the wurtzite structure has the characteristic XRD spectrum shown in Figure 2.

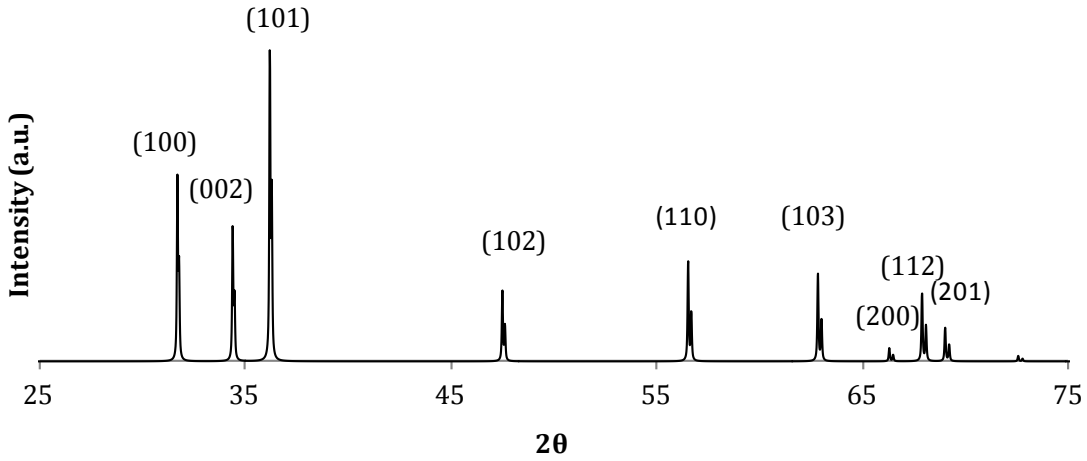

Figure 2 XRD spectrum of the wurtzite crystal structure of ZnO. The labels correspond to (hkl) planes of the ZnO material.

The average size of individual particles can be calculated using the Scherrer equation (Eq 1.5.)

$$D = \frac{k\lambda}{B\cos\theta} \tag{1.4}$$

where D is the particle size in nm, k is a constant of 0.9, λ is the X-ray wavelength in nm, θ is the Bragg's angle in radians, and B is the full width at half maximum of the θ peak used. As nanoparticles decrease in size, line broadening is observed (Figure 3).

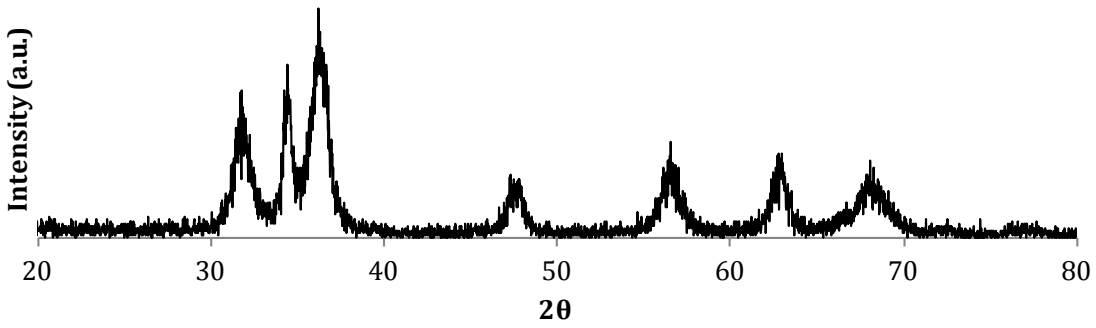

Figure 3. XRD spectrum of ZnO showing peak broadening due to small nanoparticle size of 7.7 nm

1.4.2 Scanning electron microscopy

A scanning electron microscope (SEM) is a type of electron microscope that produces images of a sample by scanning it with a focused beam of electrons. The electrons interact with atoms in the sample, producing various signals that can be detected and that contain information about the sample's surface topography and composition (Figure 4). The most common mode of detection is by secondary electrons emitted by atoms excited by the electron beam. The signals result from interactions of the electron beam with atoms at or near the surface of the sample. In the most common or standard detection mode, secondary electron imaging or SEI, the SEM can produce very high-resolution images of a sample surface, revealing details less than 1 nm in size (Figure 4b and d). Due to the very narrow electron beam, SEM micrographs have a large depth of field yielding a characteristic three-dimensional appearance useful for understanding the surface structure of a sample. The types of signals produced by a SEM include secondary electrons (SE), back-scattered electrons (BSE), characteristic X-rays (Figure 5), light (cathodoluminescence) (CL), specimen current and transmitted electrons.

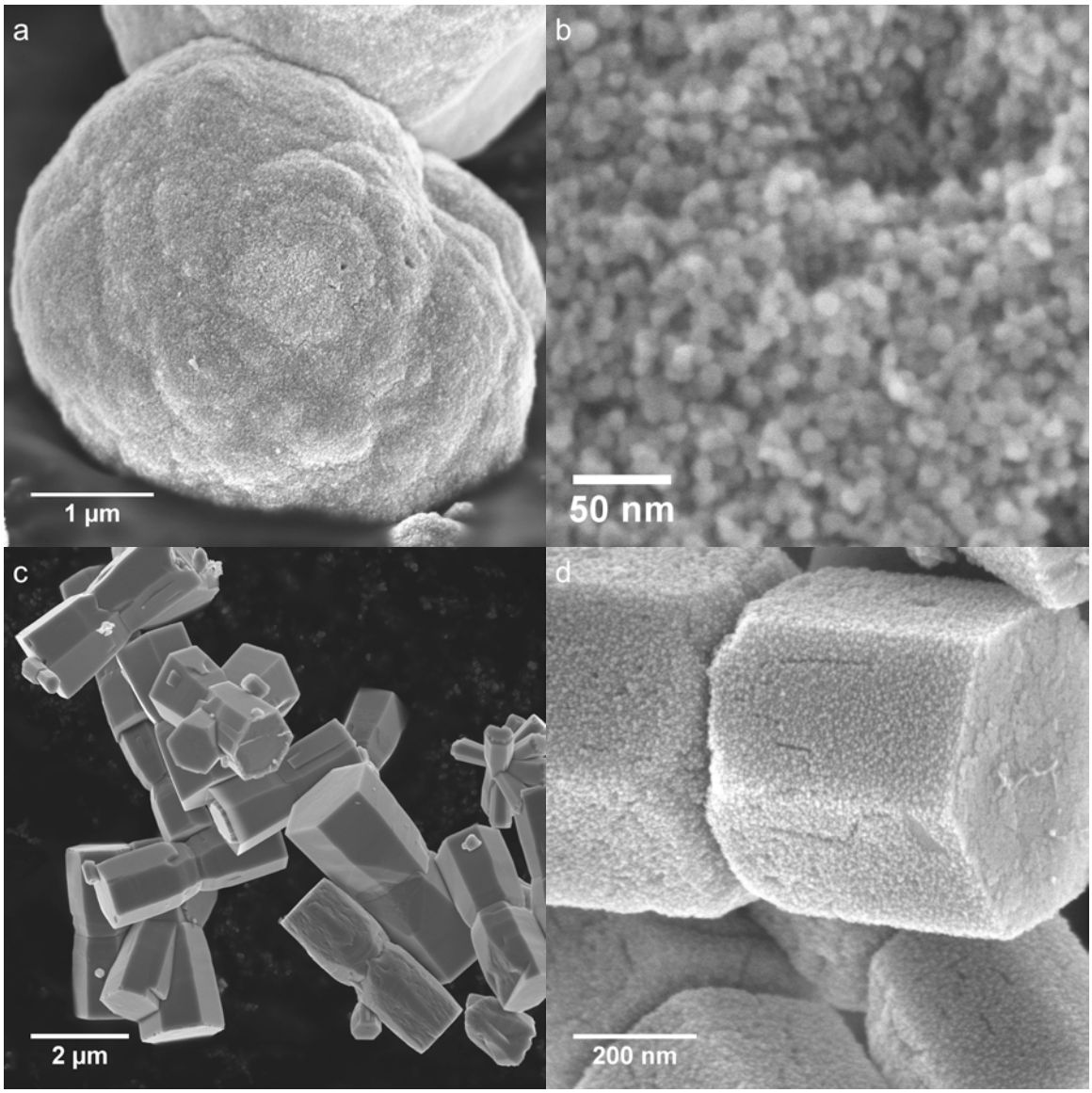

Figure 4. SEM images of different ZnO materials. a) Sphere made from ZnO nanoparticles. b) Nanoparticles on sphere structure. c) ZnO hexagonal prisms. d) ZnO hexagonal prisms showing crystal defects.

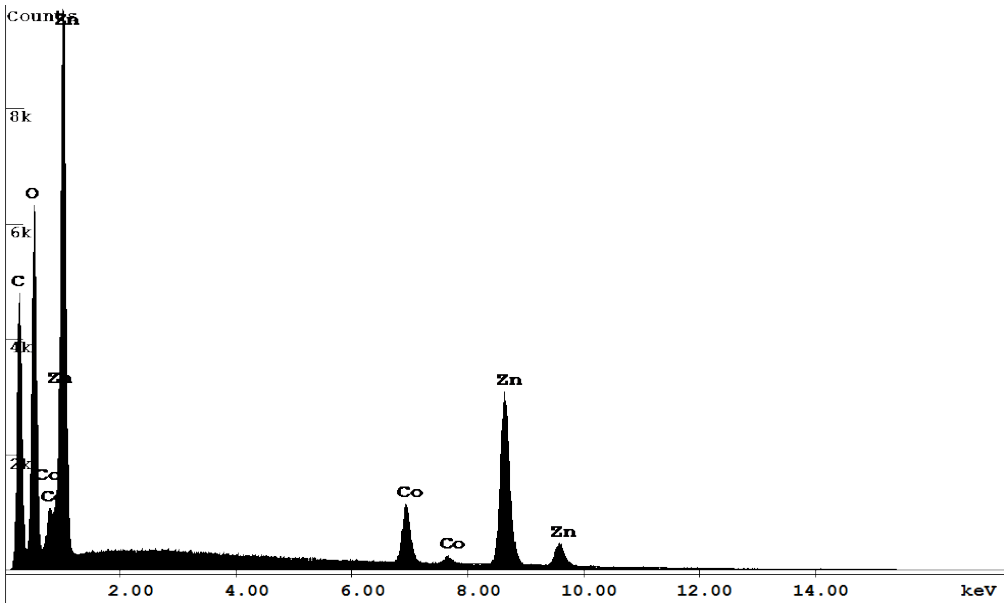

Figure 5. EDS graph of cobalt doped ZnO nanoparticles confirming the presence and percentage of cobalt ions.

1.4.3 Transmission electron microscopy

Transmission electron microscopy (TEM) is a microscopy technique whereby a beam of electrons is transmitted through an ultra-thin specimen, interacting with the specimen as it passes through. An image is formed from the interaction of the electrons transmitted through the specimen; the image is magnified and focused onto an imaging device, such as a fluorescent screen, a layer of photographic film, or a sensor such as a CCD camera. TEM has some limitations, which include the cost of the instrument, its inability to sample a large amount of surface material (only 0.3 mm^3 in the past 15 years[49]), the need to use thin (<100 nm thick) materials, the beam damage caused to the specimen, and no depth sensitivity (2D image of a 3D object) of the material. But the amount of information gained outweighs the limitations (Figure 6).

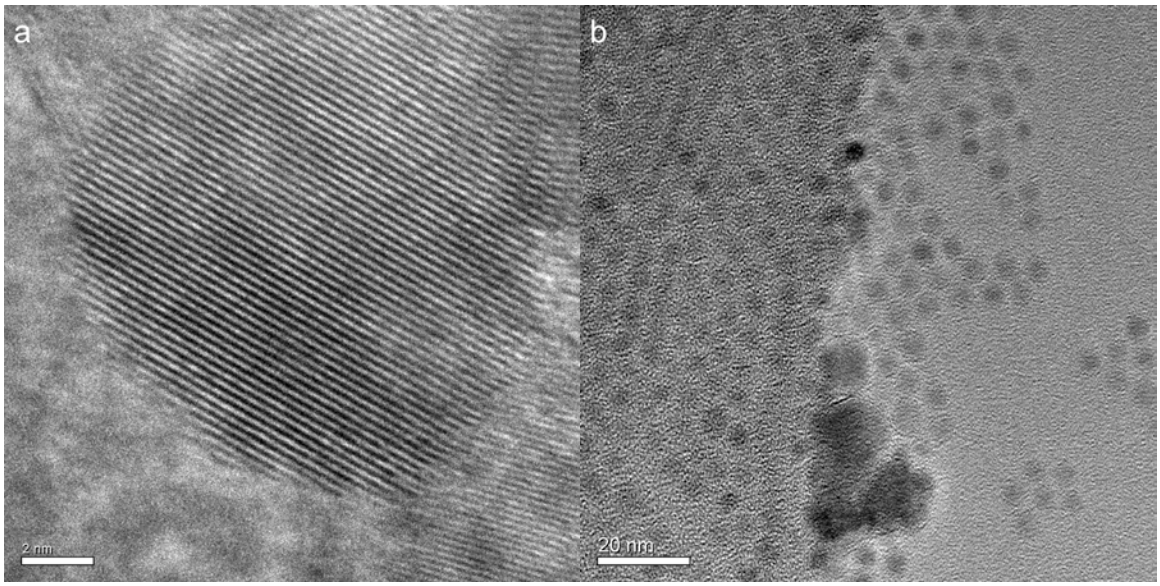

Figure 6. High resolution TEM images of a) a ZnO nanoparticle showing lattice fringes and b) magnetite nanoparticles arranged in a monolayer with hexagonal close packing order.

Most images are collected using a parallel beam, but many techniques are done by using a convergent beam with a Å-sized probe. Analytical techniques such as X-ray energy-dispersive spectrometry (XEDS) and electron energy-loss spectrometry (EELS) allow chemical analysis of the sample (Figure 7). In EELS, material is exposed to a beam of electrons with a known, narrow range of kinetic energies. Some of the electrons undergo inelastic scattering, they lose energy and have their paths slightly and randomly deflected. The amount of energy loss can be measured via an electron spectrometer and interpreted in terms of what caused the energy loss. Inelastic interactions include phonon excitations, inter- and intraband transitions, plasmon excitations, inner shell ionizations, and Bremsstrahlung radiation.

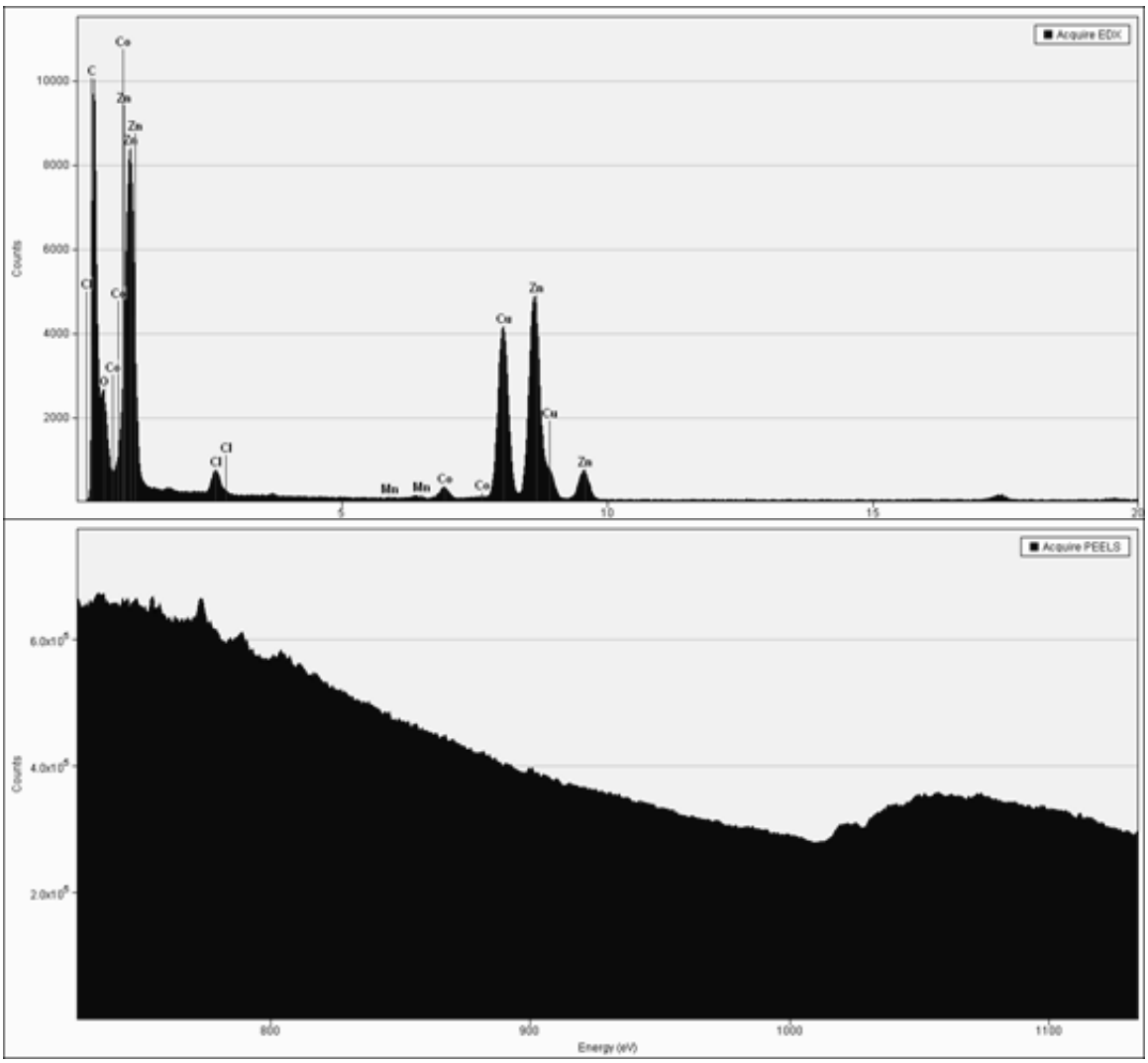

Figure 7. Top image: EDS sprectrum showing Co content in ZnO nanoparticles. Peaks due to C, Cl, Mn and Cu are contamination from the holder and column. Bottom image: EELS spectrum showing some cobalt peak at 780 and 800 eV.

Scanning transmission electron microscopy (STEM), which can show image contrast based on scattering or diffraction (Figure 8). Convergent beam diffraction patterns give direct crystallographic information about small areas of the material.

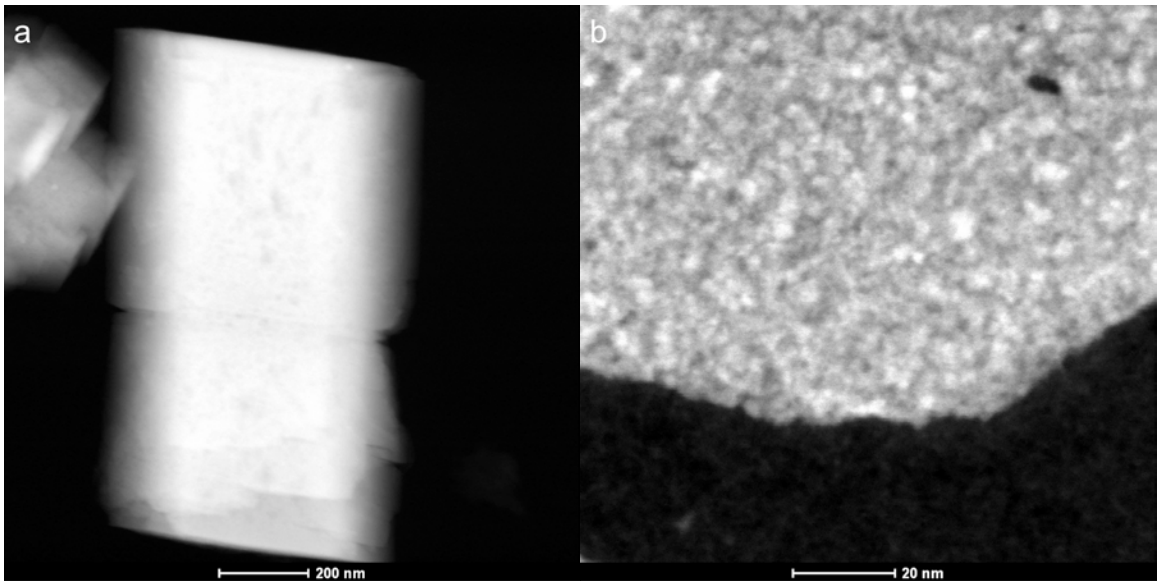

Figure 8. STEM images showing structural abnormalities and mass thickness contrast of a) ZnO hexagonal prism and b) zinc hydroxide nanoparticles

References

1. Wikipedia The Free Encyclopedia. http://en.wikipedia.org/wiki/Zinc_oxide (accessed November 20, 2013).

2. Dechene, G. Semiconductors. *Ann. Phys.* ***1934****, 2*, 241–345.

3. Alivisatos, A. P. Perspectives on the Physical Chemistry of Semiconductor Nanocrystals. *J. Phys. Chem.* **1996,** *100,* 13226–13239

4. Murray, C. B.; Kagan, C. R.; Bawendi, M. G. Synthesis And Characterization Of Monodisperse Nanocrystals And Close-Packed Nanocrystal Assemblies. *Annu. Rev. Mater. Sci.* **2000**, *30*, 545–610.

5. Shriver, D. F.; Atkins, P. W.; Overton, T. L.; Rourke, J. P.; Weller, M. T.; Armstrong, F. A. Nanomaterials, Nanoscience, and Nanotechnology. *Inorganic Chemistry* 4th ed., W. H. Freeman and Company. New York, 2006.

6. Meulenkamp, E. A., Synthesis and Growth of ZnO Nanoparticles. *J. Phys. Chem. B* **1998,** *102*, 5566–5572.

7. Yunbo, L.; Wen, X.; Weiyan, L.; Junmin, X.; Jun, D., Controllable synthesis of ZnO nanoparticles with high intensity visible photoemission and investigation of its mechanism. *Nanotechnology* **2013,** *24*, 175702.

8. Zhang, X. L.; Qiao, R.; Kim, J. C.; Kang, Y. S. Inorganic Cluster Synthesis and Characterization of Transition-Metal-Doped ZnO Hollow Spheres. *Cryst. Growth Des.* ***2008****, 8,* 2609–2613.

9. Yang, R. D.; Tripathy, S.; Li, Y.; Sue, H.-J., Photoluminescence and micro-Raman scattering in ZnO nanoparticles: The influence of acetate adsorption. *Chem. Phys. Lett.* **2005,** *411*, 150-154.

10. Sun, D.; Wong, M.; Sun, L.; Li, Y.; Miyatake, N.; Sue, H.-J., Purification and stabilization of colloidal ZnO nanoparticles in methanol. *J. Sol-Gel Sci. Technol.* **2007,** *43*, 237-243.

11. Santra, P. K.; Mukherjee, S.; Sarma, D. D., Growth Kinetics of ZnO Nanocrystals in the Presence of a Base: Effect of the Size of the Alkali Cation. *J. Phys. Chem. C* **2010,** *114*, 22113-22118.

12. Suchanek, W. L., Systematic study of hydrothermal crystallization of zinc oxide (ZnO) nano-sized powders with superior UV attenuation. *J. Cryst. Growth* **2009,** *312*, 100-108.

13. Monticone, S.; Tufeu,R.; Kanaev, A. V. Complex Nature of the UV and Visible Fluorescence of Colloidal ZnO Nanoparticles *J. Phys. Chem. B* **1998**, *102*, 2854–2862.

14. Wong, E. A.; Bonevich, J. E.; Searson, P. C. Growth Kinetics of Nanocrystalline ZnO Particles from Colloidal Suspensions *J. Phys. Chem. B* **1998**, *102*, 7770–7775.

15. Fu, Y.-S.; Du, X.-W.; Kulinich, S. A.; Qiu, J.-S.; Qin, W.-J.; Li, R.; Sun, J.; Liu, J., Stable Aqueous Dispersion of ZnO Quantum Dots with Strong Blue Emission via Simple Solution Route. *J. Amer. Chem. Soc.* **2007,** *129*, 16029-16033.

16. Sugunan, A.; Warad, H. C.; Boman, M.; Dutta, J., Zinc oxide nanowires in chemical bath on seeded substrates: Role of hexamine. *J. Sol-Gel Sci. Technol.* **2006,** *39*, 49-56.

17. Jang, W. S.; Lee, T. I.; Oh, J. Y.; Hwang, S. H.; Shon, S. W.; Kim, D. H.; Xia, Y.; Myoung, J. M.; Baik, H. K., Kinetically controlled way to create highly uniform mono-dispersed ZnO sub-microrods for electronics. *J. Mater. Chem.* **2012,** *22*, 20719–20727.

18. Greene, L. E.; Yuhas, B. D.; Law, M.; Zitoun, D.; Yang, P. Solution-Grown Zinc Oxide Nanowires. *Inorg. Chem.* **2006**, *45*, 7535–7543.

19. Özgür, Ü.; Alivov, Ya. I.; Liu, C.; Teke, A.; Reshchikov, M. A.; Doğan, S.; Avrutin, V.; Cho, S.-J.; Morkoç, H. A comprehensive review of ZnO materials and devices. *J. Appl. Phys.*, **2005**, *98,* 041301.

20. Xiong, H. M.; Shchukin, D. G.; Möhwald, H.; Xu, Y.; Xia, Y. Y. Sonochemical Synthesis of Highly Luminescent Zinc Oxide Nanoparticles Doped with Magnesium(II). *Angew. Chem. Int. Ed.* **2009**, *48*, 1–6.

21. Viswanatha, R.; Sapra, S.; Gupta, S. A.; Satpati, B.; Satyam, P. V.; Dev, B. N.; Sarma, D. D. Synthesis and Characterization of Mn-Doped ZnO Nanocrystals. *J. Phys. Chem. B* **2004**, *108*, 6303–6310.

22. Kato, H.; Sano, M.; Miyamoto, K.; Yao, T. Growth and characterization of Ga-doped ZnO layers on a-plane sapphire grown by molecular beam epitaxy. *J. Cryst. Growth* **2002**, *237,* 538–543.

23. Polarz, S.; Orlov, A.; Hoffmann, A.; Wagner, M. R.; Rauch, C.; Kirste, R.; Gehlhoff, W.; Aksu, Y.; Driess, M.; van den Berg, M. W. E.; Lehmann, M. A Systematic Study on Zinc Oxide Materials Containing Group I Metals (Li, Na, K)—Synthesis from Organometallic Precursors, Characterization, and Properties. *Chem. Mater.* **2009**, *21*, 3889–3897.

24. Chavillon, B.; Cario, L.; Renaud, A.; Tessier, F.; Cheviré, F.; Boujtita, M.; Pellegrin, Y.; Blart, E.; Smeigh, A.; Hammarström, L.; Odobel, F.; Jobic, S. P-Type Nitrogen-Doped ZnO Nanoparticles Stable under Ambient Conditions. *J. Am. Chem. Soc.* **2012**, *134*, 464–470.

25. Radovanovic, P. V.; Norberg, N. S.; Mcnally, K. E.; Gamelin, D. R. Colloidal Transition-Metal-Doped ZnO Quantum Dots. *J. Am. Chem. Soc.* **2002**, *122*, 15192–15193.

26. Radovanovic, P. V.; Gamelin, D. R. Electronic Absorption Spectroscopy of Cobalt Ions in Diluted Magnetic Semiconductor Quantum Dots: Demonstration of an

Isocrystalline Core/Shell Synthetic Method. *J. Am. Chem. Soc*. **2001**, *123*, 12207–12214.

27. Mikulec, F. V.; Kuno, M.; Bennati, M.; Hall, D. A.; Griffin, R. G.; Bawendi, M. G. Organometallic Synthesis and Spectroscopic Characterization of Manganese-Doped CdSe Nanocrystals. *J. Am. Chem. Soc*. **2000**, *122*, 2532–2540.

28. Garcia, M. A.; Merino, J. M.; Fernández Pinel, E.; Quesada, A.; de la Venta, J.; Ruíz González, M. L.; Castro, G. R.; Crespo, P.; Llopis, J.; González-Calbet, J. M., Hernando, A. Magnetic Properties of ZnO Nanoparticles. *Nano Lett.* **2007**, *7*, 1489–1494.

29. Kittilstved, K. R.; Gamelin, D. R. Activation of High-T_C Ferromagnetism in Mn^{2+}-Doped ZnO using Amines *J. Am. Chem. Soc*. **2005**, *127*, 5292–5293.

30. Schwartz, D. A.; Norberg, N. S.; Nguyen, Q. P.; Parker, J. M.; Gamelin, D. R. Magnetic Quantum Dots: Synthesis, Spectroscopy, and Magnetism of Co- and Ni-Doped ZnO Nanocrystals *J. Am. Chem. Soc*. **2003**, *125*, 13205–13218.

31. Wang, Z. L. Zinc oxide nanostructures: growth, properties and applications. *J. Phys.: Condens. Matter*, **2004**, *16*, R829–R858.

32. Liu, B.; Zeng, H. C., Hydrothermal Synthesis of ZnO Nanorods in the Diameter Regime of 50 nm. *J. Am. Chem. Soc* **2003,** *125*, 4430–4431.

33. Vayssieres, L., Growth of Arrayed Nanorods and Nanowires of ZnO from Aqueous Solutions. *Adv. Mater*. **2003,** *15*, 464–466.

34. Lam, S.-M.; Sin, J.-C.; Zuhairi Abdullah, A.; Rahman Mohamed, A., Green hydrothermal synthesis of ZnO nanotubes for photocatalytic degradation of methylparaben. *Mater. Lett.* **2013,** *93*, 423–426.

35. Pan, Z. W.; Dai, Z. R.; Wang, Z. L., Nanobelts of semiconducting oxides. *Science* **2001,** *291*, 1947–1949.

36. Wu, X.; Qu, F.; Zhang, X.; Cai, W.; Shen, G., Fabrication of ZnO ring-like nanostructures at a moderate temperature via a thermal evaporation process. *J. Alloys Compd*. **2009,** *486*, L13–L16.

37. Gao, P.; Wang, Z. L., Self-Assembled Nanowire−Nanoribbon Junction Arrays of ZnO. *J. Phys. Chem. B* **2002,** *106*, 12653–12658.

38. Zhu, C.; Lu, B.; Su, Q.; Xie, E.; Lan, W., A simple method for the preparation of hollow ZnO nanospheres for use as a high performance photocatalyst. *Nanoscale* **2012,** *4*, 3060–3064.

39. Qiu, Y.; Yang, S., ZnO nanotetrapods: controlled vapor-phase synthesis and application for humidity sensing. *Adv. Funct. Mater.* **2007,** *17*, 1345–1352.

40. Pan, A.; Yu, R.; Xie, S.; Zhang, Z.; Jin, C.; Zou, B., ZnO flowers made up of thin nanosheets and their optical properties. *J. Cryst. Growth* **2005,** *282*, 165–172.

41. Zang, C. H.; Liu, Y. C.; Zhao, D. X.; Zhang, J. Y.; Shen, D. Z., The synthesis and optical properties of ZnO nanocombs. *J. Nanosci. Nanotechnol.* **2010,** *10*, 2370–2374.

42. Huang, M. H.; Mao, S.; Feick, H.; Yan, H; Wu, Y.; Kind, H.; Weber, E.; Russo, R.; Yang, P. Room-temperature ultraviolet nanowire nanolasers *Science* **2001**, *292,* 1897–1899.

43. Li, Y. B.; Bando, Y.; and Golberg, D. ZnO nanoneedles with tip surface perturbations: Excellent field emitters. *Appl. Phys. Lett.* **2004**, *84,* 3603–3605.

44. Zhang, X. L.; Qiao, R.; Qiu, R.; Kim, J. C.; Kang, Y. S., Fabrication of Hierarchical ZnO Nanostructures via a Surfactant-Directed Process. *Cryst. Growth Des.* **2009,** *9*, 2906–2910.

45. Bitenc, M.; Dražić, G.; Orel, Z. C., Characterization of Crystalline Zinc Oxide in the Form of Hexagonal Bipods. *Cryst. Growth Des.* **2010,** *10*, 830–837.

46. Hou, H.; Xie, Y.; Li, Q., Structure-directing self-organized, one-dimensional ZnO single-crystal whiskers. *Solid State Sciences* **2005,** *7*, 45–51.

47. Sun, S.; Zhang, X.; Zhang, J.; Song, X.; Yang, Z., Unusual Designated-Tailoring on Zone-Axis Preferential Growth of Surfactant-Free ZnO Mesocrystals. *Cryst. Growth Des.* **2012,** *12*, 2411–2418.

48. Meagley, K. L.; Garcia, S. P., Chemical Control of Crystal Growth with Multidentate Carboxylate Ligands: Effect of Ligand Denticity on Zinc Oxide Crystal Shape. *Cryst. Growth Des.* **2012,** *12*, 707–713.

49. Williams, D. B.; Carter, C. B. *Transmission Electron Microscope, A Textbook for Materials Science*, Springer Science+Business Media, 2009.

Chapter 2: Assembly and Magnetic Properties of ZnO Nanoparticles Doped with Cobalt, Nickel and Manganese

ABSTRACT[1]

Zinc oxide semiconductors are synthesized with small amounts of magnetic ions to create materials called dilute magnetic semiconductors (DMS). Dilute magnetic semiconductors can be made through a variety of synthesis techniques. We have employed a low temperature sol-gel method that produces ZnO nanoparticles of reproducible size and incorporates cobalt, nickel, and manganese ions into the nanoparticles. Conditions were controlled such that a range of amounts of Co, Ni and Mn were incorporated. The incorporation could be tracked by color changes in the white ZnO powder to blue for Co, green for Ni and yellow for Mn. XRD measurements showed the nanoparticles are on the order of 10 nm in diameter and have a wurtzite structure. The nanoparticles aligned along lattice fringes and assembled into spherical structures. Nanoparticle alignment was disrupted when high concentrations of metal dopants were incorporate into the nanoparticles. Magnetic measurements showed a change from diamagnetic to paramagnetic behavior with increasing concentration of metal dopants.

[1] Work submitted for publication
Hancock, J. H.; Rankin, W. M.; Hammad, T. M.: Salem, J. S.; Chesnel, K.; Harrison, R. G. *J. Nanosci. Nanotechnol.* **2013**.

2.1 Introduction

Zinc oxide materials are widely studied due to their electronic, optical and structural properties. Zinc oxide is a wide band gap (3.37 eV) semiconductor, which absorbs ultraviolet light and forms the wurtzite structure.[1] The ability to change the properties of ZnO materials is currently of important interest, and one approach is to incorporate transition metal ions into the material. The incorporation of transition metal ions may not only change the band gap and light absorption properties, but also the magnetism. The combination of semiconducting and magnetization properties into one material could lead to faster and cheaper electronic components. Semiconductor materials with small amounts of magnetic ions encompass a new class of materials called dilute magnetic semiconductors (DMS).[2,3]

Metal oxide nanoparticle synthesis, in particular ZnO nanoparticle synthesis, is accomplished in a variety of ways. Several methods that give pure product require heating a mixture of metal ions in an annealing process.[4-6] Other methods involve the addition of base to alcoholic solutions of metal ions.[7-10] These and other methods may also involve the addition of ligands during the synthesis to limit nanoparticle growth or to change nanoparticle solubility.[11-13]

Transition metal-doped ZnO nanoparticles are important due to the transition metal's ability to change the magnetic and conducting properties of the ZnO.[7,14] Transition metal ions of interest are principally Co^{2+} and Mn^{2+}, but also other metal ions such as Ni^{2+}, Cu^{2+}, Fe^{2+}, Al^{3+}, Mg^{2+}, and Cd^{2+} have been studied.[15-17] The size, optical, and magnetic properties of the particular metal ion gives unique properties to the doped material. The materials can even be ferromagnetic due to oxygen vacancies and to the

volume/area ratio in the nanoparticle oxides.[18,19] For example, ZnO nanoparticles synthesized through an alcoholysis ester elimination reaction have been doped with small amounts of Co^{2+} and Ni^{2+} ($Zn_{1-x}TM_xO$ where x = 0-0.07 for Co and x = 0.02- 0.03 for Ni) and shown to have room temperature ferromagnetism.[20] Also, manganese and nickel have been doped into ZnO nanoparticles which self-aggregate.[21] It has also been shown that the ferromagnetism of both Mn doped ZnO nanoparticles and bulk ZnO is affected by surface ligands.[22] Manganese has also been successfully added to many types of structures besides nanoparticles, including nanorods made at low-temperature in an ethanolic solution with KOH, which had manganese doping of 1.3–5% .[23] Cobalt has also been added to different ZnO structures, such as nanowires, with doping percentages from 1–11% .[24]

In this paper we present a low temperature synthetic method to prepare transition metal-doped ZnO nanoparticles with reproducible size and amounts of Co, Mn, and Ni. We observe that the doped nanoparticles have different electronic, optical, and magnetic properties. The amount of cobalt, manganese, and nickel incorporated is measured by inductively coupled plasma (ICP), but can also be monitored by the color change from the white ZnO powder to blue (Co), yellow (Mn), and green (Ni) powders. We have also observed that the nanoparticles self-assemble into micron sized hollow structures and align along lattice fringes. These microstructures deform and diminish in size with added amounts of transition metal ions. Also, the lattice fringe alignment between the nanoparticles is disrupted at higher concentrations of metal dopant. Along with these structural changes, the ZnO band gap is not significantly shifted with added dopant. We

have also observed that the paramagnetism of these materials increases as dopant amounts increase.

2.2 Experimental

2.2.1 Materials

Zinc acetate dihydrate, cobalt(II) acetate tetrahydrate, manganese(II) acetate tetrahydrate, nickel(II) acetate tetrahydrate, methanol (HPLC grade), and ethanol (200 proof) were obtained from commercial suppliers and used as received. TEM grids were purchased from Ted Pella Inc.

2.2.2 Synthesis of ZnO nanoparticles

Zinc oxide nanoparticles were synthesized in methanolic solutions with gentle heating.[11] In a typical reaction, a round bottom flask was charged with $Zn(C_2H_3O_2)_2 \cdot 2H_2O$ (2.195 g, 10.00 mmol), 1 equivalent of distilled water (0.20 mL, 11 mmol) and methanol (50 mL). The solution was homogenized by sonication for 10 minutes, after which it was heated at 65.0 °C for 24 hr. Some precipitate formed during this period and continued to form as the flask sat at room temperature for 24 hr after heating. The precipitate was isolated by decantation after the solution was sonicated for 6 min and centrifuged at 5000 rpm's for 6 min. The solid was then washed three times with ethanol (25 mL), sonicated, centrifuged, and decanted. The solid was dried overnight at 120 °C and yielded 0.3170 g (38.95% yield). Nanoparticles were stored in water free containers to prevent potential growth from water vapor in the air.[25]

2.2.3 Synthesis of transition metal doped nanoparticles

The zinc acetate methanolic solution was prepared as stated for pure ZnO, except that either 1, 2, 3, 5, 7, or 10 mol % of $Co(C_2H_3O_2)_2 \cdot 4H_2O$, $Mn(C_2H_3O_2)_2 \cdot 4H_2O$, or $Ni(C_2H_3O_2)_2 \cdot 4H_2O$ was added to it before initial sonication. Solutions of different colors were observed when the ions were added: pink with Co^{2+} ions, brown with Mn^{2+} ions, and green with Ni^{2+} ions. The heating, washing, and drying procedures were then followed as for pure ZnO. Yields for the doped materials were: Co 0.2383 g (29.27% yield), Mn 0.2285 g (28.06% yield), and Ni 0.2262 g (27.79% yield).

2.2.4 Characterization techniques

X-ray diffraction (XRD) was performed on the PANalytical X'Pert Pro diffractometer with a Cu source and a Ge monochromator tuned to the Cu-Kα1 wavelength (λ = 1.540598 Å). Each nanomaterial was scanned from 5–80° 2θ with a step size of 0.0423°/s. Each pattern was matched to a standard pattern in the ICDD (International Center for Diffraction Data) database. Crystallite sizes were estimated using the Scherrer formula for size-related peak broadening.[26] Transmission electron microscope (TEM) images were taken with a FEI Tecnai F20 Ultra-Twin TEM/STEM operating at 200kV, equipped with a Si(Li) X-ray energy dispersive spectrometry (XEDS) detector, model EDAX PV 9761/55 ME with 30 mm^2 active area and a super-ultra thin window (SUTW). Scanning electron microscope (SEM) images were taken on a FEI Helios Nanolab 600. UV-vis absorption spectra were obtained with a Hewlett Packard 8453 spectrometer with dispersion of nanoparticles in ethanol. Metal ion concentrations were measured on a Perkin Elmer Optima 2000DV inductively coupled plasma (ICP) optical emission spectrometer. Magnetic moments were measured on a Quantum Design Physical

Property Measurement System (PPMS) Vibrating Sample Magnetometer (VSM) with a zero field and 1000kOe applied field. X-ray photoelectron spectroscopy (XPS) analyses were performed using a Surface Science SSX-100 X-ray photoelectron spectrometer (serviced by Service Physics, Bend, OR) with a monochromatic Al K_α source, a hemispherical analyzer, and a take-off angle of 35°. Survey scans were recorded with an 800 μm × 800 μm spot size with a resolution of 4. Narrow scans were recorded with a spot size of 300 μm × 300 μm with a resolution of 2. The XP spectra were analyzed using the ESCA Data Analysis Application software (Version: Analysis 25 V.01.02). IR spectra were obtained from a Thermo-Nicolet Avatar 370 FT-IR spectrometer.

2.3 Results and discussion

2.3.1 Preparation of nanoparticles

The ZnO materials were synthesized by heating methanolic solutions of zinc acetate and water. ZnO solid begins to form after about eight hours of heating and continues to form after the solution cools and sits at room temperature. The temperature of 65 °C is critical to the formation of the materials; if the solution temperature is slightly cooler than 65 °C, solids did not form. The water supplies the oxide oxygens and the acetate acts as base. Thus as seen in equation 2.1, no other base, such as hydroxide, is needed.

$$Zn(C_2H_3O_2)_2 + H_2O \rightarrow ZnO(s) + 2HC_2H_3O_2 \qquad (2.1)$$

Without the addition of an equivalent of water, a large amount of zinc hydroxide and other impurities are produced, which require more washing to remove.[27]

When the acetate salts of Co^{2+}, Mn^{2+}, and Ni^{2+} were added to the zinc acetate solution during synthesis, ZnO precipitates again formed, but the materials were no longer white. The amount of ZnO material and the rate it formed were not affected by

the 1 – 10% concentrations of the transition metal ions. However, at the higher concentration of transition metals (10 mol %), acetate became increasingly difficult to remove from the materials and additional washes were required. Even with water present in the synthesis and ethanol washes, a small amount of acetate remained as detected by IR measurements. The acetates did not form crystalline structures, as shown by the XRD spectra, which only showed ZnO. The presence of the transition metals did affect the color of the precipitates. Rather than the pure white powder of ZnO, a blue solid was obtained from the pink Co^{2+} solution, a pale yellow solid was isolated from the brown Mn^{2+} solution, and a light green solid was separated from the green Ni^{2+} solution (Figure 1).

Figure 1. Colors of ZnO materials: white – pure, green – doped with Ni, yellow – doped with Mn, and blue – doped with Co.

The colors were visibly more intense with higher concentrations of transition metal ions. Colored solids indicate that the transition metals are being incorporated into the ZnO lattice. If the transition metal ions were going into wurtzite ZnO lattice, they would be in tetrahedral environments, unlike the octahedral solution environment. Co^{2+} in a tetrahedral environment is blue, Mn^{2+} in a similar environment is yellow, and Ni^{2+} is green or blue in such an environment.[28] Thus, the incorporated metal ions look to be in the 2^+ oxidation state.

2.3.2 Characterization of nanoparticles

The wurtzite crystal structure was observed for the doped and undoped ZnO nanoparticle materials (Figure 2). ZnO normally forms the wurtzite structure and the presence of Co^{2+}, Mn^{2+}, and Ni^{2+} did not affect that, even though CoO, MnO, and NiO crystalize in the rock salt structure. As shown by XRD spectra, there were no impurities in the materials, such as zinc hydroxide or zinc acetate. Also, there were not any peaks for crystalline oxides of Co, Mn, or Ni noted in the XRD spectra. The lack of other structures indicates the transition metals are likely being incorporated into the ZnO lattice, predictably replacing some of the zinc ions due to their similar charge and size.[29]

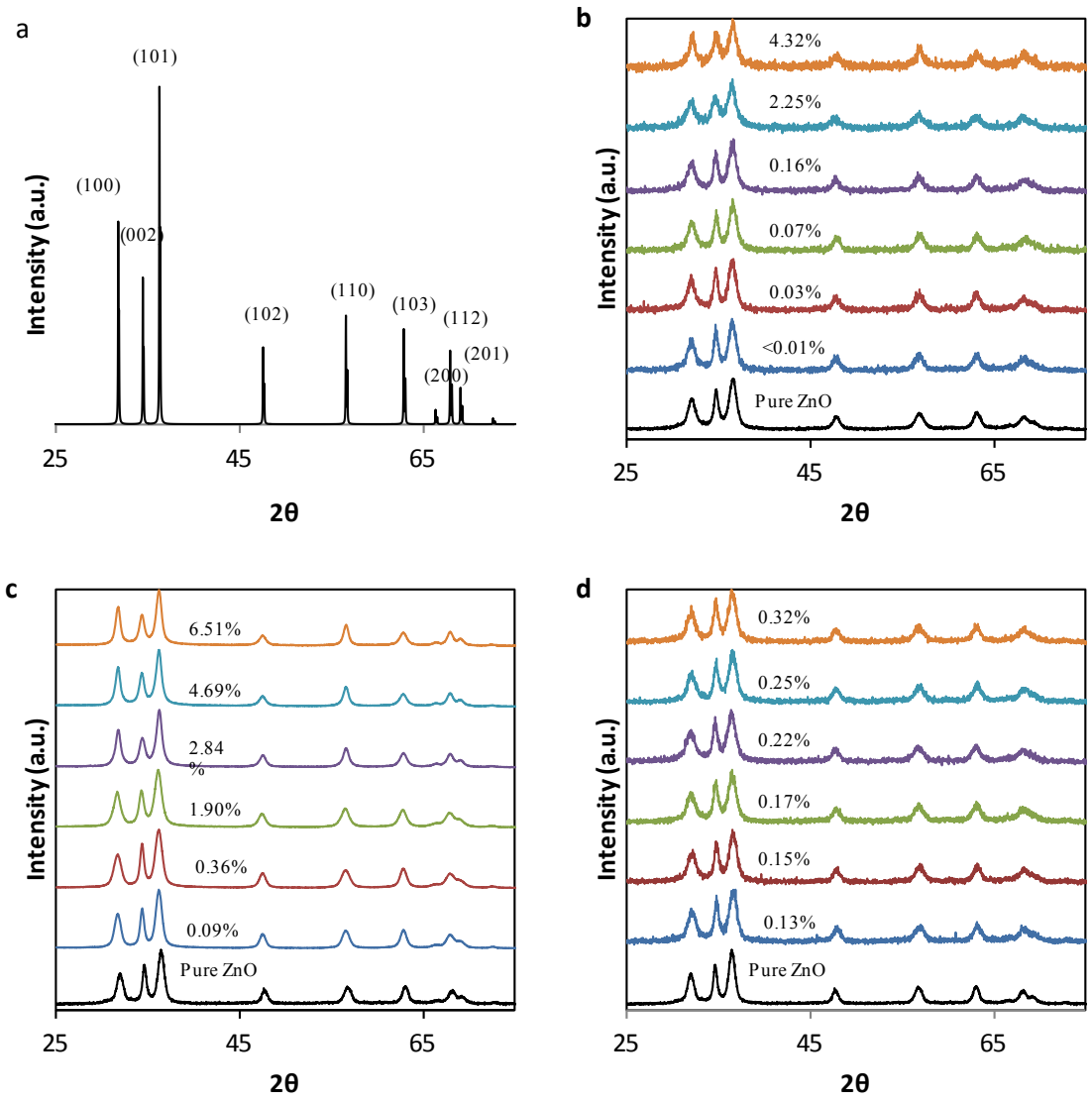

Figure 2. XRD spectra of reference ZnO (a) and materials doped with Co (b), Ni (c), and Mn (d). The mole percentages of dopants found in the materials are indicated on the spectra.

XRD spectra also allowed for the calculation of nanopartcle size. The Scherrer formula

$$D = \frac{k\lambda}{B\cos\theta} \tag{2.2}$$

where D is the particle size in nm, k is a constant of 0.9, λ is the X-ray wavelength in nm, θ is the Bragg's angle in radians, and B is the full width at half maximum of the peak in radians was used. The seven most prominent peaks (100), (002), (101), (102), (110), (103), and (112) were used in the calculation (Figure 2). Using this equation, we found nanoparticles ranged in size from 8-12 nm whether they had incorporated transition metals ions or not.

ZnO nanoparticles with different amounts of transition metal ions were formed. We found that about half of the Co^{2+} and Ni^{2+} ions present were incorporated into the nanoparticles (Table 1). Materials with Co in them had from 0.1 to 4.3 mol % and those with Ni had from 0.1 to 6.5 mol %. Manganese ions proved to incorporate at a lower amount and even when 10 mol % was present; only 0.3 mol % was incorporated. To help identify the charge and location of the transition metal ions, XPS was performed. The XPS spectra showed small signals for Co^{2+} and Ni^{2+}, too small to accurately integrate, but large enough to indicate the presence of each of these metal ions. This indicates the metal ions are spread throughout the nanoparticles and not congregated on the surface.

Table 1. Mole percentages of Co, Ni and Mn in ZnO materials determined by ICP. The first column indicates the mole percent of transition metal (TM) in the starting solution and columns 2 – 4 indicated the percentage found in the isolated solids.

Mole % of TM Ion in Solution	Mole % of TM Ion in Material		
	Co^{2+}	Ni^{2+}	Mn^{2+}
1	0.0–0.10	0.02–0.09	0.01–0.13
2	0.03–0.14	0.05–0.36	0.07–0.15
3	0.07–0.21	0.09–1.9	0.06–0.17
5	0.16–0.32	2.8–3.9	0.12–0.22
7	0.37–2.25	3.9–4.7	0.14–0.25
10	1.3–4.32	5.3–6.5	0.22–0.32

2.3.3 Electron microscopy characterization

The nanoparticles self-assemble into micron sized spherical structures with hollow interiors as shown by SEM (Figure 3). Others researchers have also been able to synthesize ZnO materials composed of hollow spheres but by the layering nanoplates.[30] Also, a single-step electrochemical method has been used to create template-free hollow ZnO nanospheres.[31] When SEM images of our ZnO materials were taken, surface nanoparticles were observed as building blocks for the microstructures (Figure 3b). We noted that the nanoparticles that had the larger amounts of Co and Ni ions self-assembled into smaller structures (Figure 3f, 3g). The Mn-doped materials self-assembled like the pure ZnO materials, presumably due to their low levels of incorporated Mn.

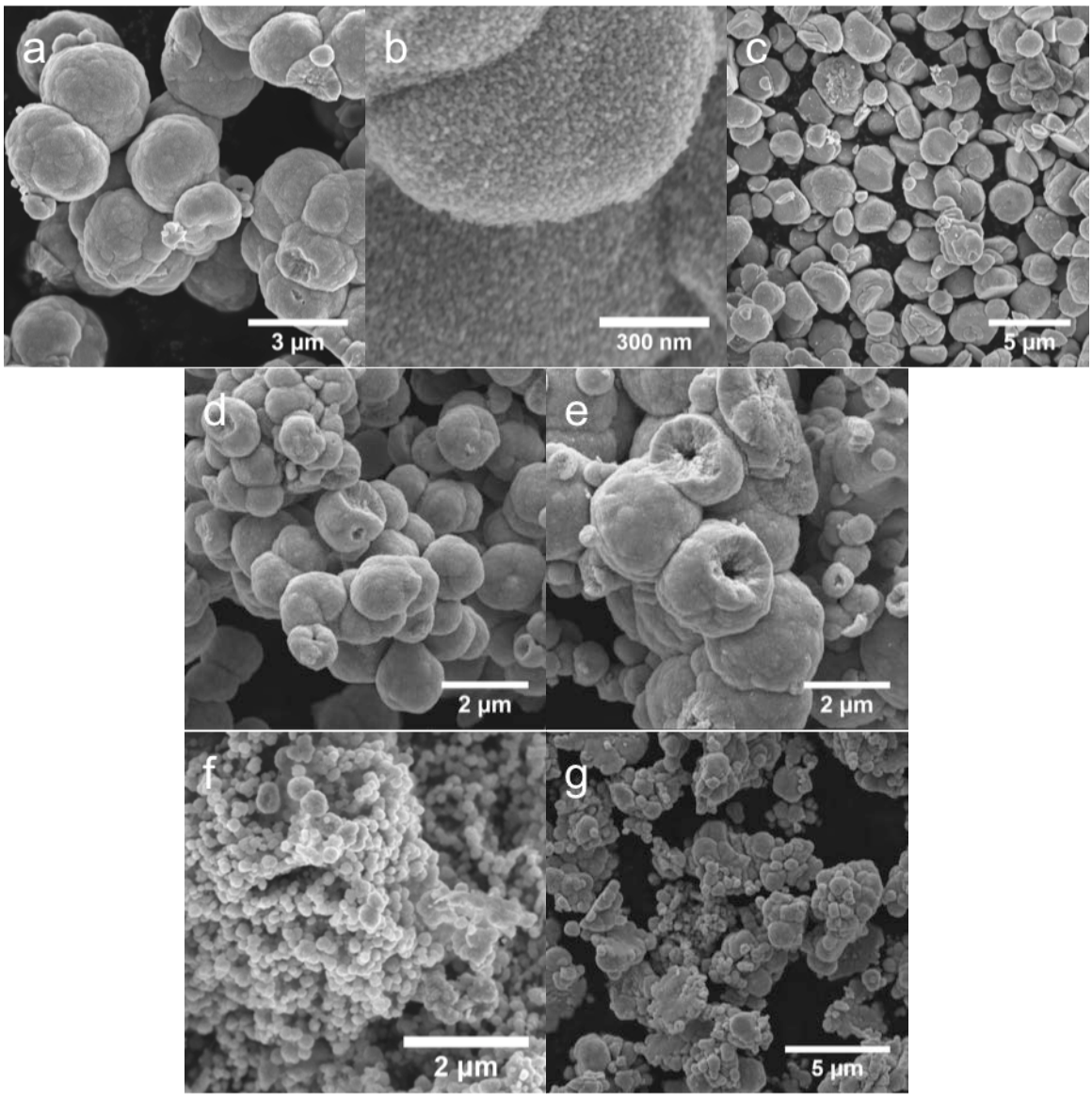

Figure 3. SEM images of self-assembled ZnO nanoparticles. (a) Pure ZnO. (b) Surface of ZnO assembly showing nanoparticles. (c) Low percent of Ni (0.36%). (d) Low percent of Co (0.14%). (e) Low percent of Mn (0.13 %). (f) High percent of Ni (2.84%). (g) High percent of Co (2.25%).

The wurtzite structure of the ZnO nanoparticles as seen by XRD was confirmed by TEM diffraction patterns (Figure 4a). The ratio of the first and second rings is 1.13, consistent with ZnO having a hexagonal close packed crystal lattice. The TEM diffraction patterns containing bright dots show that the materials are crystalline and that dopants do not cause the formation of amorphous materials. As seen in Fig. 4c and 4d,

the nanoparticles align in two directions from the center of the microstructure, tangentially and radially. Alignment of the atomic spacing in the ZnO nanoparticles is observed over several nanoparticles. The nanoparticle alignment could be due to nanoparticle formation on a seed nanoparticle or self-assembly of nanoparticles after they have formed. Increasing amounts of incorporated transition metal ions disrupt the alignment, presumably due to transition metal ions that are on the surface, which are slightly different in size and structural preference to Zn^{2+} (Figure 4e and 4f). Further study is needed to better understand the assembly process.

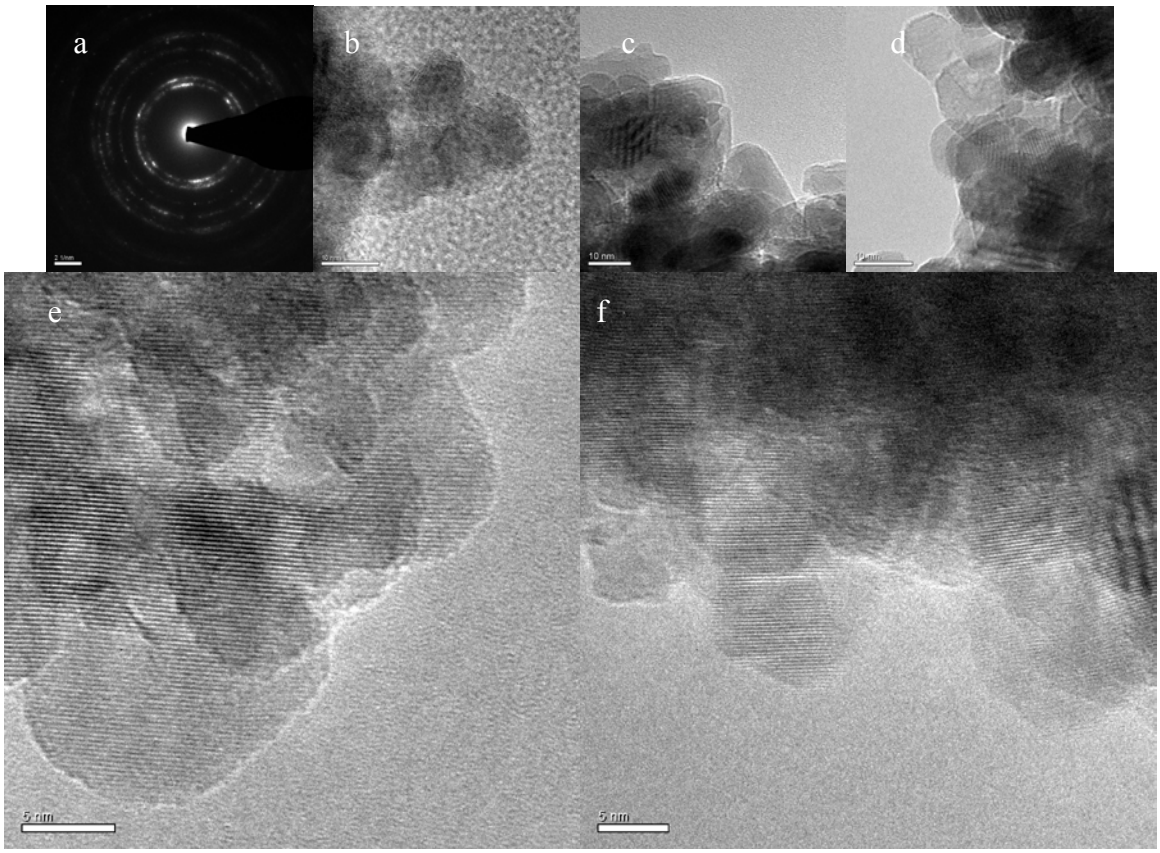

Figure 4. TEM images of ZnO materials showing nanoparticles. (a) Diffraction pattern of ZnO nanoparticles (NPs) showing crystallinity. (b) Co (4.3%) doped NPs. (c) Ni (5.3%) doped NPs. (d) Mn (0.32%) doped NPs (e) ZnO NPs showing radial alignment of NPs. (f) ZnO NPs showing tangential alignment of NPs.

An important aspect of transition metal doping is its affect on the ZnO band gap. Ethanolic solutions of the materials were analyzed by UV-vis absorption spectroscopy to determine the energy of their electronic transition. The nanoparticles do not dissolve well in ethanol, so manual grinding and sonication for several minutes were necessary to disperse the nanoparticles. The ZnO band gap was 365 nm (3.40 eV) (Figure 5). The band gap for the doped materials remains mostly unchanged, it moving slightly to longer wavelengths, 367 nm (3.38 eV), in the Co and Ni doped materials. This implies that the transition metal ions do not disturb the ZnO lattice.

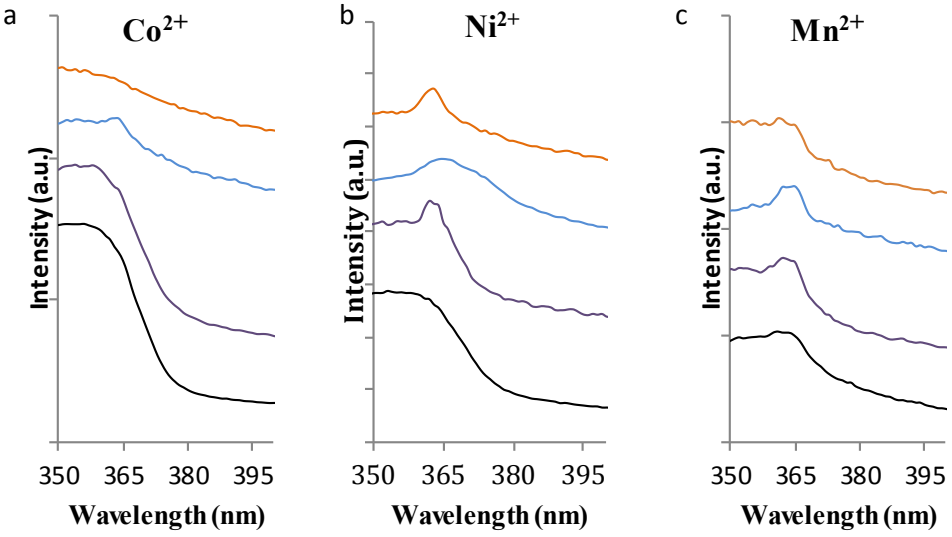

Fig. 5 UV-vis absorption spectra of Co, Mn, and Ni doped ZnO nanoparticles. (a) $Zn_{1-x}Co_xO$ black 0.0012, purple 0.0069, blue 0.023, orange 0.043. (b) $Zn_{1-x}Ni_xO$ black 0, purple 0.0084, blue 0.047, orange 0.065. (c) $Zn_{1-x}Mn_xO$ black 0, purple 0.0001, blue 0.001, orange 0.0023.

2.3.4 Magnetic properties of nanoparticles

The magnetic nature of the transition metal doped materials was investigated to determine if the diamagnetic behavior of ZnO was changed with the addition of transition metal ions. Magnetization measurements were performed on pure ZnO and on Co, Mn, and Ni doped materials by cycling the field between ±10000 Oe at room temperature.

Measurements were also taken on the sample holder. The magnetization curve on pure ZnO nanoparticles (Fig. 6) shows a negative slope, -2×10^{-6} emu/g·Oe, which indicates a diamagnetic behavior with a coercive field H_c of 15 Oe and a magnetization of remanence M_r of 0.0002 emu. When Co is present, the magnetization curves exhibit a paramagnetic signal, with a positive slope (Fig. 6a). Furthermore, the strength of the slope increases with the amount of Co dopant. The comparison between the type of dopants indicates that Co induces the strongest effect, with a susceptibility of $c = 7\times10^{-6}$ emu/g·Oe, compared to $c = 3\times10^{-6}$ emu/g·Oe in the case of Ni, and $c = 2\times10^{-6}$ emu/g·Oe in the case of Mn. This large effect for Co is consistent with the fact that Co atoms are in greater abundance than Mn and Co has more unpaired electrons than Ni in a tetrahedral environment. In the case of Ni doped nanoparticles, magnetization curves also indicate a paramagnetic behavior, whose magnitude increases with amount of Ni dopant (Fig. 6b). When 0.32 % Mn is present, the curve exhibits a slightly more positive slope, which indicates a paramagnetic behavior (Fig. 6c). Increased paramagnetism has been observed in other transition metal doped ZnO materials.[7, 21]

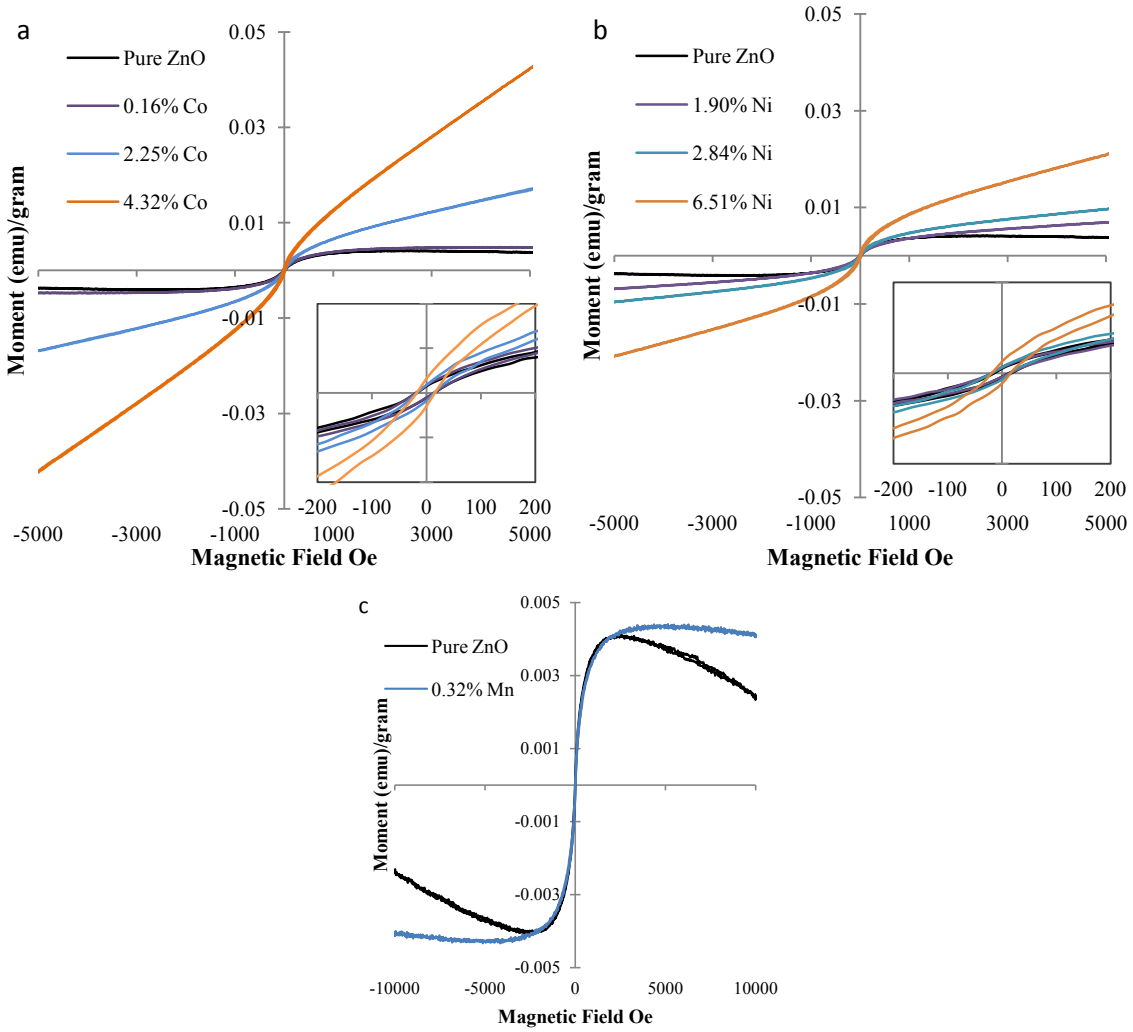

Figure 6. Magnetic spectra of Co, Mn, and Ni doped ZnO nanoparticles. (a) Comparison of Co doped materials showing increased magnetism with increased Co. (b) Comparison of Ni doped materials. (c) Pure ZnO (diamagnetic) and 0.32% Mn doped material. Insets show magnified view.

In addition to the paramagnetic component, a small ferromagnetic component appears in all curves, even the pure ZnO, with an *S* shape centered at the origin and a small hysteresis (visible in the close-ups in Fig. 6). We attribute the presence of some ferromagnetic contribution in these curves to the sample holder in the VSM instrument. And while some parasitic ferromagnetism was detected, it was less than 1% of the measurement for pure ZnO. However, the close-ups indicate a slight increase in the size and magnitude of the hysteresis in the magnetization curves for the higher concentrations

of Co and Ni-doped samples, suggesting that part of the ferromagnetic signal originates from the Co and Ni atoms. In the case of the Ni materials, the coercive field H_c is about 20 Oe and the magnetization at remanence increases from 0.0003 emu up to 0.0006 emu. In the case of the Co cobalt materials, the coercive field H_c is about 20 Oe, and the magnetization at remanence M_r increases from 0.0003 emu at 0.16% Co up to 0.0007 emu at 4.32% Co. This magnetic behavior could be due to intrinsic effects within the nanoparticles themselves such as surface or grain boundaries.[32, 33] Another cause maybe be due to O or Zn vacancies within the ZnO crystal. [34, 35] Overall, the small ferromagnetic contribution is due in most part to the sample holder, defects in the ZnO and to a small degree to the dopant. The main impact introduced by the Mn, Co, and Ni dopants remains the appearance of a paramagnetic signal of increasing magnitude with the amount of dopant.

2.4 Conclusions

Zinc oxide nanoparticles doped with Co, Mn, and Ni were synthesized from a methanolic solution of zinc acetate. The nanoparticles were 8-11 nm in diameter and wurtzite in structure. They assembled into micron-sized spheres with hollow centers. The new materials were colored and had slightly smaller band gaps than pure ZnO. Furthermore, the introduction of Co, Ni or Mn dopants induces a paramagnetic behavior that is not present in pure ZnO. The amount of paramagnetic component is the strongest in the case of Co and it increases with the amount of dopant. Our magnetization measurements also indicate the appearance of a small ferromagnetic component.

Acknowledgements

We thank Jeff Farrer and Michael Standing for TEM/SEM assistance. We appreciate the Fulbright Scholar Program for supporting TMH and JSS. We are grateful to BYU for funding and NSF for XRD instrument funding.

References

1. Özgür, Ü.; Alivov, Y. I.; Liu, C.; Teke, A.; Reshchikov, M. A.; Doğan, S.; Avrutin, V.; Cho, S.-J.; Morkoç, H. A comprehensive review of ZnO materials and devices. *J. Appl. Phys.* **2005**, *98*, 041301-103.

2. Furdyna, J. K. Diluted magnetic semiconductors. *J. Appl. Phys.* **1988**, *64*, R29-R64.

3. Furdyna, J. K., Kossut, J., Eds. *Diluted Magnetic Semiconductors*; Academic: New York, 1988; Vol. 25.

4. Bauermann, L. P.; Bill, J.; Aldinger, F. Bio-friendly synthesis of ZnO nanoparticles in aqueous solution at near-neutral pH and low temperature. *J. Phys. Chem. B* **2006**, *110*, 5182-5185.

5. Ali, M.; Friedenberger, N.; Spasova, M.; Winterer, M. A novel approach for chemical vapor synthesis of ZnO nanocrystals: optimization of yield, crystallinity. *Chem. Vap. Deposition*. **2009**, *15*, 192-198.

6. Greene, L. E.; Yuhas, B. D.; Law, M.; Zitoun, D.; Yang, P. Solution-grown zinc oxide nanowires. *Inorg. Chem.* **2006**, *45*, 7535-7543.

7. Norberg, N. S.; Kittistved, K. R.; Amonette, J. E.; Kukkadapu,R.K.; Schwartz, D. A; Gamelin, D. R. Synthesis of colloidal Mn^{2+}:ZnO quantum dots and high-T_C ferromagnetic nanocrystalline thin films. *J. Am. Chem. Soc.* **2004**, *126*, 9387-9398.

8. Tang, H.; Chang, J.C.; Shan, Y.; Lee, S.T. Surfactant-assisted alignment of ZnO nanocrystals to superstructures. *J. Phys. Chem. B* **2008**, *112*, 4016-4021.

9. Chen, L.; Xu, J.; Holmes, J. D.; Morris, M. A. A facile route to ZnO nanoparticle superlattices: synthesis, functionalization, and self-assembly. *J. Phys. Chem. C* **2010**, *114*, 2003-2011.

10. Viswanatha, R.; Sapra, S.; Gupta, S. A.; Satpati, B.; Satyam, P. V.; Dev, B. N.; Sarma, D. D. Synthesis and characterization of Mn-doped ZnO nanocrystals. *J. Phys. Chem. B* **2004**, *108*, 6303-6310.

11. Wu, Y.L.; Tok, A. I. Y.; Boey, F.Y.C.; Zeng, X.T.; Zhang, X.H. Surface modification of ZnO nanocrystals. *Appl. Surf. Sci.* **2007**, *253,* 5473-5479.

12. Singh, J.; Im, J.; Whitten, J. E. Encapsulation of zinc oxide nanorods and nanoparticles. *Langmuir* **2009**, 25(17), 9947-9953.

13. Schwartz, D. A.; Norberg, N. S.; Nguyen, Q. P.; Parker, J. M.; Gamelin, D. R. Magnetic quantum dots: synthesis, spectroscopy, and magnetism of Co^{2+}- and Ni^{2+}-doped ZnO nanocrystals. *J. Am. Chem. Soc.* **2003**, *125*, 13205-13218.

14. Garcia, et al. Magnetic properties of ZnO nanoparticles. *Nano Letters* **2007**, *7*, 1489-1494.

15. Xiong, H.; Shchukin, D.G.; Möhwald, H.; Xu, Y.; Xia, Y. Sonochemical synthesis of highly luminescent zinc oxide nanoparticles doped with magnesium(II). *Angew. Chem. Int. Ed.* **2009**, *48*, 2727-2731.

16. Wang, Y.S.; Thomas, P.J.; O'Brien, P. Optical properties of ZnO nanocrystals doped with Cd, Mg, Mn, and Fe ions. *J. Phys. Chem. B.* **2006**, *110*, 21412-21415.

17. Nayak, J. ;Kimura, S.; Nozaki, S.; Ono, H.; Uchida, K. Yellowish-white photoluminescence from ZnO nanoparticles doped with Al and Li. *Superlattice. Microstruct.* **2007**, *42*, 438-443.

18. Escudero, R.; Escamilla, R. Ferromagnetic behavior of high-purity ZnO nanoparticles. *Solid State Commun.* **2011**, *151*, 97-101.

19. Panchakarla, L. S.; Sundarayya, Y.; Manjunatha, S.; Sundaresan, A.; Rao, C. N. R. On the defect origin of the room-temperature magnetism universally exhibited by metal-oxide nanoparticles. *Chem. Phys. Chem.* **2010**, *11*, 1673-1679.

20. Singhal, A.; Achary, S. N.; Manjanna, J.; Chatterjee, S.; Ayyub, P.; Tyagi, A. K. Chemical synthesis and structural and magnetic properties of dispersible cobalt- and nickel-doped ZnO nanocrystals. *J. Phys. Chem. C* **2010**, *114*, 3422-3430.

21. Barick, K. C.; Aslam, M.; Dravid, V. P.; Bahadur, D. Self-aggregation and assembly of size-tunable transition metal doped ZnO nanocrystals. *J. Phys. Chem. C* **2008**, *112*, 15163-15170.

22. Jayakumar, O. D.; Sudakar, C.; Vinu, A.; Asthana, A.; Tyagi, A. K. Effect of surfactant treatment on the magnetic properties of Mn-doped ZnO bulk and nanoparticles. *J. Phys. Chem. C* **2009**, *113*, 4814-4819.

23. Guo, Y.; Cao, X.; Lan, X.; Zhao, C.; Xue, X.; Song Y. Solution-based doping of manganese into colloidal ZnO nanorods. *J. Phys. Chem. C* **2008**, *112*, 8832-8838.

24. Yuhas, B. D.; Zitoun, D. O.; Pauzauskie, P. J.; He, R.; Yang, P. Transition-metal doped zinc oxide nanowires. *Angew. Chem. Int. Ed.* **2006**, *45*, 420-423.

25. Ali, M.; Winterer, M. ZnO nanocrystals: surprisingly 'alive'. *Chem. Mater.* **2010**, *22,* 85-91.

26. Patterson, A. L. The Scherrer formula for X-ray particle size determination. *Phys. Rev.* **1939**, *56*, 978-982.

27. Moezzi, A.; Cortie, M.; McDonagh, A. Aqueous pathways for the formation of zinc oxide nanoparticles. *Dalton Trans*. **2011**, *40*, 4871-4878.

28. Cotton, F. A.; Wilkinson, G. *Advanced Inorganic Chemistry* 6th ed.; John Wiley & Sons, Inc. New York, 1999.

29. Shannon, R. D. Revised effective ionic radii and systematic studies of interatomie distances in halides and chalcogenides. *Acta Crys*. **1976**, *A32*, 751-767. Crystal ionic radii (pm): Zn^{2+} = 88, Co^{2+} = 88.5, Mn^{2+} = 97, Ni^{2+} = 83.

30. Makoto, M.; Yoshikawa, K.; Sakamoto, W.; Yogo, T. Size-controlled submicrometer hollow spheres constituted of ZnO nanoplates from layered zinc hydroxide. *Inorg. Chem* **2009**, *48*, 8544-8549.

31. Pradhan, D.; Leung, K. T. Template-free single-step electrochemical synthesis of ZnO hollow nanospheres: Self-assembly of hollow nanospheres from nanoparticles. *J. Mater. Chem.* **2009**, *19*, 4902-4905.

32. Schoenhalz, A. L.; Arantes, J. T.; Fazzio, A.; Dalpian, G. M. Surface magnetization in non-doped ZnO nanostructures. *Appl. Phys. Lett.* **2009**, 94, 162503.

33. Xu, Q.; Schmidt, H.; Zhou, S.; Potzger, K.; Helm, M.; Hochmuth, H.; Lorenz, M.; Setzer, A.; Esquinazi, P.; Meinecke, c.; Grudmann, M. Room temperature ferromagnetism in ZnO films due to defects *Appl. Phys. Lett.* **2008**, 92, 082508.

34. Sundaresan, A.; Bhargavi, R.; Rangarajan, N.; Siddesh, U.; Rao, C. N. R. Ferromagnetism as a universal feature of nanoparticles of the otherwise nonmagnetic oxides *Phys. Rev. B: Condens. Matter* **2006**, *74*, 161306(R).

35. Wang, Q.; Sun, Q.; Chen, G.; Kawazoe, Y.; Jena, P. Vacancy-induced magnetism in ZnO thin films and nanowires *Phys. Rev. B: Condens. Matter* **2008**, 77, 205411.

Chapter 3: Controlled ZnO Hexagonal Prism Formation with Ethanol Amines and Water

ABSTRACT

Formation of crystalline hexagonal ZnO prisms from a sol-gel method is presented. The method requires zinc acetate, water, and ethanol amine to create a gel of zinc hydroxide and zinc hydroxide acetate, which upon heating forms hexagonal prisms. By characterizing the gel with XRD and XRD high temperature chamber (HTK), it was determined that 100 ˚C was required for prism formation. SEM images showed hexagonal prisms were of uniform size (approx. 0.5 × 2 μm) with very distinct edges and were made from two halves. TEM and electron diffraction image showed the prisms were highly crystalline but had a rough surface. TEM also showed a change from randomly oriented particles in the gel to ordered crystals after heating. When the amount of water in the gel was varied, it was found that water was required to form the prisms. Also it was found that other zinc salts, such as chloride, nitrate and perchlorate did not form prisms. Water and the acetate salt of zinc proved to be critical to prism formation.

3.1 Introduction

Zinc oxide is used in many applications such as light harvesters,[1] spintronics devices,[2] catalytic supports,[3] gas detectors,[4] water splitters,[5] and semiconductors.[6] These applications result from zinc oxide being an n-type semiconductor, with a direct band gap of 3.37 eV and an exciton binding energy of 60 meV. ZnO forms in the hexagonal wurtzite crystal structure, where each zinc atom is coordinated tetrahedrally to four oxygen atoms, which then can combine over several unit cells to create a hexagonal prism (Figure 1). This noncentrosymmetric structure creates two polar planes, the positive Zn^{2+} ion rich (0001) and the negative O^{2-} $(000\bar{1})$ planes, and several nonpolar planes, including the $(10\bar{1}0)$ plane. This structure results in piezoelectric and electronic properties of ZnO, including spontaneous polarization. A higher rate of growth often occurs along the axis that contains the two high-energy Zn^{2+} and O^{2-} polar planes or along the c-axis.

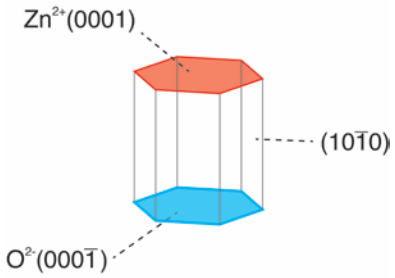

Figure 1. ZnO crystallographic structure showing the hexagonal prism shape and the polar (0001) and $(000\bar{1})$ and nonpolar $(10\bar{1}0)$ planes.

The structure and shape of ZnO is influenced by the synthetic method used to make it. Multiple synthetic methods have been tried and include chemical vapor deposition, thermal evaporation, electrodeposition, hydrothermal, sol-gel, and pulsed-laser deposition. In addition, catalysts, surfactants, and solvents are often used to alter the

ZnO growth. For example, ZnO structures of shells and cages were synthesized by vapor deposition during epitaxial surface oxidation by using SnO_2 catalysts and graphite during the synthesis.[7] A large number of structure morphologies have been formed, such as nanorods,[8] nanowires,[9] nanotubes,[10] nanobelts,[11] nanorings,[12] nanoribbons,[13] nanospheres,[14] nanotetrapods,[15] nanoflowers,[16] and nanocombs.[17] These morphologies alter the physical, chemical, and optical properties of ZnO and thus, create the ability of ZnO to be used in multiple applications.

ZnO forms from a variety of starting materials but is frequently done from a zinc salt combined with a base such as hydroxide, citrate and acetate, or an amine. The use of a different base causes changes in the ZnO structures. The base chosen can even be pivotal in forming larger micro-sized structures. The structures formed can be used in functional materials. Few defects are seen on the surface of the crystal structure.

In hydrothermal and sol-gel methods, amines, including diethanolamine (DEA)[18] and hexamethylenetetramine (HMTA),[19,20] have been included in the Zn^{2+} solutions as the ZnO nanostructures are grown. Fu et al.[18] used zinc acetate with DEA and oleic acid to synthesize highly dispersed nanoparticles. Recently, there have been reports of synthesizing hexagonal prisms using other amines than DEA or HMTA, though there are few cases. Researchers have made ZnO hexagonal prisms with zinc nitrate and sodium dodecylbenzenesulfonate[21] or urea.[22] Also, a solution of zinc acetate with cetyltrimethylammonium bromide was shown to form large hexagonal crystals of ZnO.[23]

We present the controlled synthesis of crystalline hexagonal ZnO. Zinc acetate, alcohol amines, water, and heat are necessary for prism formation. The first step produces a gel of $Zn(OH)_2/Zn(C_2H_3O_2)(OH)$ after water has been added to a $Zn(C_2H_3O_2)_2$ solution.

The gel is composed of 2-3 nm particles. When the gel is heated to 100 ˚C in the presence of water, hexagonal prisms form. The prisms were found to be highly crystalline by XRD, SEM and TEM, including single crystal diffraction patterns by TEM.

3.2 Experimental Section

3.2.1 Synthesis of prisms

All chemicals were used as received from the manufacturer. In a general synthesis of ZnO hexagonal prisms, zinc acetate dihydrate (2.1950 g, 10.0 mmol) and two equivalents (20.0 mmol) of DEA were dissolved in 50 mL of methanol. Water (50 mL) was added to the solution and a white gel formed. The mixture was centrifuged and the gel collected. Water (~30 mL) was added to the gel, and it was sonicated for 10 minutes, centrifuged, and excess water was poured off of the gel. This step was repeated three times. The wet gel was then heated *en masse* at 100 °C for 8 hours and ZnO hexagonal prisms (0.500 g, 6.10 mmol) were obtained.

The general synthesis was altered to determine the affects of the water content, DEA, and zinc acetate salt. Water content of the gel was found by heating air-dried gel at 100 ˚C for 48 h. NMR samples of the wet and air-dried gel were prepared in D_2O and deuterated trifluoracetic acid to determine the amounts of acetate and DEA. To understand the role of DEA in the formation of prisms, other amines, including ethanolamine, triethanolamine, methylamine, triethylamine, diisopropylmethylamine, oleylamine, ethylenediamine, triethylenetetramine, diethylenetriamine, and hexamethylenetetramine, as well as sodium hydroxide, were used in place of DEA. The synthesis was altered by using other zinc salts, $Zn(NO_3)_2 \cdot 6H_2O$, $Zn(ClO_4)_2 \cdot 2H_2O$, and

$ZnCl_2$ (10.0 mmol) in place of the $Zn(C_2H_3O_2)_2 \cdot 2H_2O$ with the same amounts of DEA, methanol and water.

3.2.2 Characterization

X-ray diffraction (XRD) was performed on a PANalytical X'Pert Pro diffractometer with a Cu source and a Ge monochromator tuned to the Cu-Kα1 wavelength (λ = 1.540598 Å). Each material was scanned from 5–80° 2θ with a step size of 0.0423°/s. The patterns were matched to a standard pattern in the ICDD (International Center for Diffraction Data) database. Variable temperature XRD measurements were taken with the HTK 1200N high-temperature oven-chamber by Anton Paar. Spectra were obtained at 25 ˚C and 5 °C increment afterwards with a ramp rate of 10 ˚C per minute and a wait time of 30 seconds before the scan was initialized. Crystallite sizes were estimated using the Scherrer formula (Eq 3.1) for size-related peak broadening where D is the particle size, k is a constant of 0.9, λ is the X-ray wavelength, θ is the Bragg's angle in radians, and B is the full width at half maximum of the θ peak used.[24]

$$D = \frac{k\lambda}{B\cos\theta} \tag{3.1}$$

Transmission electron microscope (TEM) images were taken with a FEI Tecnai F20 Ultra-Twin TEM/STEM operating at 200kV, equipped with a Si(Li) X-ray energy dispersive spectrometry (XEDS) detector, model EDAX PV 9761/55 ME with 30 mm^2 active area and a super-ultra thin window (SUTW). Scanning electron microscopy (SEM) images were taken on a FEI Helios Nanolab 600. Focused ion beam (FIB) samples were coated with an AuPd (60:40) layer that was deposited to about 15 nm in thickness before milling. ^1H NMR spectra were recorded using a VXR 500-MHz multinuclear FT-NMR spectrometer.

3.3 Results and Discussion

3.3.1 Hexagonal prism formation

During our synthetic work on ZnO structures, we added diethanolamine to a methanol solution of zinc acetate, which process hadn't previously been researched. Unlike what usually occurs when no DEA is present, no precipitate formed. We noted, however, that upon addition of water, a gel formed, which was washed with water. The wet gel when heated for 8h at 100 ˚C formed a white, free flowing material that was analyzed by XRD. Comparing the XRD pattern of the new material with standard wurtzite ZnO showed that the material was ZnO in the hexagonal wurtzite structure (Figure 2). The sharp XRD peaks indicated that the new material was highly crystalline.

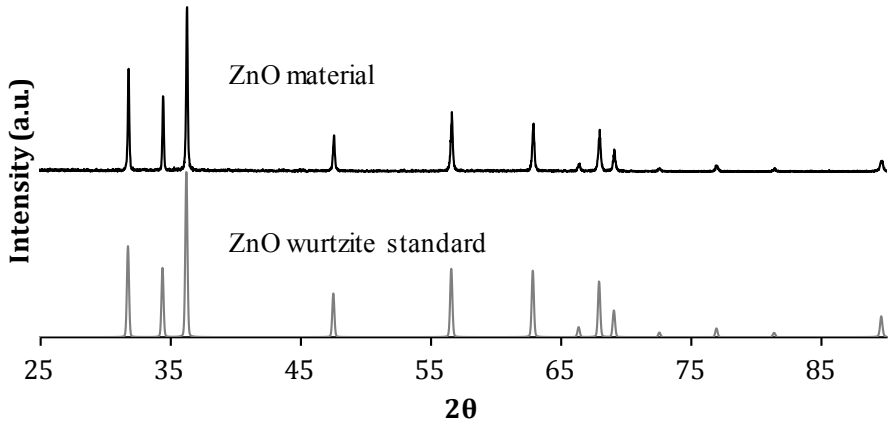

Figure 2. XRD pattern of the newly synthesized ZnO material (top) and wurtzite standard (bottom).

The ZnO material was further characterized by scanning electron microscopy (SEM). The SEM images showed the solid crystalline ZnO was made of hexagonal prisms (Figure 3a). Each prism was made of two halves, equally sized, joined at the center. There is only a slight, if any, offset between the faces and edges of the two halves. Most of the prisms were approximately 2 μm in length and 500 nm in width (Figure 3b).

Growth on the two polar planes, the positively charged (0001) and the negatively charged $(000\bar{1})$ planes, or along the longitudinal axis is preferred[25] as seen by the longer length than width.

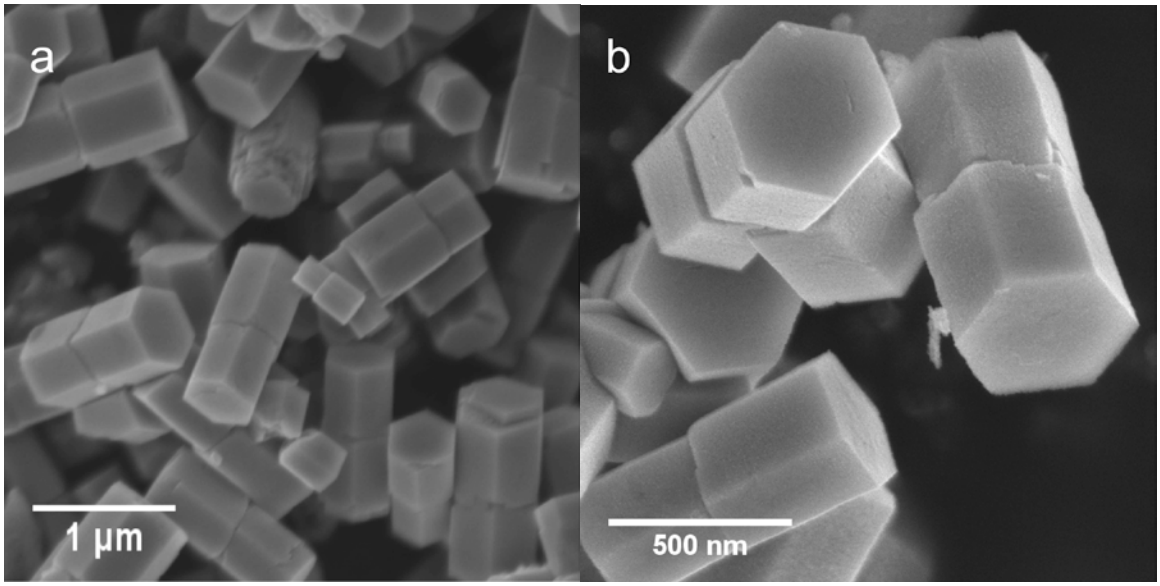

Figure 3. SEM images of ZnO hexagonal prisms. (a) Hexagonal prims. (b) Image showing the average size of the prisms, 0.5 µm × 2µm.

After analysis by SEM, a closer look of the structures was performed by TEM. Images of the hexagonal prisms showed their surface were somewhat rough but still with clearly defined edges (Figure 4). The diffraction pattern of the prisms was similar to that of a single crystal of ZnO (Figure 4c). In the diffraction pattern, a blurring of the points was seen rather than the clear spots expected in a single crystals. This blurring was caused from the rough surface on the crystal or from slight variations of the material as the prisms grew or assembled. The rough surface could be caused by small particles of ZnO material that was available in the solution interacting with the edges of the crystals.[26,27]

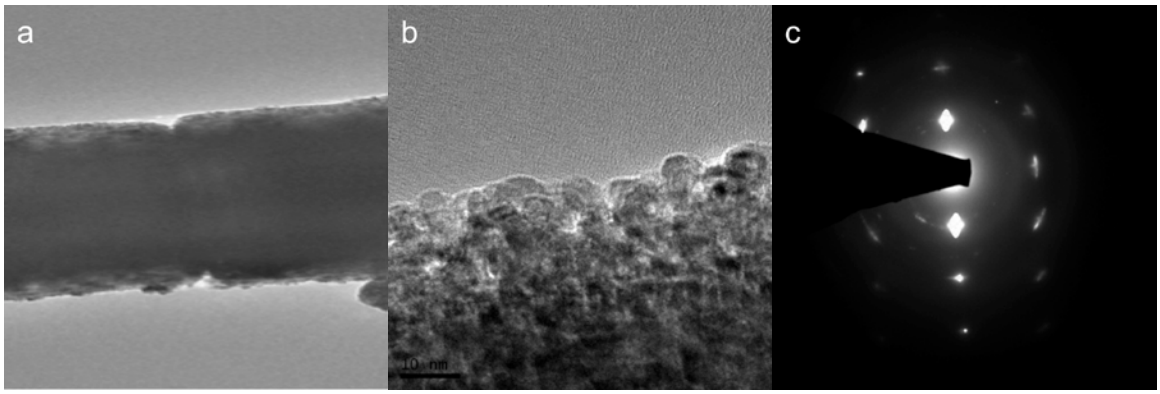

Figure 4. TEM images of a ZnO prism showing (a) & (b) a rough surface. (c) Diffraction pattern of a hexagonal prism showing a pattern associated with a single crystal but with some blurring of the diffracted points.

We noted that some batches of material contained prisms that were broken in half. Most of the prisms were solid, but some that were broken were found to have hollow cores (Figure 5). We wondered if the fully intact prisms had hollow cores. A focused ion beam (FIB) was used to cut the ZnO prisms and as shown in Figure 5, the prisms were found to be solid. Small pores were found in some prisms (Figure 5b and c), with pores ranging in size from 5–30 nm. The pores could be caused from slight variations when the prisms were formed.

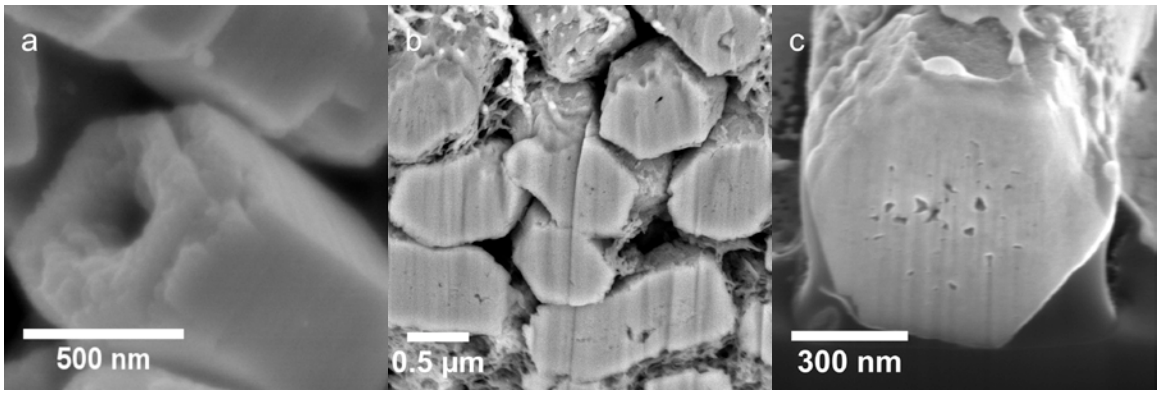

Figure 5. SEM images of the ZnO prisms. (a) Broken hexagonal prism showing the cup shape. (b and c) Ion milled prisms showing solid prism with small cavities.

3.3.2 Roles of water, diethanol amine, and zinc acetate

The synthetic procedure was altered to confirm the importance of water, DEA, and acetate. Addition of water was found to be important to the formation of prisms. When the gel was not rinsed with water, XRD spectra showed an increase in peak width due to nanoparticle formation as well as impurity peaks. The synthesis, including DEA, was done but with ethanol washings instead of water. This also caused formation of nanoparticles (Figure 6) and no prisms were detected. Thus, water left by rinsing the gel with water was critical to the formation of the ZnO hexagonal prisms. Small amounts of the air-dried gel were heated with differing amounts of water to determine the minimal amount of water needed to form prisms. Without water, amorphous ZnO formed. It was found that the air-dried gel to water ratio of 1:3 was needed for optimal prism formation.

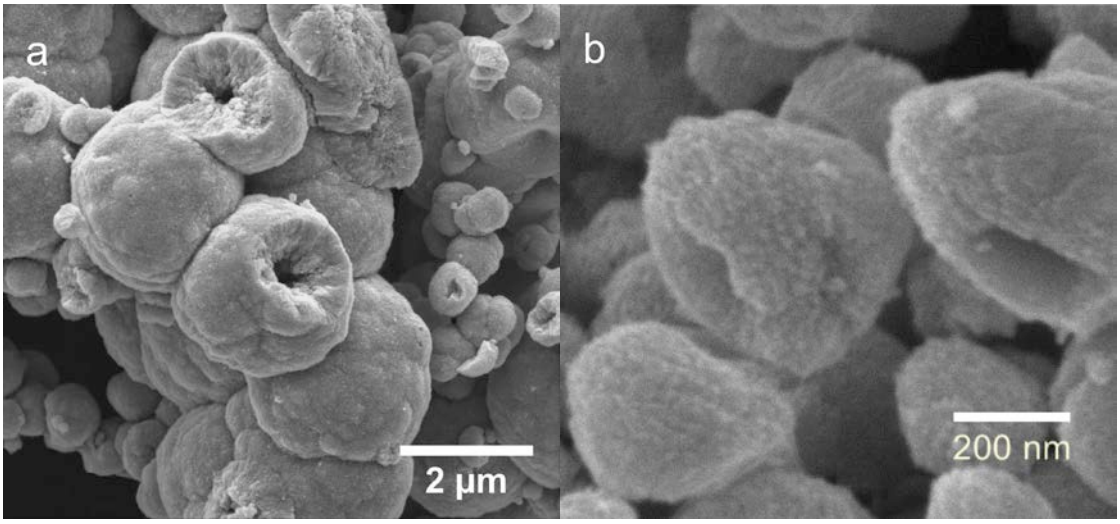

Figure 6. SEM images of alterations to the synthesis of ZnO hexagonal prisms. (a) Secondary assembly when DEA was not used during the synthesis. Nanoparticles of ZnO make up the surface of the sphere. (b) Effect of using ethanol instead of water to rinse the gel. Nanoparticles are also seen on the surface of the spheres

The second alteration was to exclude DEA or exchange it with another amine. Gel was not formed upon addition of water, although heating caused precipitation. The

precipitate was analyzed by SEM, and the secondary structure was spherical with nanoparticles easily seen on the surface (Figure 6a). There was no evidence of the hexagonally shaped prisms.

To understand the importance of DEA, other types of amines such as ethanol amines, alkyl amines, and polyamines were used in place of DEA. Sodium hydroxide was also used as a control. As with DEA, ethanolamine and triethanol amine (TEA) resulted in gel and promoted the formation of hexagonal prisms (Figure 7a and b). When DEA and TEA are used in the synthesis, very good three-dimensional formation of the hexagonal prisms was seen, whereas the structures from the ethanolamine solution were somewhat deformed in hexagonal prism shape. We propose this is caused from the lack of multiple alcohol groups on the amine. The alkyl amines (methylamine, triethylamine, diisopropylmethylamine, and oleylamine) and NaOH solutions did not form gel (Table 1). They all formed precipitates, which were composed of nanoparticles varying from 8–30 nm in size (determined by the Scherrer formula (Eq 3.1)) with no overall secondary structure (Figure 9 c–e). We also tried hexamethylenetetramine (HMTA), which formed a precipitate and nanoparticles similar to the alkyl amines. No gel or precipitates formed with the polyamines (ethylenediamine, triethylenetetramine, and diethylenetriamine). These polyamines are known to coordinate more strongly than water or an alcohol group to a Zn^{2+}. This keeps the Zn^{2+} solvated, with water unable to coordinate with each Zn^{2+} forming the gel. Of importance is that gel was formed only with the ethanol amines and that they formed prisms.

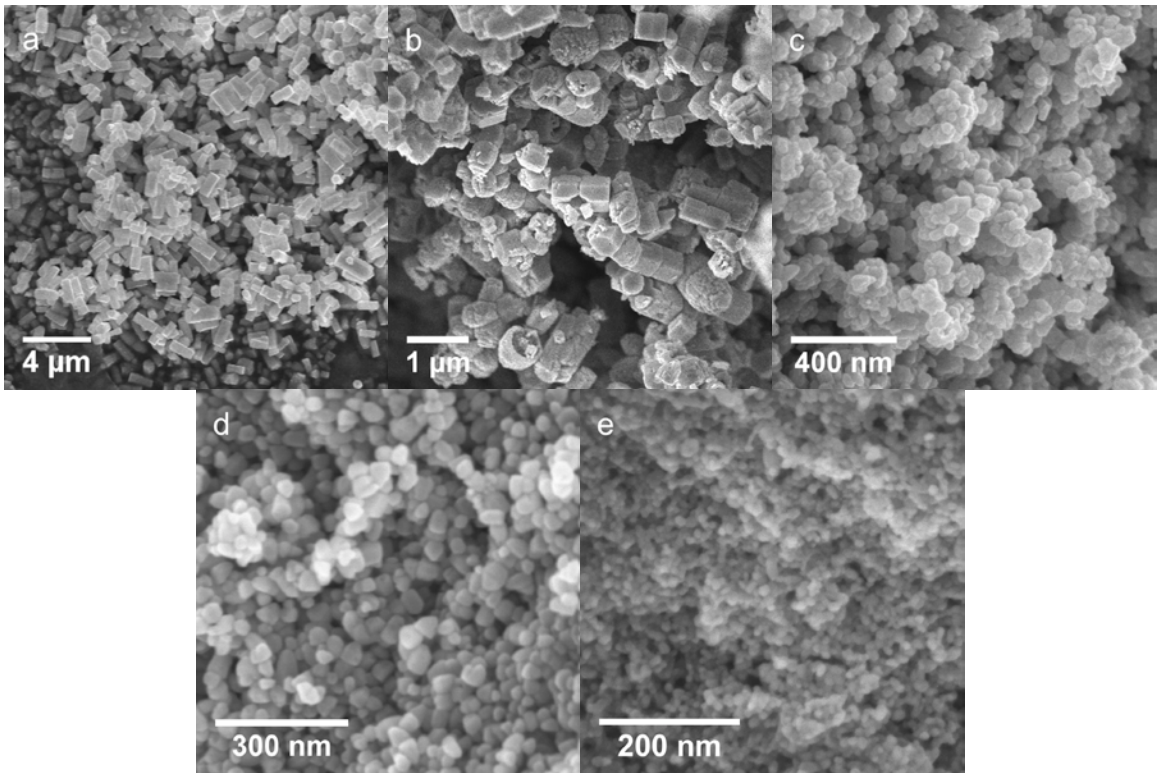

Figure 9. SEM images of materials formed by various amines and NaOH. (a) TEA, (b) ethanolamine, (c) methylamine, (d) triethylamine, and (e) NaOH.

Table 1. Comparison of ZnO structures formed from different bases. Bases were added to methanol solutions of $Zn(C_2H_3O_2)_2$.

Base	Structure	pH
no amine	NP (10 nm)	6.1
ethanolamine	prisms	8.3
diethanolamine	prisms	8.0
triethanolamine	prisms	7.0
methylamine	NP (28 nm)	9.5
triethylamine	NP (27 nm)	8.5
diisopropylmethylamine	NP (21 nm)	7.4
oleylamine	NP (14 nm)	8.5
ethylenediamine	no solid	8.5
triethylenetetramine	no solid	9.5
diethylenetriamine	no solid	9.5
hexamethylenetetramine	NP (27 nm)	7.0
sodium hydroxide	NP (12 nm)	7.9

Other zinc salts, such as zinc nitrate, zinc perchlorate, and zinc chloride, were used in place of zinc acetate with DEA. Zinc perchlorate and zinc nitrate did form gel upon addition of water, but ZnO nanoparticles (18 and 34 nm respectively) were formed instead of prisms. The zinc chloride formed a gel also, but XRD analysis showed multiple peaks without wurtzite being prominent, and SEM images did not show nanoparticles or prisms.

3.3.3 Precursors to ZnO hexagonal prisms

When synthesizing the hexagonal prisms, we noticed that the formation of the gel was critical. The gel forms when water is added to the methanol solution. We first looked at the differences between wet and air-dried gel through XRD. SEM and TEM were then employed. Finally, XRD HTK was used to determine at which temperature ZnO formation occurred.

There was little difference in the XRD spectra of the wet and air-dried gels (Figure 10). Also, the XRD pattern showed that the gel was not composed of ZnO in the wurtzite structure, but it matched standard XRD spectra of $Zn(OH)_2$ and $Zn(C_2H_3O_2)(OH)$.

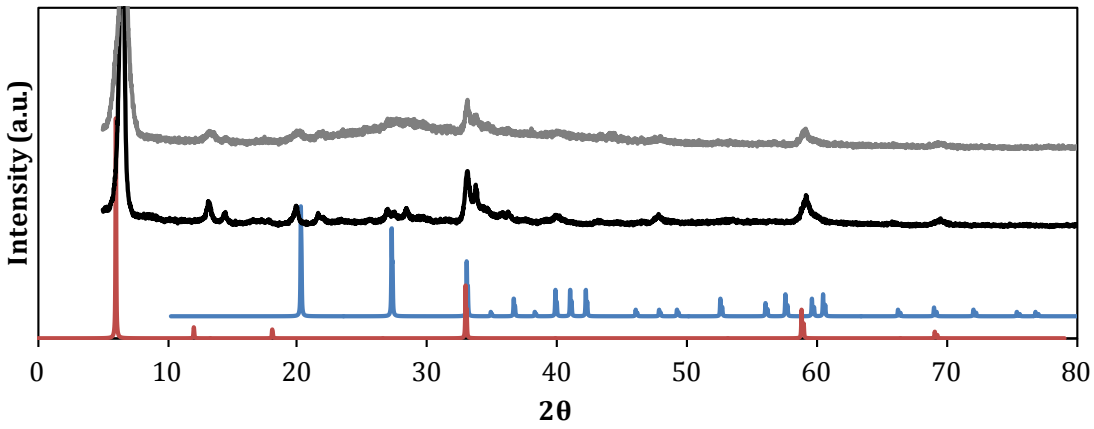

Figure 10. XRD spectra of the wet (–) and dried (–) gel compared to $Zn(OH)_2$ (–) and $Zn(C_2H_3O_2)(OH)$ (–) standards.

TEM images showed that there were small particles, 2-3 nm in size (Figure 11). According to XRD, these were a mixture of $Zn(OH)_2$ and $Zn(C_2H_3O_2)(OH)$. The diffraction pattern of the gel showed that there are randomly oriented crystals (ring distribution pattern) in the gel itself (Figure 11 inset). When SEM pictures of the gel were taken, no ordered structure was seen

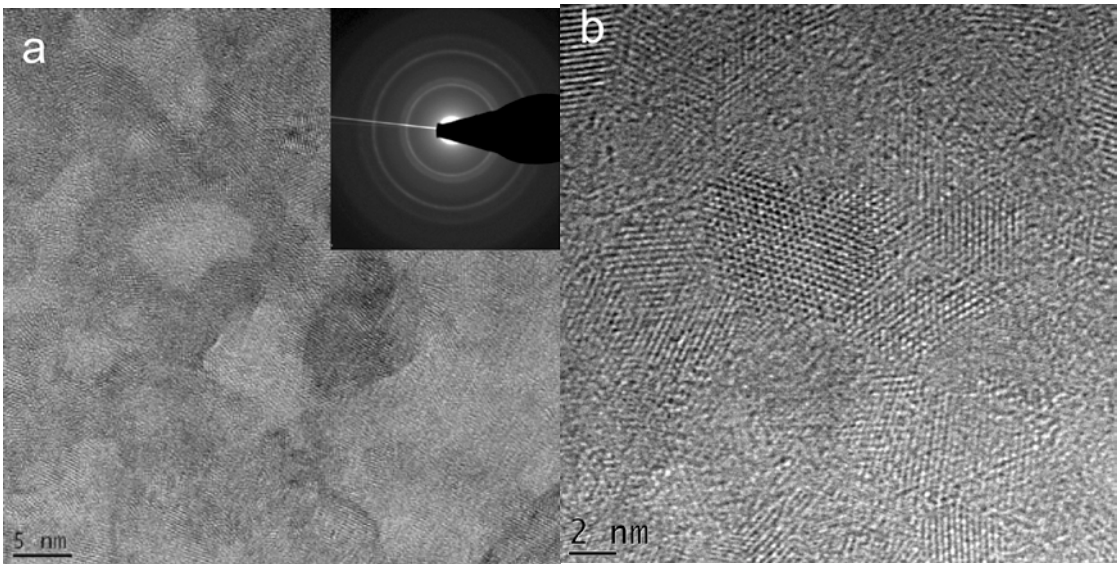

Figure 11. TEM images of gel showing nanoparticle aggregation (a) High resolution of nanoparticles with diffraction pattern inset (b) High resolution showing 2-3 nm particles.

Although DEA was important to gel formation, it was only found in minute amounts in the gel and prisms. The gel and prisms were dissolved in deuterated water by acidifying them and then their ^{1}H NMR spectra were taken. Only a small amount of DEA was detected (0.10 mM), seventy times less than the amount of acetate present (7.7 mM). We propose DEA coordinates to zinc ions and traps water in its structure, which results in gel formation.

Water loss was studied through simple mass difference and TGA. Mass loss of the sample by heating was investigated first. Air-dried samples of the gel were weighed and then heated at 100 ˚C for 48 h. An equal number of equivalents of water to ZnO, one equivalent of water for every equivalent of ZnO, were found (Eq 3.2). TGA showed a 34% loss of mass by the gel upon heating. The mass loss occurred at 125 ˚C with a corresponding DSC peak showing a chemical change at that temperature. Gas chromatography was run during the TGA experiment and water vapor was the only gas detected. When gel is heated, water is released and ZnO forms (Eq 3.2).

$$Zn(OH)_2/Zn(OH)(C_2H_3O_2) \xrightarrow{\Delta} ZnO + H_2O/HC_2H_3O_2 \qquad (3.2)$$

Because heating of the gel is necessary for prism formation, we ran XRD sampling with a temperature controlled heating stage. Both air-dried gel and wet gel were tested. Samples were placed on the HTK stage and heated from 25 ˚C to 150 ˚C with XRD spectra taken every 5 ˚C (Figure 12). Between 90–95 ˚C, there was a change from the zinc hydroxide/acetate pattern to the ZnO wurtzite pattern.

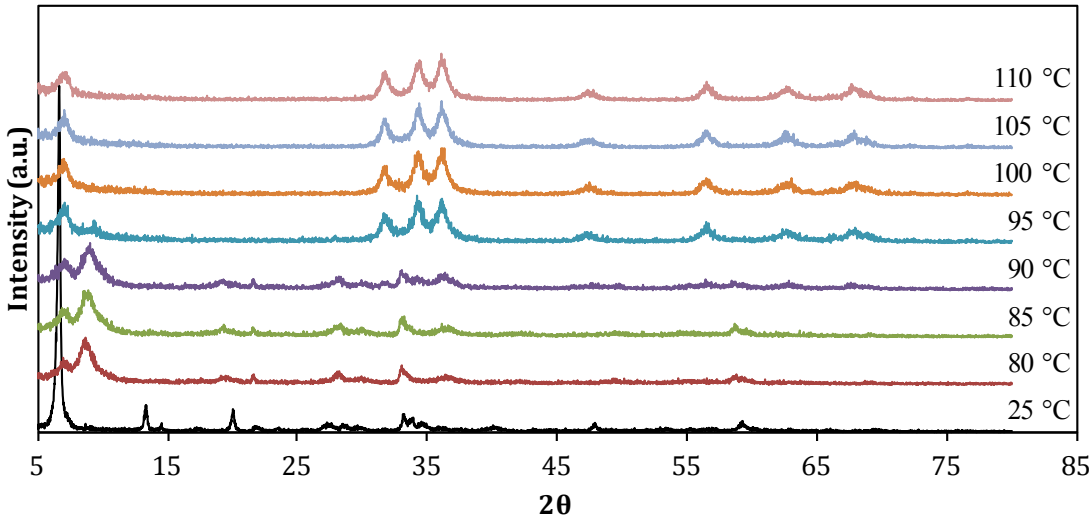

Figure 12. XRD HTK of the gel to ZnO prisms. The wurtzite structure is seen at 95 ˚C.

Although the XRD spectra show ZnO formation at 95 ˚C, this material is not made of hexagonal prisms but of nanoparticles. This can be seen by the broad XRD peaks in Figure 10 instead of the sharp peaks seen in Figure 2. We tried the same process of heating the gel on a TEM stage. The gel was heated to 100 ˚C, while watching for prism formation and correcting for drift. Prisms did not form, but nanoparticles did. This was probably due to the high vacuum conditions of the TEM instrument where any water that was released would be immediately removed from the water, preventing assembly of the ZnO material into hexagonal prisms. However, diffraction patterns did show a change from the hydroxide precursor to the ZnO wurtzite structure. We believe that water slows the growth of the ZnO and this allows for the large prism structures to form. Heating without excess water, like in the XRD HTK stage or TEM chamber, disrupts prism formation.

$$Zn(C_2H_3O_2)_2 + DEA + H_2O \rightarrow Gel \xrightarrow{\Delta} Prisms \qquad (3.3)$$

To summarize, four factors were found to control the growth of ZnO hexagonal prisms. Diethanol amine was important in the formation of gel and trapping of water, which was needed for ZnO hexagonal prism formation. Other ethanolic amines resulted in prism formation. Zinc acetate was critical in prism formation as well. Other zinc salts were unsuccessful in promoting prism formation. Excess water was needed to obtain prisms from the gel, otherwise without water nanoparticles formed. Lastly, heat was needed for the gel needed to reach a temperature of 100 ˚C for several hours. While hexagonal prisms have been reported to form, examples are few.[21-23] Hexagonal prism formation in a controlled method with DEA and zinc acetate is new.

3.4 Conclusion

We have reported on a controlled procedure to produce ZnO hexagonal prisms through a sol-gel method of zinc acetate, DEA, and water. We have found four factors critical to prism formation. The prisms have preferential growth along the polar planes of the wurtzite crystal. Water, DEA and zinc acetate were investigated and found to be necessary in controlling the formation of the prisms. The gel precipitated from water was found to contain small nanoparticles made of zinc hydroxide/acetate. TEM diffraction pattern images show a change from randomly oriented nanoparticles in the gel to a highly ordered single crystal structure.

References

1. Ko, S. H.; Lee, D.; Kang, H. W.; Nam, K. H.; Yeo, J. Y.; Hong, S. J.; Grigoropoulos, C. P.; Sung, H. J., Nanoforest of Hydrothermally Grown Hierarchical ZnO Nanowires for a High Efficiency Dye-Sensitized Solar Cell. *Nano Lett.* **2011,** *11*, 666–671.

2. Sharma, P.; Gupta, A.; Rao, K. V.; Owens, F. J.; Sharma, R.; Ahuja, R.; Guillen, J. M. O.; Johansson, B.; Gehring, G. A., Ferromagnetism above room temperature in bulk and transparent thin films of Mn-doped ZnO. *Nat. Mater.* **2003,** *2*, 673–677.

3. Llorca, J.; Homs, N.; Sales, J.; Ramirez, d. l. P. P., Efficient Production of Hydrogen over Supported Cobalt Catalysts from Ethanol Steam Reforming. *J. Catal.* **2002,** *209*, 306–317.

4. Wan, Q.; Li, Q. H.; Chen, Y. J.; Wang, T. H.; He, X. L.; Li, J. P.; Lin, C. L., Fabrication and ethanol sensing characteristics of ZnO nanowire gas sensors. *Appl. Phys. Lett.* **2004,** *84*, 3654–3656.

5. Maeda, K.; Takata, T.; Hara, M.; Saito, N.; Inoue, Y.; Kobayashi, H.; Domen, K., GaN:ZnO Solid Solution as a Photocatalyst for Visible-Light-Driven Overall Water Splitting. *J. Am. Chem. Soc.* **2005,** *127*, 8286–8287.

6. Norton, D. P.; Heo, Y. W.; Ivill, M. P.; Ip, K.; Pearton, S. J.; Chisholm, M. F.; Steiner, T., ZnO: Growth doping and processing. *Mater. Today (Oxford, U. K.)* **2004,** *7*, 34–40.

7. Gao, P. X.; Wang, Z. L., Mesoporous Polyhedral Cages and Shells Formed by Textured Self-Assembly of ZnO Nanocrystals. *J. Am. Chem. Soc.* **2003,** *125*, 11299–11305.

8. Liu, B.; Zeng, H. C., Hydrothermal Synthesis of ZnO Nanorods in the Diameter Regime of 50 nm. *J. Am. Chem. Soc* **2003,** *125*, 4430–4431.

9. Vayssieres, L., Growth of Arrayed Nanorods and Nanowires of ZnO from Aqueous Solutions. *Adv. Mater.* **2003,** *15*, 464–466.

10. Lam, S.-M.; Sin, J.-C.; Zuhairi Abdullah, A.; Rahman Mohamed, A., Green hydrothermal synthesis of ZnO nanotubes for photocatalytic degradation of methylparaben. *Mater. Lett.* **2013,** *93*, 423–426.

11. Pan, Z. W.; Dai, Z. R.; Wang, Z. L., Nanobelts of semiconducting oxides. *Science* **2001,** *291*, 1947–1949.

12. Wu, X.; Qu, F.; Zhang, X.; Cai, W.; Shen, G., Fabrication of ZnO ring-like nanostructures at a moderate temperature via a thermal evaporation process. *J. Alloys Compd.* **2009,** *486*, L13–L16.

13. Gao, P.; Wang, Z. L., Self-Assembled Nanowire−Nanoribbon Junction Arrays of ZnO. *J. Phys. Chem. B* **2002,** *106*, 12653–12658.

14. Zhu, C.; Lu, B.; Su, Q.; Xie, E.; Lan, W., A simple method for the preparation of hollow ZnO nanospheres for use as a high performance photocatalyst. *Nanoscale* **2012,** *4*, 3060–3064.

15. Qiu, Y.; Yang, S., ZnO nanotetrapods: controlled vapor-phase synthesis and application for humidity sensing. *Adv. Funct. Mater.* **2007,** *17*, 1345–1352.

16. Pan, A.; Yu, R.; Xie, S.; Zhang, Z.; Jin, C.; Zou, B., ZnO flowers made up of thin nanosheets and their optical properties. *J. Cryst. Growth* **2005,** *282*, 165–172.

17. Zang, C. H.; Liu, Y. C.; Zhao, D. X.; Zhang, J. Y.; Shen, D. Z., The synthesis and optical properties of ZnO nanocombs. *J. Nanosci. Nanotechnol.* **2010,** *10*, 2370–2374.

18. Fu, Y. S.; Du, X. W.; Kulinich, S. A.; Qiu, J. S.; Qin, W. J.; Li, R.; Sun, J.; Liu, J., Stable Aqueous Dispersion of ZnO Quantum Dots with Strong Blue Emission via Simple Solution Route. *J. Am. Chem. Soc.* **2007,** *129*, 16029–16033.

19. Jang, W. S.; Lee, T. I.; Oh, J. Y.; Hwang, S. H.; Shon, S. W.; Kim, D. H.; Xia, Y.; Myoung, J. M.; Baik, H. K., Kinetically controlled way to create highly uniform mono-dispersed ZnO sub-microrods for electronics. *J. Mater. Chem.* **2012,** *22*, 20719–20727.

20. Sugunan, A.; Warad, H. C.; Boman, M.; Dutta, J., Zinc oxide nanowires in chemical bath on seeded substrates: Role of hexamine. *J. Sol-Gel Sci. Technol.* **2006,** *39*, 49–56.

21. Zhang, X. L.; Qiao, R.; Qiu, R.; Kim, J. C.; Kang, Y. S., Fabrication of Hierarchical ZnO Nanostructures via a Surfactant-Directed Process. *Cryst. Growth Des.* **2009,** *9*, 2906–2910.

22. Bitenc, M.; Dražić, G.; Orel, Z. C., Characterization of Crystalline Zinc Oxide in the Form of Hexagonal Bipods. *Cryst. Growth Des.* **2010,** *10*, 830–837.

23. Hou, H.; Xie, Y.; Li, Q., Structure-directing self-organized, one-dimensional ZnO single-crystal whiskers. *Solid State Sciences* **2005,** *7*, 45–51.

24. Patterson, A., The Scherrer Formula for X-Ray Particle Size Determination. *Physical Review* **1939,** *56*, 978–982.

25. Meagley, K. L.; Garcia, S. P., Chemical Control of Crystal Growth with Multidentate Carboxylate Ligands: Effect of Ligand Denticity on Zinc Oxide Crystal Shape. *Cryst. Growth Des*. **2012,** *12*, 707–713.

26. Sun, S.; Zhang, X.; Zhang, J.; Song, X.; Yang, Z., Unusual Designated-Tailoring on Zone-Axis Preferential Growth of Surfactant-Free ZnO Mesocrystals. *Cryst. Growth Des*. **2012,** *12*, 2411–2418.

27. Ye, F.; Peng, Y.; Chen, G.-Y.; Deng, B.; Xu, A.-W., Facile Solution Synthesis and Characterization of ZnO Mesocrystals and Ultralong Nanowires from Layered Basic Zinc Salt Precursor. *J. Phys. Chem. C* **2009,** *113*, 10407–10415.

Chapter 4: Optical Properties of Oligothiophene-Ruthenium Complexes Bound to CdSe Nanoparticles[1,2]

ABSTRACT

Molecular conjugates are important to link photocell sensitizers to electron acceptors. We have synthesized oligothiophenes and oligothiophene-ruthenium complexes and bound them to CdSe nanoparticles to test their ability to act as sensitizers and charge transfer junctions. The absorption and fluorescence properties of the oligothiophenes bound to CdSe were measured. Steady-state luminescence and time correlated single photon counting were used to observe the effects of fluorescence and fluorescence lifetimes before and after binding. It was found that fluorescence of CdSe nanoparticles was quenched when they were bound to the oligothiophenes, and that the fluorescence of the oligothiophenes was also quenched. The fluorescence lifetimes of the quenched species were shortened.

[1] Parts include previously published work Bair, N. S. Synthesis and characterization of an oligothiophene-ruthenium complex and synthesis and optical properties of oligothiophene-ruthenium complexes bound to CdSe nanoparticles, Thesis, Brigham Young University, 2010, Used with permission.

[2] My contributions included the absorbance and fluorescent measurements. I also plotted and calculated Stern-Volmer constants. Nathan Bair and Cameron Simonsen prepared the organic synthetic procedures. Scott Thalman, John S. Colton, and Matthew C. Asplund helped with single photon measurements and calculations.

4.1 Introduction

A variety of materials have been used in solar cells to absorbs light, materials such as organic dyes,[1] organic polymers[2,3] including polythiophenes,[4,5] inorganic quantum dots,[6,7] metal ion dyes,[8,9] and bulk silicon.[10] Organic solar cells commonly contain an organic polymer, conjugated oligomer, or metal-containing organic dye. Organic solar cells, specifically organic photovoltaic devices, often have an electron donor/acceptor interface. By inserting a charge transfer junction between the donor and acceptor, the charge injection rate can be increased. This charge transfer junction acts as an electron conduit to separate the exciton into a free charge carrier with the electron hole left behind. Oligothiophenes show promising electron and hole mobilities, both key properties for charge transfer junctions.[11-18] They have been used as both electron donor and charge transfer junctions.[13] Oligothiophenes are a well-studied class of compounds due primarily to their electronic structure.[19-21] Their highly conjugated electronic structure makes oligothiophenes useful as fluorescent materials in organic light emitting diodes, electron conductors in organic field effect transistors, active phases in organic solar cells, and bridges at electron donor/acceptor interfaces.

In the case of organic dyes, oligothiophenes have been used as charge transfer junctions and bound directly to an electron donor.[14] When constructed this way, the oligothiophene may have the added effect of red shifting the absorbance and increasing the molar extinction coefficient of the dye. These effects were demonstrated by a set of compounds that vary in the number of oligothiophenes.[15] In these compounds, the peak absorption of the dye was broadened when thiophenes were bound to it and the molar extinction coefficient increased with increasing oligothiophene chain length.

Oligothiophenes can also be electronically connected to metal-containing dyes by being covalently bonded to metal-coordinating ligands.[22-26] In many cases, Ru is the metal of choice and bipyridines are coordinated to it. It was found that the number of injected electrons increased when thiophenes were included as the charge transfer junction with Ru dyes.[27]

Oligothiophenes can be equipped with anchoring groups to attach them to nanoparticle acceptors such as TiO_2. Both cyanoacrylic acid and cyanoacetic acid moieties have been used.[13-15,28] Along with TiO_2 nanoparticles, CdSe nanoparticles are also common electron acceptors.[29] Carboxylic acids[30] and phosphonic acids[31] have been used as anchoring groups to CdSe nanoparticles. Of these, the phosphonic acid moiety binds strongly to CdSe nanoparticles, whether the thiophenes are in a linear chain[32] or branched configuration.[33] There has been some disagreement on the right thiophene chain length for optimal CdSe nanoparticle electron transfer. It was demonstrated that a pentathiophene quenched CdSe fluorescence, while a terthiophene caused an increase in CdSe fluorescence.[32] In contrast, while testing dendron oligothiophenes, it was shown that charge transfer occurred with thiophenes with fewer than five subunits.[33] In another study that used oligothiophenes bonded to organic dye, a two thiophene chain link was the optimum length.[34] And yet in another study, it was found that thiophenes of 2 and 3 enhanced CdSe fluorescence.[35] In summary, the optimal oligothiophene chain length depends on the system's specific donor and acceptor and further study is needed to understand the best number of thiophene subunits.

Not only are nanoparticles used as electron acceptors, they can act as electron donors in quantum dot solar cells, which are made with CdS,[36] CdSe,[7] and CdTe[37]

nanocrystals. Quantum confinement gives quantum dot solar cells the ability to be tuned to different wavelengths of light. CdSe nanoparticles have been used as sensitizer with TiO_2 nanoparticles on an optically transparent conducting glass electrode.[38] In these materials, a connecting molecule (mercaptopropionic acid) was used to link the two nanoparticle types together. The carboxylic acid group was bound to the TiO_2 followed by binding of the thiol to CdSe.

We have synthesized molecules to act as charge transfer junctions that link sensitizers and electron acceptors. These molecules are unsymmetrical oligothiophenes that contain bipyridine groups on one end and phosphate groups on the other (Figure 1, compounds **1, 2, 5, 6**).[39] The molecules are designed to incorporate an electron donor, Ru(II), along with a charge transfer junction, oligothiophene, and bind to an electron acceptor, CdSe nanoparticle. Thus, the bipyridine groups were installed to chelate to $Ru(bpy)_2^{2+}$ and the phosphate groups were included to bind to electron acceptors such as nanoparticles. In previous studies, the tetrathiophenes showed smaller HOMO-LUMO band gaps than the bithiophenes, as seen by their red-shifted absorbance. Not only did the $Ru(bpy)_3^{2+}$ groups act as sensitizers, but the thiophenes did as well and the fluorescence of both of these groups was quenched when they were bound together.

In this paper, we report on the binding of the di- and tetrathiophenes, and the complimentary trithiophene to CdSe nanoparticles. The UV-vis and fluorescence measures were performed on the thiophene nanoparticle assemblies. For the new trithiophenes (compounds **2** and **5**), we present their synthetic procedure and detailed characterization, including UV-vis and fluorescence spectroscopies. The oligothiophenes have lengths of two, three and four units, allowing us to investigate the optimum

thiophene chain length for this charge transfer junction. An important property of these oligothiophenes is their low-lying LUMOs, which promote exciton dissociation. Indeed, as shown by the optical properties of these thiophenes bound to CdSe nanoparticles, communication between thiophenes and nanoparticles is realized.

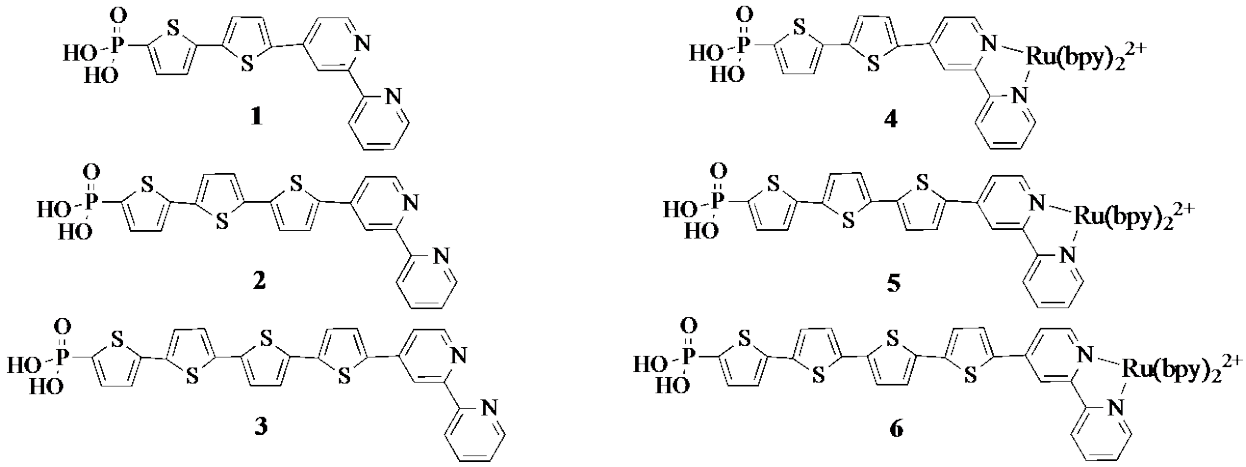

Figure 1. Oligothiophene molecules (**1**, **2**, **3**) and their $Ru(bpy)_2^{2+}$ compounds (**4**, **5**, **6**).

4.2 Results and Discussion

Compounds **1**, **3**, **4**, and **6** were synthesized as reported in the literature.[39] To synthesize the new trithiophenes, thiophene units were made in two sections and coupled together (Scheme 1). One section is made with a phosphate ester group and two thiophene rings, while the other section has a bipyridine group and one thiophene ring. One of the initial steps of the synthesis is the addition of trymethyltin to bithiophene, which has a phosphate ester group. This compound is coupled to a brominated thiophene bypyridine molecule to form 4-PT_3bpy. The phosphate ester is then hydrolyzed to form **2**, which is coordinated to $Ru(bpy)_2^{2+}$ to form **5**. The thiophene chain extends off the fourth position of 2,2′-bipyridine.

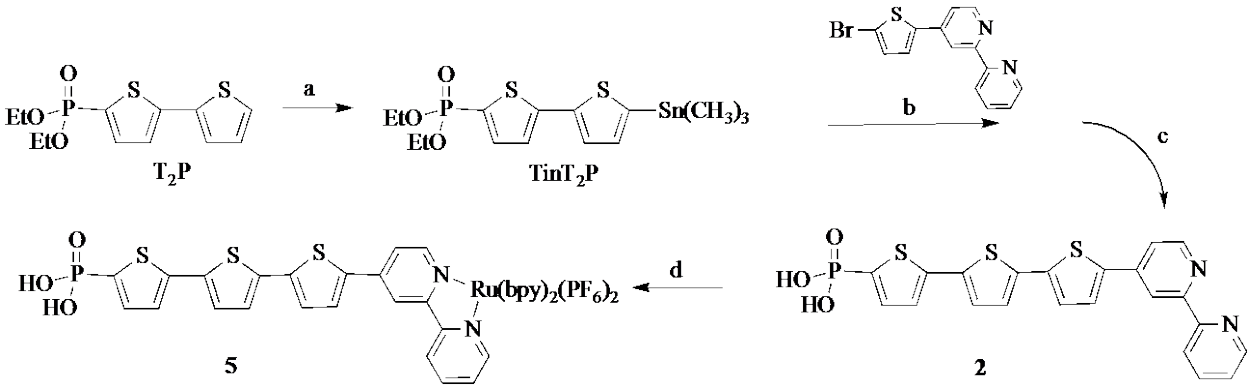

Scheme 1. Synthesis of **2** and **5.** Reagents (a) (1) LDA, -78 °C, 1hr; (2) Me_3SnCl, 24 hr; (b) $Pd(PPh_3)_4$, 120 °C, 120 hr; (c) TMSBr, neat rt, 12 hr; (d) $Ru(bpy)_2Cl_2$, 100 °C, 16hr, KPF_6.

4.2.1 Absorbance

The absorption spectra of the dithiophene (**1**), trithiophene (**2**), and terthiophene (**3**) have two major peaks (Figure 2a). The peak at 290 nm is common to all and originates from the bipyridine units. The second peak, due to the thiophene π-π* transition, is at longer wavelength, 358, 392, and 410 nm as the thiophene chain length goes from 2 to 3 to 4 subunits. This red shift implies the HOMO-LUMO gap is becoming smaller, which is expected due to greater conjugation. When $Ru(bpy)_2^{2+}$ is bound to the oligothiophenes, the bipyridine peak remains constant, the thiophene transition is red shifted (402 nm (4), 426 nm (5), and 440 nm (6)) and a MLCT peak from Ru-bpy appears (Figure 2b). The red shift shows that $Ru(bpy)_2^{2+}$ is interacting with the thiophene chain and changing the oligothiophene HOMO-LUMO gap. The MLCT band slightly red shifts, 456 to 464 to 475 nm, as the thiophene chain length goes from 2 to 3 to 4, respectively.

Upon addition of the oligothiophenes to CdSe nanoparticles, most absorption peaks remain unchanged, but some are red shifted. The bpy transitions for compounds **1-3** and **4-6**, remain at 270 and 285 nm, respectively. Although the oligothiophene π-π*

transitions for **1**-**3** are red shifted by 20 (**1**), 8 (**2**), and 12 (**3**) nm, they remain unchanged for **4**-**6**. There are, however, red shifts seen for the MLCT bands for **4**-**6**, as they shift by 4 (**4**), 13 (**5**), and 12 (**6**) nm. These red shifts mean that the CdSe nanoparticles are lowering the energies of these affected transitions. For the nanoparticles, the absorption starts at 554 nm and is blue shifted by 9 (**1**), 20 (**2**), and 35 (**3**) nm and thus shifts to higher energy as the thiophene chain length increases. This is in contrast to the thiophenes with $Ru(bpy)_2^{2+}$, where it blue shifts more for the shorter thiophenes than the longer ones, 26 (**4**), 19 (**5**), and 6 (**6**) nm. This interesting change of the CdSe band gap due to oligothiophene binding, could be caused by a decrease in the nanoparticle's valence band, an increase in the conduction band, or a combination of these.

a)

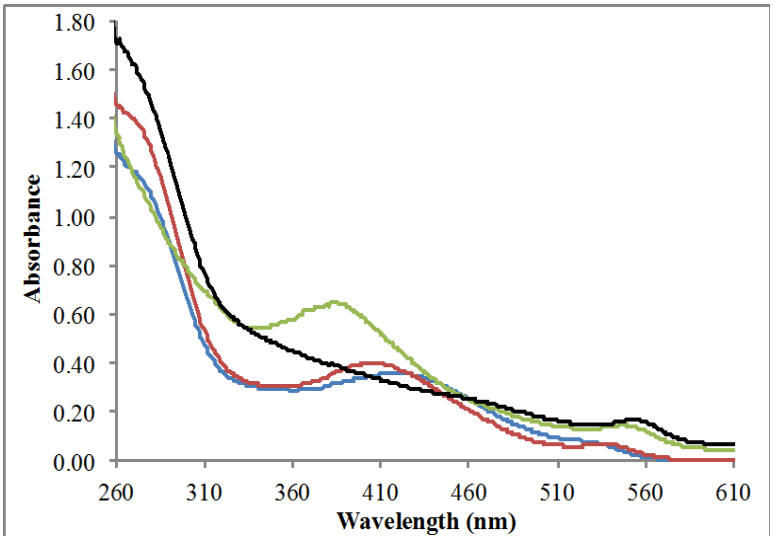

b)

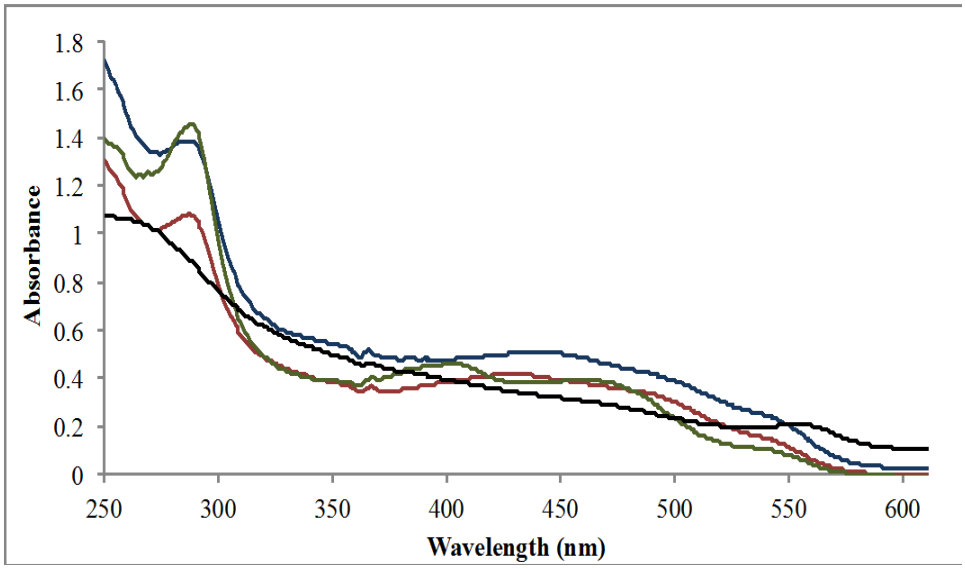

Figure 2. Absorbance spectra of a) **1** (–green), **2** (–red), and **3** (–blue) with CdSe nanoparticles, (CdSe nanoparticles (–black)); b) **4** (**–green**), **5** (**–red**), and **6** (**–blue**) with CdSe nanoparticles, (CdSe nanoparticles (–)).

4.2.2 Fluorescence

As the thiophene units increase from 2 to 4, the fluorescence wavelength maximum is red shifted and lies at 450, 488, and 506 nm for **1**, **2**, and **3**, respectively

(Figure 3). When $Ru(bpy)_2^{2+}$ is coordinated to the oligothiophenes, the fluorescence of the oligothiophenes and $Ru(bpy)_3^{2+}$ is mostly quenched. Compounds **4**, **5**, and **6** have a small broad fluorescence at around 428, 440, and 456 nm, respectively. One of the several ways fluorescence could be quenched would be for an electron from the $Ru(bpy)_3^{2+}$ to move into the hole created in the thiophene as a result of excitation, followed by the excited electron moving to the hole in the $Ru(bpy)_3^{2+}$.

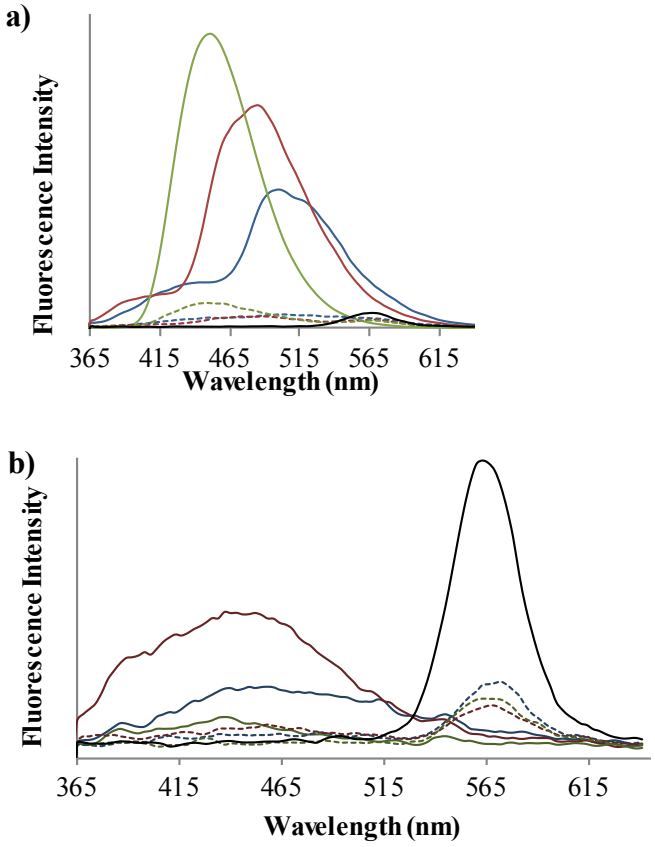

Figure 3. Fluorescence spectra of a) **1** (–), **2** (–), **3** (–), **1** with NPs (--), **2** with NPs (--), **3** with NPs (--) and b) **4** (–), **5** (–), **6** (–), **4** with NPs (--), **5** with NPs (--), **6** with NPs (--). CdSe NPs (–).

Combining the oligothiophenes with CdSe results in quenching of oligothiophene fluorescence (Figure 3). Quenching occurs with oligothiophenes without Ru (**1**, **2**, **3**) and those with Ru (**4**, **5**, **6**). Thus, the nanoparticles have facilitated a nonradiative decay

pathway for the oligothiophenes. This could be due to the creation of a new electron transfer or energy transfer pathway. Along with the fluorescence quenching of the oligothiophenes, the fluorescence of the CdSe nanoparticles was also quenched (Figure 3). As mentioned, a new electron and/or hole transfer pathway could potentially lead to quenching, but it could also be due to nanoparticle surface modification, which are known to influence CdSe fluorescence. Whatever the mechanism of fluorescence quenching, the results indicate there is communication between the thiophenes and nanoparticles.

Noting the CdSe nanoparticle's efficient quenching, we performed fluorescence quenching titrations with **1**, **2**, and **3** and calculated Stern-Volmer constants. The data were compared to equal volume additions of blank solvent and plotted using the Stern-Volmer relationship given by $I_f^0/I_f = k_q C_q$, where I_f^0 is the intensity of fluorescence in the absence of quencher, I_f is the fluorescence intensity with quencher, k_q is the quenching constant and C_q is the concentration of quencher. Since the $Ru(bpy)_2$ had already quenched the thiophene fluorescence, we did not perform these experiments for **4**-**6**. As Figure 4 shows, the fluorescence of the oligothiophenes is quickly quenched after a short lag phase. The Stern-Volmer constants for the steep part of the plots are K_s (M^{-1}) = 1.9 x 10^6 for **1**, 4.0 x 10^5 for **2**, and 3.1 x 10^5 for **3**. More than 95% of the fluorescence of **1** is quenched with 0.2 equivalent of CdSe. This quenching can be explained by each CdSe nanoparticle binding and quenching multiple oligothiophenes. These molecules being equipped with coordinating phosphate groups, means the quenching might be due to an electron transfer mechanism, however we can not rule out a fluorescence resonance energy transfer (FRET) mechanism.

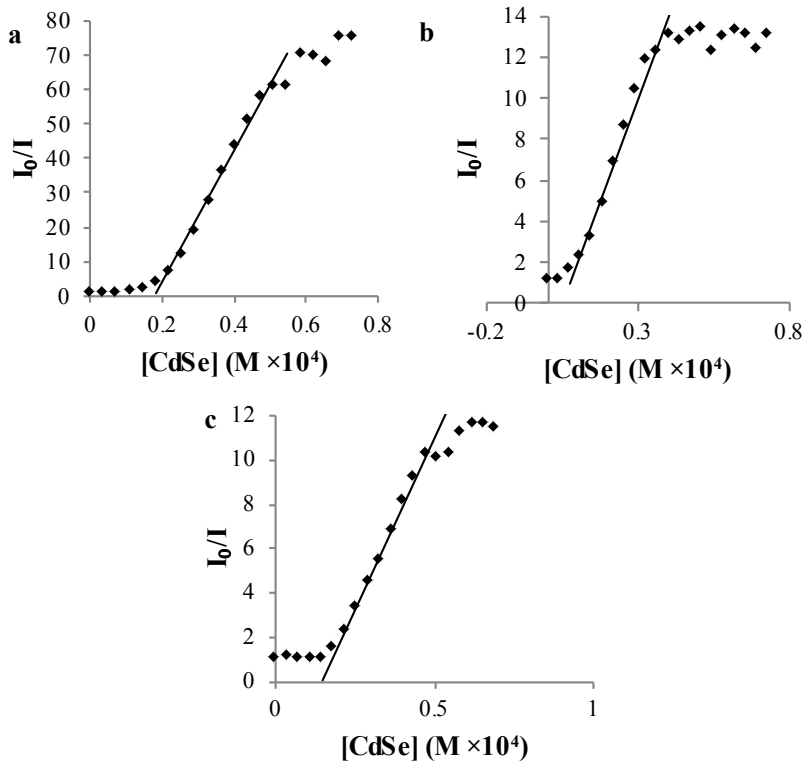

Figure 4. Stern-Volmer plots for **1** (a), **2** (b), and **3** (c). Stern-Volmer constants were calculated from the straight lines.

To gain a better understanding of the quenching mechanism, CdSe nanoparticles were added to bithiophenes that resembled **1** and **4**, but did not contain the phosphonic acid group (Figure 5). The fluorescence of these molecules was also quenched, however the Stern-Volmer constants were much smaller, K_s = 1.7 x 10^4 for T_2bpy and 3.1 x 10^4 for T_2bpyRu(bpy)$_2$. These values are similar to those constants calculated using the data in the lag phase part of the Stern-Volmer plots of **1**, **2**, and **3**. Since these molecules do not have nanoparticle binding groups, we attribute this quenching to FRET. The order of magnitude difference in Stern-Volmer constants, shows how the phosphonic acid binding group enhances fluorescence quenching and facilitates communication between the nanoparticles and oligothiophenes.

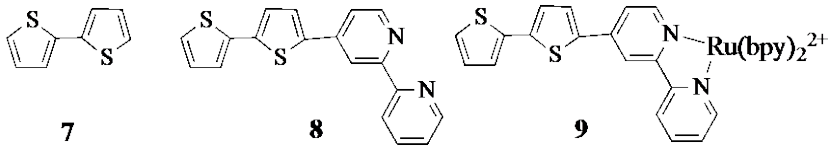

Figure 5. Bithiophenes without phosphoric acid groups (**7, 8,** and **9**) used with CdSe nanoparticles.

Further investigation of whether the CdSe was quenched was carried out with compound **4**. By using steady-state luminescence, it was found that **4** steadily quenches CdSe fluorescence with a $K_s = 2.1 \times 10^5$ M^{-1} (Figure 6). Due to spectral overlap, the quenching of CdSe by **1** could not be quantified. This efficient quenching could be due to electron transfer, FRET, or CdSe surface modifications, which create nonradiative decay pathways.

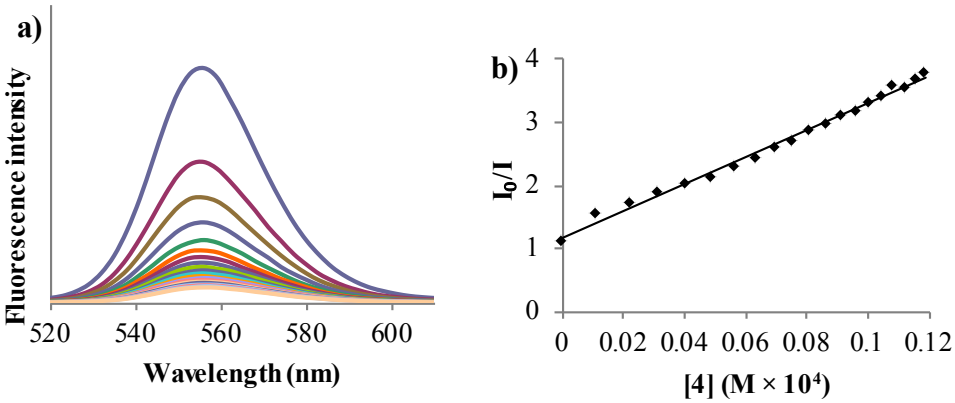

Figure 6. Fluorescence measurements of CdSe with increasing concentration of **4** (350 nm excitation). a) Shows fluorescence reductions as **4** is added. b) Stern-Volmer plot of fluorescence ratio versus concentration of **4**.

4.2.3 Time Correlated Single Photon Counting

Time correlated single photon counting (TCSPC) was used to measure the fluorescence lifetimes of the CdSe nanoparticles with **1** and **4**. We used a 25 fs pulsed laser with a 12 ns pulse interval to excite the fluorescence. The laser was gated on and off with an acousto-optic modulator (AOM), which created ~100 ns pulse trains (i.e. trains of

~8 pulses). The pulse train created by the AOM had a Gaussian envelope, so that pulses in the beginning/end of the train had a much smaller intensity than pulses in the middle. For fast optical lifetimes, the fluorescence decays could be seen between the pulses in the train; for slower optical lifetimes, the fluorescence would build up during a train and the decays could be measured following the last pulse in a train. The latter was the case for the control, CdSe nanoparticles in chloroform, for which a fluorescence lifetime of ~50 ns was measured (Figure 7).

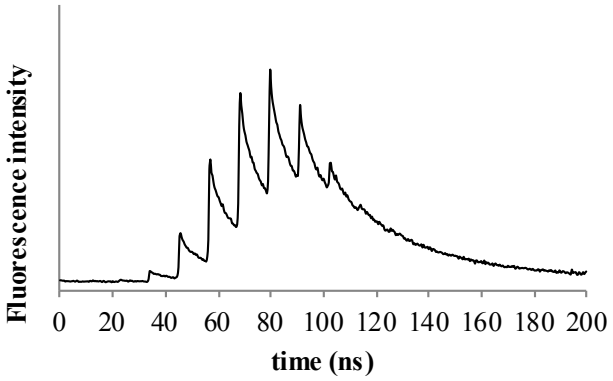

Figure 7. Fluorescence lifetime of CdSe nanoparticles in chloroform. Excitation wavelength was 400 nm, fluorescence wavelength was 557 nm.

Upon mixing the CdSe nanoparticles with **1** or **4** in a similar manner to the steady-state fluorescence experiments, the fluorescence lifetime CdSe nanoparticles were acquired (Figure 8). These data were taken at the same emission wavelength, 557 nm, and are plotted as a proportion of fluorescence remaining over time. The graphs shows a shortened fluorescent lifetime of CdSe nanoparticles which was previously so long we were unable to see the entire decay before the next pulse from the laser source. This significantly shortened lifetime suggests a fast electron transfer from oligothiophene to nanoparticle, which is on a competitive timescale with fluorescence. This is most likely due to a new electron/hole transfer pathway becoming available.

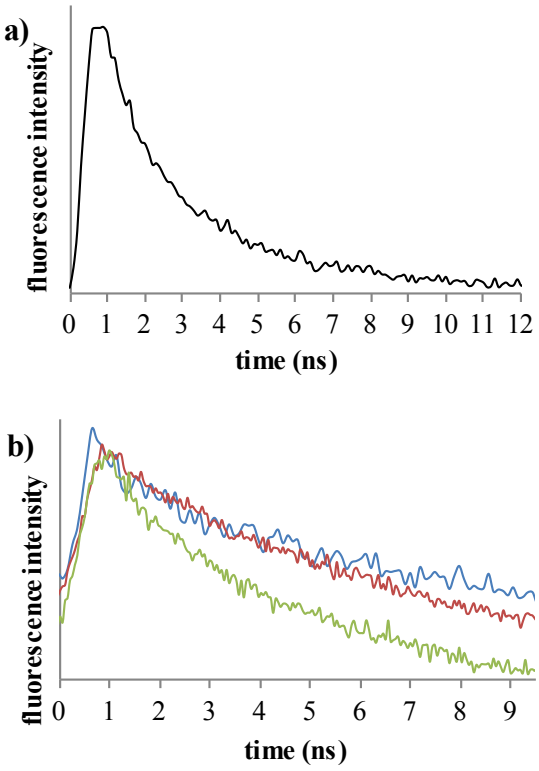

Figure 8. Fluorescence lifetimes of CdSe nanoparticles with **1** (a) and increasing concentrations of **4** (b) going from blue to red to green. Excitation wavelength was 400 nm and fluorescence wavelength was 557 nm.

The fluorescence lifetime of **1** was measured and is given in Figure 9. These data show that the fluorescence lifetime of the oligothiophene chain is on the order of a single nanosecond. Because the steady-state fluorescence measurements showed fluorescence quenching of **1** by CdSe nanoparticles, these data suggest that the excited electron transfer from oligothiophene to nanoparticle becomes competitive with fluorescence around the single nanosecond timescale. Fluorescent lifetimes of **4** were not measured because the fluorescence signal was too weak due to nearly complete quenching.

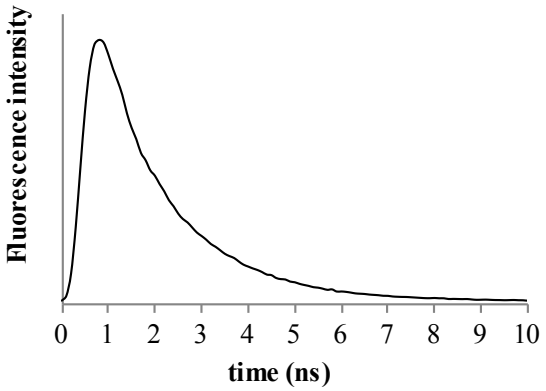

Figure 9. Fluorescence lifetime of **1**. Excitation wavelength was 400 nm, fluorescence wavelength was 444 nm.

4.3 Conclusion

New bifunctional oligothiophenes were prepared, which contained phosphonic acid groups for binding to CdSe nanoparticles and bpy units to bind to Ru. Along with four other oligothiophenes, these were bound to CdSe nanoparticles. The absorption spectra of the CdSe bound oligothiophenes only shift slightly. Steady-state fluorescence measurements showed that CdSe nanoparticles quenched oligothiophenes, those without and those with Ru. Stern-Volmer plots showed very efficient quenching and large constants. TCSPC measurements show a decreased fluorescence lifetime of the nanoparticle upon binding with an oligothiophene bound to Ru. An even stronger decrease in fluorescence lifetime is observed when Ru is not present. These experiments suggest electron transfer from oligothiophene to nanoparticle is on the order of single nanoseconds.

4.4 Experimental

All starting materials were used as purchased from commercial sources. Dry solvents were always used and obtained from activated alumina columns. Glassware for water-sensitive reactions was oven-dried at 100 °C. N_2 was used as the atmosphere in

air-sensitive reactions. Column chromatography was performed using silica gel. All NMR spectra were taken on a 500 MHz Varian NMR, and referenced to internal TMS. Absorbance measurements were taken on a Hewlett Packard 8453 spectrophotometer. Steady-state luminescence measurements were taken using a quartz cuvette in a Photon Technology International (PTI) Bryte Box fluorometer. Excitation wavelength was set at 350 nm.

4.4.1 Organic syntheses

Diethyl 5'-trimethyltin-2,2'-bithien-5-ylphosphonate (TnT_2P)

Lithium diisopropyl amide (1.2 mL, 1.4 M) was added to T_2P (0.420 g 1.39 mmol) dissolved in 6.0 mL of THF at -78 °C and stirred for 1 hour. While at -78 °C, $(CH_3)_3SnCl$ (0.320 g, 1.61 mmol) dissolved in 5.0 mL was dripped in to the solution and the solution was stirred for 4 hours, allowed to warm to room temperature, and stirred for 24 hours. The solution was then evaporated to an oil, which oil was dissolved in 10 mL CH_2Cl_2 and received 10 mL of saturated NH_4Cl. The CH_2Cl_2 solution was separated, washed with water and dried with sodium sulfate, filtered, and evaporated to an oil (0.495 g, 76.4 % yield). ^1H NMR ($CDCl_3$, 500 MHz) δ: 7.54 (dd, 1H, J = 2.5 Hz), 7.34 (d, 1H, J = 2.5 Hz), 7.18 (t, 1H, J = 3.5 Hz), 7.11 (d, 1H, J = 3.5 Hz), 4.13 (m, 4H), 1.348 (m, 6H), 0.39 (m, 9H). HRMS (ESI-TOF) *m/z* calcd for $C_{15}H_{24}O_3PS_2Sn$ $(M + H)^+$ 466.98; found 466.9910.

Diethyl 5''-(2,2'-bipyridin-4-yl)-2,2'-5',2''-terthien-5-ylphosphonate (4-PT_3bpy)

4-BrTbpy (0.1002 g, 0.3171 mmol), SnT_2P (0.1891 g), and $Pd(PPH_3)_4$ (0.0370 g) were dissolved in 75 mL toluene and refluxed at 115 °C for 5 days. After cooling to room temperature, 200 mL of hexane was added. The solution was evaporated to 20 mL,

hexane added, and precipitate collected. The solution was let stand and another crop of precipitate was collected. The product weighted 0.1017 g (60 % yield). ^{1}H NMR ($CDCl_3$, 500 MHz) δ: 8.75 (d, 1H, J = 5 Hz), 8.68 (d, 1H, J = 2.5 Hz), 8.64 (d, 1H, J = 1.5 Hz), 8.45 (d, 1H, J = 8.0 Hz), 7.86 (td, 1H, J = 5.0, 2.5 Hz), 7.60 (d, 1H, J = 3.5 Hz), 7.58 (dd, 1H, J = 5.0 Hz), 7.50 (dd, 1H, J = 5.5, 2.0 Hz), 7.36 (td, 1H, J = 5.5, 2.0 Hz), 7.25 (d, 1H), 7.26 (d, 1H, J = 4 Hz), 7.24 (dd, 1H, J = 3.0 Hz), 7.21 (d, 1H, J = 3.0 Hz), 4.20 (m, 4H), 1.38 (t, 6H, J = 7.0 Hz). HRMS (ESI-TOF) *m/z* calcd for $C_{26}H_{24}N_2O_3PS_3$ $(M + H)^+$ 539.06; found 539.0715.

5″-(2,2′-bipyridin-4-yl)-2,2′-5′,2″-terthien-5-ylphosphonic acid (4-APT$_3$bpy)

TMSBr (0.5 mL, 3.75 mmol) and 4-PT$_3$bpy (0.0520 g, 0.0967 mmol) were added to a dry, N_2 purged flask and the reaction was stirred for 12 hours. Two mL of water were added to the slurry while stirring, the precipitate was filtered, washed with water, dried, washed with diethyl ether, and air-dried. The dark red-orange product weighed 0.0442 g (95 % yield). ^{1}H NMR (DMSO, 500 MHz) δ: 8.76 (d, 1H, J = 2.0 Hz), 8.71 (d, 1H, J = 4.5 Hz), 8.61 (s, 1H), 8.47 (d, 1H, J = 8.0 Hz), 8.03 (t, 1H, J = 8.0 Hz), 8.77 (d, 1H, J = 2.0 Hz), 7.82 (d, 1H, J = 2.5 Hz), 7.53 (m, 2H), 7.49 (d, 1H, J = 2.5 Hz), 7.45 (d, 1H, J = 2.5 Hz), 7.39 (d, 1H), 7.37 (d, 1H). HRMS (ESI-TOF) *m/z* calcd for $C_{22}H_{15}N_2O_3PS_3$ $(M + H)^+$ 483.00; found 483.0126.

[5′′-(2,2′-bipyridin-4-yl)-2,2′-5′,2′′-terthien-5-ylphosphonic acid]bis(bipyridyl)ruthenium(II) hexafluorophosphate (4-APT$_3$bpyRu)

4-APT$_3$bpy (16.2 mg, 0.0377 mmol), $Ru(bpy)_2Cl_2$ (16.1 mg, 0.0329 mmol) and NaOH (2.0 mg) were dissolved in 10 mL H_2O and refluxed for 16 hr. The solution after cooling was filtered through celite, which celite was washed with basic water until colorless. The

aqueous solution was acidified with 6.5 mL 1.0 M HCl and an aquesous solution of KPF_6 (0.0642 g KPF_6/ 1 mL H_2O) was added to it. The dark red precipitate that formed was filtered, dried and weighed (27.6 mg, 71 % yield). ^{1}H NMR (DMSO, 500 MHz) δ: 9.14 (d, 1H, J = 7.5 Hz), 9.07 (s, 1H), 8.85 (s, 4H), 8.20-8.18 (m, 6H), 7.89 (d, 1H, J = 2.5 Hz), 7.74 (s, 4H), 7.68 (d, 1H), 7.63 (m, 2H), 7.55 (m, 5H), 7.48 (s, 1H), 7.46 (s, 1H), 7.40 (m, 2H). ^{31}P NMR (DMSO, 121 MHz) δ: 9.1 (s). HRMS (ESI-TOF) *m/z* calcd for $C_{42}H_{31}N_6O_3PRuS_3^{2+}$ $(M)^{2+}$ 448.02; found 448.0269.

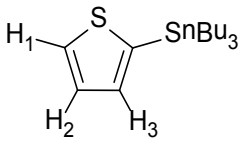

2-tributylstannylthiophene (TinT)

Thiophene (13.5 mL, 169 mmol) was added to a dry, N_2 purged Schlenk flask with 150 mL THF and cooled to -78°C. *n*-BuLi (100 mL, 160 mmol) was added dropwise and the solution was allowed to react for 1 hr under continued cooling. Tri-n-butyltin chloride (43.4 mL, 160 mmol) was added and the solution was allowed to warm to room temperature overnight. The THF was evaporated under vacuum and 75 mL toluene were added. The solution was left to stir for 45 min after which the insoluble salts were filtered out through celite. The toluene was evaporated under vacuum and the resulting pale yellow liquid was chromatographed using hexanes as eluent. TinT (34.73 g, 93.1 mmol, 58% yield) was collected and is a clear colorless liquid. δ 7.67 (H_1, dd, 1H, J = 1, 5 Hz), δ 7.29 (H_2, dd, 1H, J = 3, 4.5 Hz), δ 7.22 (H_3, dd, 1H, J = 1, 3.3 Hz), δ 1.60 ($SnCH_2CH_2CH_2CH_3$, m, 6H), δ 1.36 ($SnCH_2CH_2CH_2CH_3$, m, 6H), δ 1.13 ($SnCH_2CH_2CH_2CH_3$, m, 6H), δ 0.92 ($SnCH_2CH_2CH_2CH_3$, t, 9H, J = 7 Hz).

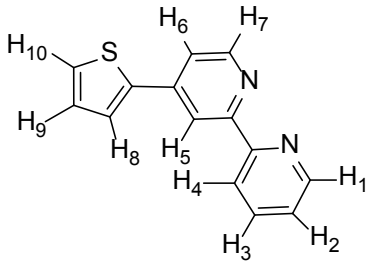

2-(2,2´-bipyridin-4-yl)-thiophene (4-Tbpy)

4-Brbpy (2.32 g, 9.87 mmol), TinT (3.76 g, 10.0 mmol) and $Pd(PPh_3)_4$ (0.93 g, 0.80 mmol, 8.2 mol%) were dissolved in 250 mL of dry toluene under N_2. The solution was brought to reflux for 96 hr. The toluene was then evaporated and the remains were partitioned between 2M NaOH and CH_2Cl_2. The organics were separated off, filtered through celite and the solvent was removed. The remains were subjected to column chromatography using ethyl acetate as eluent followed by 25% methanol in ethyl acetate once the impurities had been removed. 4-Tbpy (1.69 g, 7.11 mmol, 72%) was collected as a yellow brown solid and was without impurities as noted by NMR. ^{1}H NMR ($CDCl_3$, 500 MHz): δ 8.73 (H_1, d, 1H), δ 8.66 (H_7, d, 1H), δ 8.64 (H_5, d, 1H), δ 8.44 (H_4, d, 1H), δ 7.84 (H_3, td, 1H), δ 7.68 (H_{10}, d, 1H), δ 7.51 (H_8, dd, 1H), δ 7.43 (H_6, d, 1H), δ 7.30 (H_2, m, 1H), δ 7.16 (H_9, t, 1H). ESI-TOF $(M+H)^+$ mass: 239.0638.

2-bromo-5-(2,2´-bipyridin-4-yl)-thiophene (4-BrTbpy)

4-Tbpy (1.64 g, 6.88 mmol) and NBS (2.58 g, 8.88 mmol) were dissolved in 300 mL of 1:1 $CHCl_3$:AcOH and heated to 60 °C for 30 min. 50 mL of H_2O were added and the layers were separated. The aqueous phase was extracted with 2 x 50 mL of chloroform. The combined organics were neutralized with $K_2CO_{3(aq)}$ and then dried over $MgSO_4$. The solution was filtered through celite and the solvent was evaporated. 4-BrTbpy (1.32 g, 4.16 mmol, 61%) was collected and is clean to NMR. ^{1}H NMR ($CDCl_3$,

500 MHz): δ 8.71 (H_1, d, 1H, J = 4 Hz), δ 8.66 (H_7, d, 1H, J = 5 Hz), δ 8.56 (H_5, d, 1H, J = 1.5 Hz), δ 8.43 (H_4, d, 1H, J = 8.5 Hz), δ 7.84 (H_3, td, 1H, J = 1.5, 8 Hz), δ 7.40 (H_6, d, 1H, J = 3.5 Hz), δ 7.39 (H_8, d, 1H, J = 2 Hz), δ 7.34 (H_2, m, 1H), δ 7.11 (H_9, d, 1H, J = 4 Hz). ^{13}C NMR ($CDCl_3$, 500 MHz): δ 156.82, 155.55, 149.792, 149.14, 142.79, 141.60, 137.05, 131.27, 125.88, 124.04, 121.30, 119.42, 116.83, 114.42. ESI-TOF $(M+H)^+$ mass: 316.9743.

[5′-(2,2′-bipyridin-4-yl)-2,2′-5′,2″-bithiophene]bis(bipyridyl)ruthenium(II) hexafluorophosphate (4-T_2bpyRu)

4-T_2bpy (0.0060 g, 0.019 mmol) and $Ru(bpy)_2Cl_2$ (0.0063 g, 0.015 mmol) were dissolved in 1.5 mL of 95% ethanol and refluxed for 24 hr. KPF_6 (0.040 g) in 0.5 mL H_2O was added and an orange solid precipitated as the solution cooled. The solid was filtered and collected and left to dry under vacuum overnight. Orange-red 4-T_2bpyRu (0.0096 g, 0.0094 mmol, 63% yield) was clean to ^{1}H NMR. ^{1}H NMR (DMSO, 500 MHz): δ 8.90-8.81 (m, 6H), δ 8.46 (d, 1H), δ 8.28 (t, 1H), δ 8.19-8.15 (m, 4H), 7.95 (d, 1H), δ 7.86 (d, 1H), δ 7.76 (d, 2H), δ 7.73 (d, 1H), δ 7.65-7.52 (m, 8H), δ 7.39 (d, 1H), δ 7.35 (d, 1H), δ 7.15 (t, 1H).

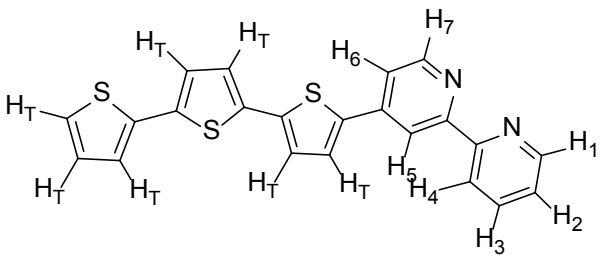

5″-(2,2′-bipyridin-4-yl)-2,2′-5′,2″-terthiophene (4-T_3bpy)

Into 50 mL dry toluene were dissolved 4-BrTbpy (0.1218 g, 0.38 mmol), $TinT_2$ (0.2142 g, 0.47 mmol) and $Pd(PPh_3)_4$ (0.08 g, 0.07 mmol). The solution was heated to reflux for 72 hr. The reaction was cooled, filtered through celite and the solvent was removed. The toluene was replaced with hexanes and the precipitate was filtered and collected. This solid was recrystallized in DMSO and then in THF/hexanes. 4-T_3bpy (0.158 g, 0.39 mmol, 100%) was a dark red solid. ^{1}H NMR (DMSO, 500 MHz): δ 9.05 (H_1, d, 1H), δ 8.72 (H_7, d, 1H), δ 8.45 (H_4, d, 1H), 8.41 (H_5, d, 1H), δ 8.23 (H_3, dd, 1H), 7.98 (H_6, td, 1H), δ 7.76 (H_T, d, 1H), δ 7.58-7.33 ($H_{2,T,T,T,T,}$ m, 5H), δ 7.13 (H_T, t, 1H). ESI-TOF $(M+H)^+$ mass: 402.0392.

4.4.2 Optical measurements

The CdSe nanoparticles were made with trioctylphosphinoxide (TOPO) ligands on their surface and were soluble in nonpolar solvents.[40] Approximately three mL of CdSe mixture as prepared were dissolved in 15 mL of methanol to dissolve the extra ligand. The suspension was centrifuged and the mother liquor was discarded. The solid was dissolved in 10 mL $CHCl_3$ and any solid remained it was removed by centrifugation. The solution was diluted until an absorption <1 was found by UV-vis and a concentration could be determined. UV-vis was used to determine size and concentration of the nanoparticles. CdSe absorption was found to be 550 nm, which corresponds to an average size of 3.0 nm and a molar absorptivity of 1.05×10^5 cm^{-1} M^{-1}. A degassed chloroform solution of CdSe nanoparticles at a concentration of 2.94 μM was prepared for binding to **1** and **4**, which were prepared as degassed butanol solutions.

All solutions of oligothiophenes and oligothiophene-ruthenium complexes were made by sonicating approximately 50 mg of solid in butanol for 10 min and centrifuged.

The saturated solution was retained and the remaining solid was left in the centrifuge tube for future solutions. The solution was diluted until an absorption <1 was found by UV-vis so a concentration could be determined. All solutions were placed in dry Schlenk flasks equipped with rubber septa and the solutions were degassed by bubbling N_2 through a needle into the solution with the stop cock open. After 15 min the stop cock was closed and the needle removed.

All fluorescence measurements were taken using a step size of 3 nm, using a single integration and no averaging. In quenching experiments, 1.5 mL of the species being quenched was added to an N_2 purged cuvette via syringe, followed by removal of 1 mL of N_2 to maintain pressure. The fluorescence was measured, followed by additions of 75 μL of quenching solution via syringe with readings taken after each addition. For Stern-Volmer plots the above procedure was followed by an identical blank experiment using 1.5 mL of the species to be quenched with 75 μL additions of degassed solvent identical to that used to dissolve the quenching species.

4.4.3 CdSe Experimental for UV-vis and Fluorescence

Ruthenium compounds were diluted in 50/50 butanol/acetonitrile and non-ruthenium compounds in a 50/50 butanol/DMSO mixture. The CH_3CN and DMSO were added due to low solubility in butanol and to increase solubility of the CdSe nanoparticles. Solutions of the CdSe nanoparticles were made in chloroform. Solutions ≤ 0.4 absorbance in a 1 cm quartz cuvette were used for fluorescence. Quinine sulfate in 1.0 N H_2SO_4 was used as a standard for fluorescent quenching.[41] For fluorescence, 350 nm light was used for excitation and a step size of 3 nm from 350 to 650 nm. The absorbance of the quinine sulfate was matched to that of compounds at 350 nm.

4.4.4 Stern-Volmer measurements

Each compound studied was dissolved with a 50/50 mixture of either butanol/acetonitrile or butanol/DMSO to an absorbance of 0.4. The solutions were degassed with nitrogen for 10 minutes. Fluorescent intensity measurements were taken on a PTI spectrofluorometer. An initial amount of 1.5 mL (50+ equivalents) of each solution was added to a 1 cm quartz cuvette and the intensity was measured. Aliquots of 76 uL of CdSe nanoparticles dissolved in $CHCl_3$ were used as quencher. A total of 20 aliquots or 1.52 mL of CdSe solution was added to give an end equivalent ratio of CdSe nanoparticles to compound of 1 to 3-5. A blank trial was also run with $CHCl_3$ using the same amounts as described above. The ratio of fluorescent intensity of the blank to the quenched solution (I_0/I) was plotted against the concentration of the CdSe nanoparticles as described by the Stern-Volmer equation $\frac{I_0}{I} = k_q C_q$. The quenching constant k_q is then calculated by using the slope of a line fit to the data.

4.4.5 Time Correlated Single Photon Counting

TCSPC measurements were taken in a quartz fluorescence cuvette using solutions identical to those used in the fluorescence measurements except that they were not degassed. Excitation pulses are from a Ti:sapphire femtosecond oscillator which produces 25 fs, 4 nJ pulses centered at 800 nm, at a repetition rate of 80 MHz. These were frequency doubled to 400 nm in a Type 1 BBO crystal. The pulse train was chopped by an acousto-optic modulator (AOM) to give packets of ~8 pulses per envelope. Fluorescence was focused to a quarter meter monochrometer for wavelength selectivity and detected with a photomultiplier tube. Timing was done with an Edinburgh Instruments T900 TCSPC card, which created a histogram of single photon fluorescence

events based on the difference in time between a reference "start" pulse (from a detector internal to the laser cavity, which also triggered the AOM) and the photomultiplier tube's "stop" pulse.

References

1. Nelson, J. Organic photovoltaic films, *Curr. Opin. Solid. St. M.* **2002**, *6*, 87–95.

2. Bundgaard, E.; Krebs, F. C. Low band gap polymers for organic photovotaics, *Sol. Energ. Mat. Sol. C.* **2007**, *91,* 954–985.

3. Brabec, C. J.; Sariciftci, N. S.; Hummelen, J. C. Plastic solar cells, *Adv. Funct. Mater.* **2001**, *11*, 15–26.

4. Liang, Y.; Wu, Y.; Feng, D.; Tsai, S.; Son, H.; Li, G.; Yu, L. Development of new semiconducting polymers for high performance solar cells, *J. Am. Chem. Soc.* **2009**, *131*, 56–57.

5. Wienk, M. M.; Turbiez, M.; Gilot, J.; Janssen, R. A. J. Narrow-bandgap diketo-pyrrolo-pyrrole polymer solar cells: the effect of processing on the performance, *Adv. Mater.* **2008**, *20*, 2556–2560.

6. Kamat, P. C.; Quantum dot solar cells, semiconductor nanocrystals as light harvesters, *J. Phys. Chem. C.* **2008**, *112*, 18737–18753.

7. Mora-Sero, I.; Gimenez, S.; Fabregat-Santiago, F.; Gomez, R.; Shen, Q.; Toyoda, T.; Bisquert, J. Recombination in quantum dot sensitized solar cells, *Acc. Chem. Res.* **2009**, *42*, 1848–1857.

8. Meyer, G. J. Molecular approaches to solar energy conversion with coordination compounds anchored to semiconductor surfaces *Inorg. Chem.* **2005**, *44*, 6851–6864.
9. Grätzel, M. Solar energy conversion by dye-sensitized photovoltaic cells, *Inorg. Chem.* **2005**, *44*, 6841–6851.

10. Bergmann, R.B. Crystalline Si thin-film solar cells: a review. *Appl. Phys. A: Mater. Sci. Process.* **1999**, *69*, 187-194.

11. Antoun, T.; Brayner, R.; Al terary, S.; Fiévet, F.; Chehimi, M.; Yassar, A. Facile synthesis of oligothiophene-capped CdS nanoparticles, *Eur. J. Inorg. Chem.* **2007**, *9*, 1275–1284.

12. Liang, Y.,; Peng, B.; Liang, J.; Tao, Z.; Chem, J. Triphenylamine-based dyes bearing functionalized 3,4-propylenedioxythiophene linkers with enhanced performance for dye-sensitized solar cells, *Org. Lett.* **2010**, *12*, 1204–1207.

13. Yang, H.; Yen, Y.; Hsu, Y.; Chou, H.; Lin, J.; Organic dyes incorporating the dithieno[3,2-*b*:2′,3′ -*d*]thiophene moiety for efficient dye-sensitized solar cells, *Org. Lett.* **2010**, *12*, 16–19.

14. Choi, H.; Baik, C.; Kang, S.; Ko, J.; Kang, M.; Nazeeruddin, M. K.; Grätzel, M.; Highly efficient and thermally stable organic sensitizers for solvent-free dye-sensitized solar cells, *Angew. Chem. Int. Ed.* **2008**, *47*, 327–330.

15. Hara, K.; Kurashige, M.; Dan-oh, Y.; Kasada, C.; Shinpo, A.; Suga, S.; Sayama, K.; Arakawa, H.; Design of new coumarin dyes having thiophene moieties for highly efficient organic-dye-sensitized solar cells, *New J. Chem.* **2003**, *27*, 783–785.

16. Ic, Y.; Hirose, T.; Aso, Y. Synthesis, properties, and FET performance of rectangular oligothiophene, *J. Mater. Chem.* **2009**, *19*, 8169–8175.

17. Umemoto, Y.; Le, Y.; Saeki, A.; Seki, S.; Tagawa, S.; Aso, Y. Electronegative oligothiophenes fully annelated with hexafluorocyclopentene: synthesis, properties, and intrinsic electron mobility. *Org. Lett.* **2008**, *10*, 1095–1098.

18. Le, Y.; Umemoto, Y.; Okabe, M.; Kusunoki, T.; Nakayama, K.; Pu, Y.; Kido, J.; Tada, H.; Aso, Y. Electronegative olighiophenes based on difluorodioxocyclopentene-annelated thiophenes: synthesis, properties, and n-type FET performances *Org. Lett.* **2008**, *10* (5), 833–836.

19. Otsubo, T.; Aso, Y.; Takimiya, K. Functional oligothiophenes as advanced molecular electronic materials, *J. Mater. Chem.* **2002**, *12*, 2565–2575.

20. Mishra, A.; Ma, C.; Bauerle, P. Functional oligothiophenes: Molecular design for multidimensional nanoarchitectures and their applications, *Chem. Rev.* **2009**, *109*, 1141–1276.

21. Luo, J.; Qu, H.; Yin, J.; Zhang, X.; Huang, K.; Chi, C. π-Conjugated oligothiophene-anthracene co-oligomers: synthesis, physical properties, and self-assembly, *J. Mater. Chem.* **2009**, *19*, 8202–8211.

22. Sauvage, F.; Fischer, M., K. R.; Mishra, A.; Zakeeruddin, S. M.; Nazeeruddin, M. K.; Bäurle, Peter; Grätzel, Michael; A dendritic oligothiophene ruthenium sensitizer for stable dye-sensitized solar cells, *Chemsuschem* **2009**, *2*, 761–768.

23. Gao, F.; Wang, Y.; Zhang, J.; Shi, D.; Wang, M.; Humphry-Baker, R.; Wang, P.; Zakeeruddin, S. M; Grätzel, M.; A new heteroleptic ruthenium sensitizer enhances the absorptivity of mesoporous titania film for a high efficiency dye-sensitized solar cell, *Chem. Commun*. **2008**, 2635–2637.

24. Gao, F.; Wang, Y.; Shi, D.; Zhang, J.; Wang, M.; Jing, X.; Humphry-Baker, R.; Wang, P.; Zakeeruddin, S. M.; Grätzel, M.; Enhance the optical absorptivity of nanocrystalline TiO_2 film with high molar extinction coefficient ruthenium sensitizers for high performance dye-sensitized solar cells, *J. Am. Chem. Soc*. **2008**, *130*, 10720–10728.

25. Chen, C.; Wu, S.; Wu, C.; Chen, J.; Ho, K.; A ruthenium complex with superhigh light-harvesting capacity for dye-sensitized solar cells, *Angew. Chem.* **2006**, *118*, 5954–5957.

26. Chen, C.; Wu, S.; Li, J.; Wu, C.; Chen, J.; Ho, K.; A new route to enhance the light-harvesting capability of ruthenium complexes for dye-sensitized solar cells, *Adv. Mater*. **2007**, *19*, 3888–3891.

27. Houarner-Rassin, C.; Chaignon, F.; She, C.; Stockwell, D.; Blart, E.; Buvat, P.; Lian, T.; Odobel, F. Synthesis and photoelectrochemical properties of ruthenium bisterpyridine sensitizers functionalized with a thienyl phosphonic acid moiety, *J. Photochem Photobio A* **2007**, *192*, 56–65.

28. Hagberg, D. P.; Edvinsson, T.; Marinado, T.; Boschloo, G.; Hagfeldt, A.; Sun, L. A novel organic chromophore for dye-sensitized nanostructured solar cells. *Chem. Commun*. **2006**, *21*, 2245–2247.

29. Zotti, G.; Vercelli, B.; Berlin, A.; Pasini, M.; Nelson, T. L.; McCullough, R. D.; Virgili, T. Self-assembled structures of semiconductor nanocrystals and polymers for photovoltaics. 2 Multilayers of CdSe nanocrystals and oligo(poly)thiophene-based

molecules. Optical, electrochemical, photoelectrochemical, and photoconductive properties, *Chem. Mater.* **2010**, *22*, 1521-1532.

30. Fritzinger, B.; Capek, R. K.; Lambert, K.; Martins, J.; Hens, Z. Utilizing self-exchange to address the binding of carboxylic acid ligands to CdSe quantum dots, *J. Am. Chem. Soc.* **2010**, *132*, 10195–10201.

31. Edder, C.; Fréchet, J. M. J. Synthesis of bridged oligothiophenes: toward a new class of thiophene-based electroactive surfactants, *Org. Lett.* **2003**, *5*, 1879-1882.

32. Milliron, D. J.; Alivisatos, A. P.; Pitois, C. E.; Fréchet, J. M. J. Electroactive surfactant designed to mediate electron transfer between CdSe nanocrystals and organic semiconductors, *Adv. Mater.* **2003**, *15*, 58–61.

33. O'Connor, C.; Roydhouse, M.; Przybyl, A.; Wall, M.; Southern, J. Facile Synthesis of 3-nitro-2-substituted thiophenes, *J. Org. Chem.* **2010**, *75*, 2534–2538.

34. Chen, R.; Yang, X.; Tian, H.; Wang, X.; Hagfeldt, A.; Sun, L. Effect of tetrahydroquinoline dyes structure on the performance of organic dye-sensitized solar cells, *Chem. Mater.* **2007**, *19*, 4007–4015.

35. Sih, B. C.; Wolf, M. O. CdSe nanorods functionalized with thiol-ancchored oligothiophenes, *J. Phys. Chem. C* **2007**, *111*, 17184-17192.

36. Britt, J.; Ferekides, C. Thin-film CdS/CdTe solar cell with 15.8% efficiency, *Appl. Phys. Lett.*, **1993**, *62*, 2851-2852.

37. Bang, J. H.; Kamat, P. V. Quantum dot sensitized solar cells: A tale of two semiconductor nanocrystals: CdSe and CdTe, *ACS Nano*, **2009**, *3*, 1467-1476.

38. Barea, E. M.; Shalom, M.; Gimenez, S.; Hod, I.; Mora-Sero, I.; Zaban, A.; Bisquert, J. Design of injection and recombination in quantum dot sensitized solar cells, *J. Am. Chem. Soc.* **2010**, *132*, 6834-6839.

39. Bair, J. S.; Harrison, R. G. Synthesis and optical properties of bifunctional thiophene molecules coordinated to ruthenium, *J. Org. Chem.* **2007**, *72*, 6653–6661.

40. Harrison, R. G.; Washburn, A. L.; Pickett, A. T.; Call, D. M. Assembly of CdSe Nanoparticles into Microspheres by a Liquid Droplet Emulsion Process. *J. Mater. Chem.* **2008**, *18*, 3718–3722.

41. Demas, J. N.; Crosby, G. A. The measurement of photoluminescence quantum yields. A review. *J. Phys. Chem.* **1971**, *75*, 991–1024.

APPENDIX

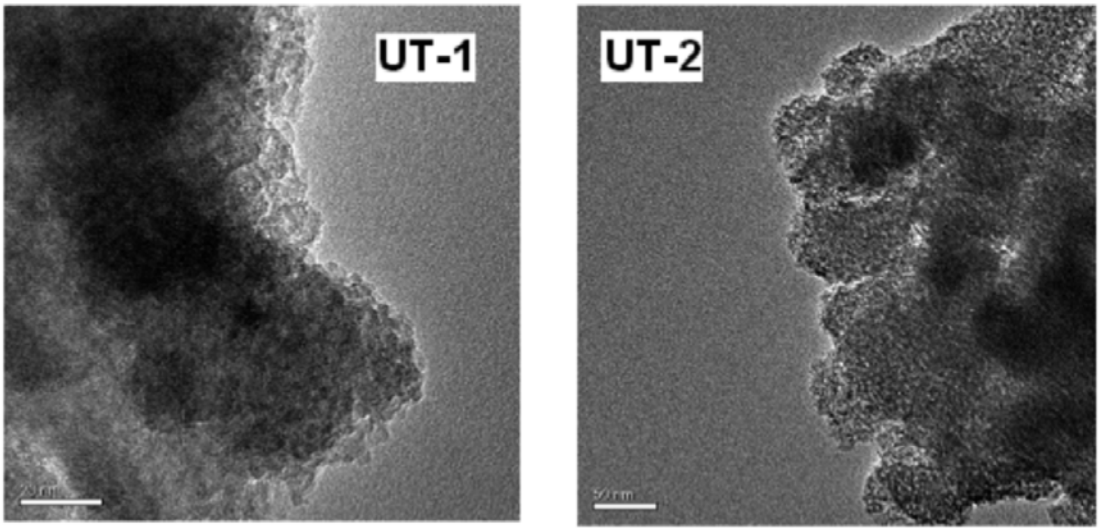

Figure 1. TEM images of the Fe:Al:Cu (UT-1) and Fe:Al:Cu:K (UT-2) FHYD samples.[1]

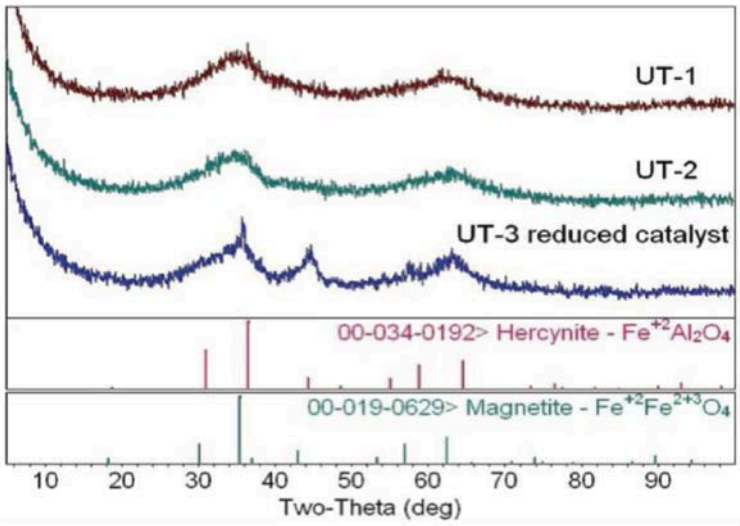

Figure 2. XRD pattern of as-prepared Fe:Al:Cu FHYD (UT-1), K impregnated Fe:Al:Cu:K (UT-2), and reduced Fe:Al:Cu:K FHYD (UT-3−0.3K).[1]

TEM and XRD work done in collaboration with Eyring group at the Univeristy of Utah about ferrihydrite nanoparticles for use as a catalyst in the Fischer-Tropsch synthesis.

[1] Bali, S.; Bali, G.; Huggins, F. E.; Seehra, M. S.; Singh, V.; Hancock, J. M.; Harrison, R. G.; Huffman, G. P.; Pugmire, R. J.; Ernst, R. D.; Eyring, E. M. Synthetic Doped Amorphous Ferrihydrite for the Fischer−Tropsch Synthesis of Alternative Fuels. *Ind. Eng. Chem. Res.* **2012**, 51, 4515−4522.

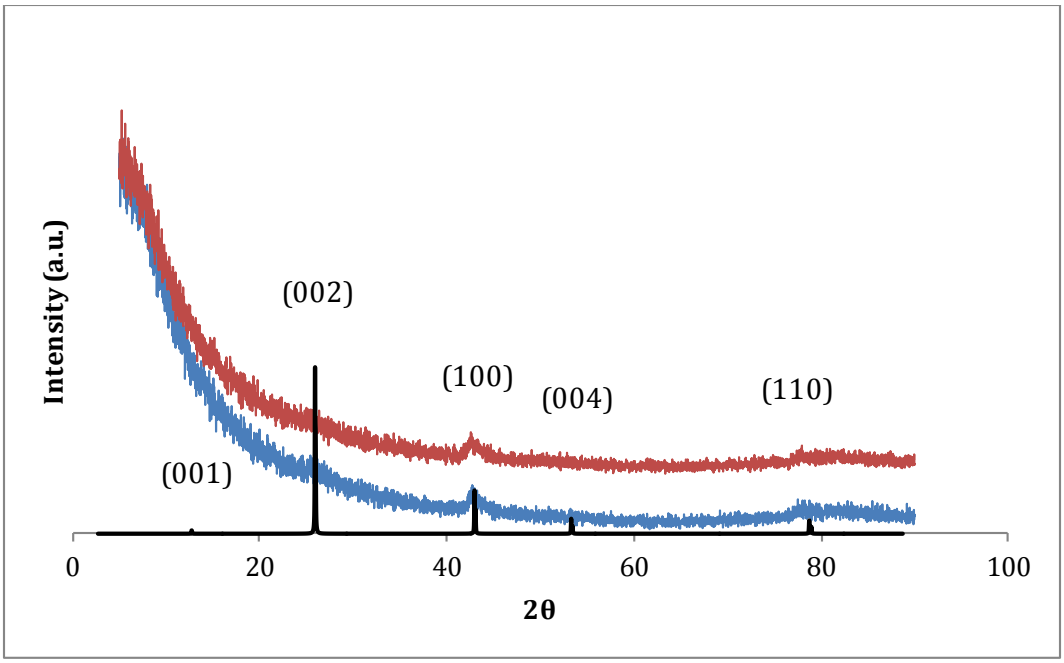

Figure 3. XRD graph of carbon coated carbon nanotubes (red) and carbon nanotubes (blue) showing similar structures to that of the reference carbon nanotubes (black).[2]

XRD analysis done in collaboration with the Linford group at BYU on carbon nanotubes and carbon coated carbon nanotubes on microfabricated thin layer chromatography plates grown from iron nanoparticles $Si/SiO_2/Al_2O_3/Fe(NP)/CNT$.

[2] Jensen, D. S.; Kanyal, S. S.; Engelhard, M.; Hancock, J. M.; Shutthanandan, V.; Zhu, Z.; Vanfleet, R.; Linford, M. R. Multi-Instrument Characterization of the Surfaces and Materials in Microfabricated, Carbon Nanotube-Templated Thin Layer Chromatography Plates. An Analogy to 'The Blind Men and the Elephant.' *Surf. Interface Anal.* **2013**, *45*, 1273–1282.

The following figures were other work done that was not included in publications or soon to be published papers.

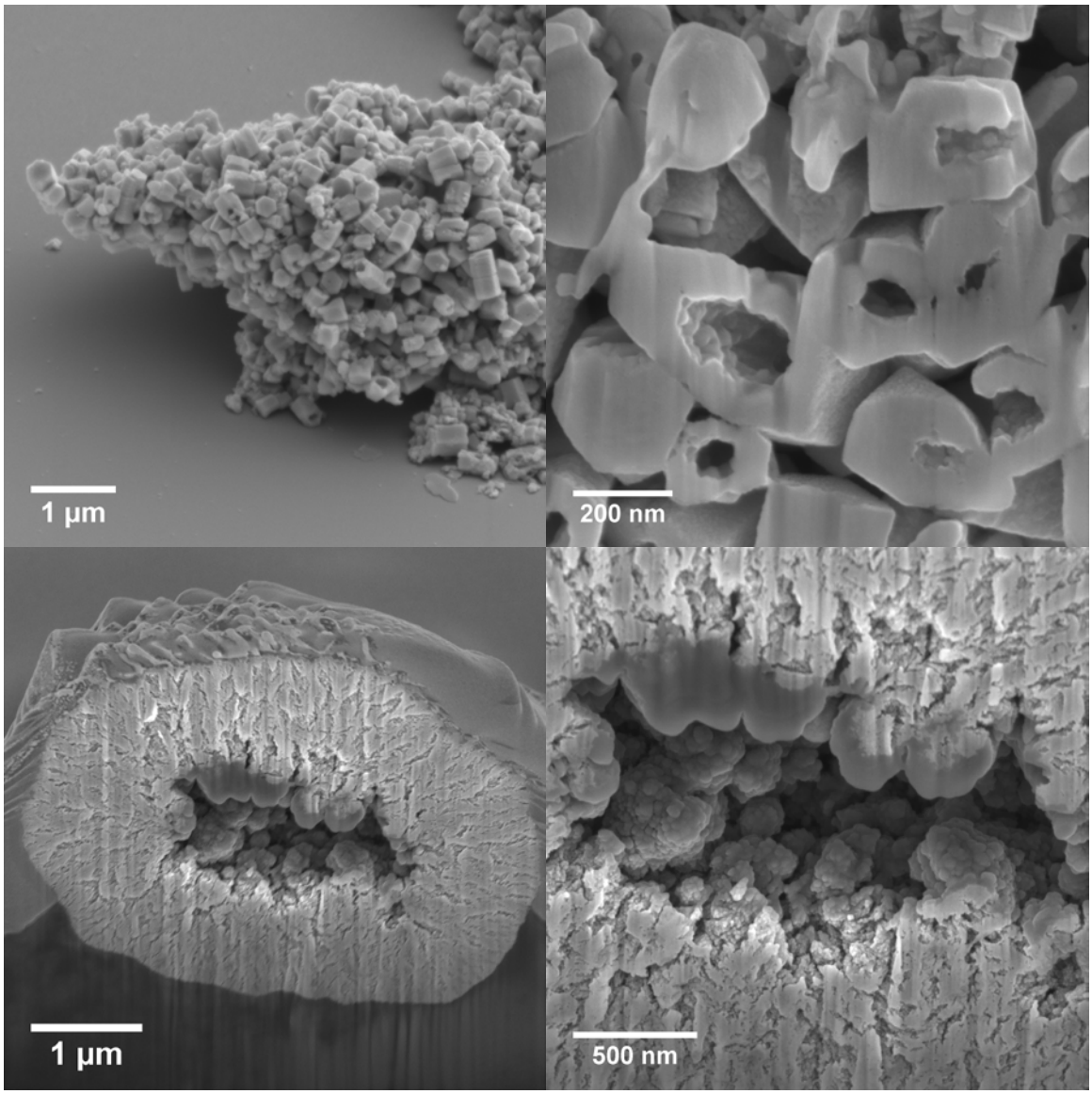

Figure 4. Focused ion beam milling of ZnO structures showing hollow cavities in each structure. Hexaganol prims (top) and spheres (bottom)

During the synthesis carried out in Chapter 3, some of the hexagonal prisms were shown to be hollow. We used an ion beam mill to cut away a cross section of material in both the prisms and the hollow spheres to show similarities and differences. The spheres shown in the bottom of Figure 4 were synthesized by the method described in Chapter 2 and coated with Pt/Au mixture before milling.

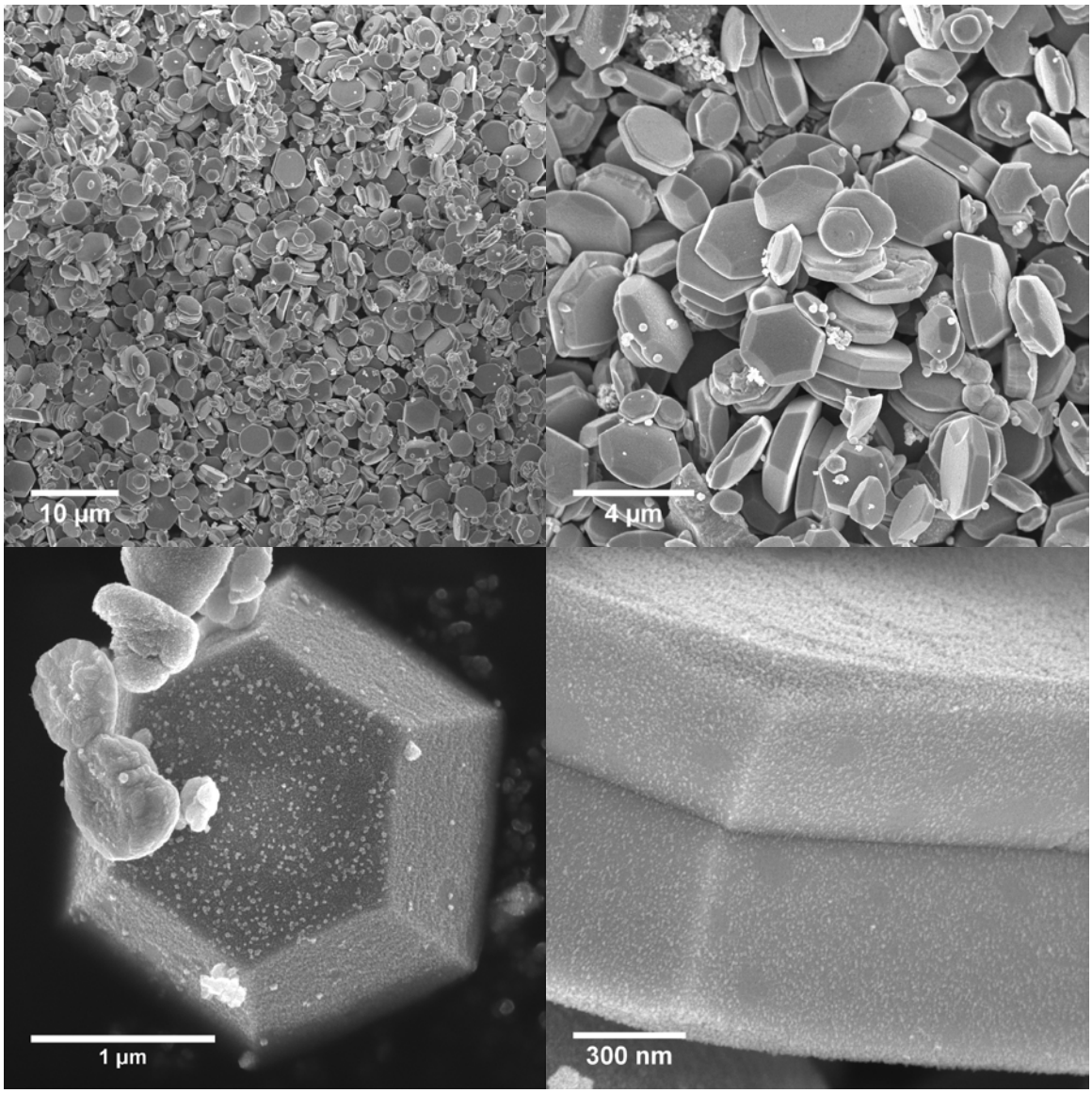

Figure 5. SEM images of hexagonal plates grown in a methanol/water solution with zinc acetate and heat.

Figure 5 images show hexagonal plates that were grown by modifying the procedure detailed in Chapter 2. The synthesis was modified by using a 50/50 solution of water/ethanol to dissolve the zinc salt. Figure 6 images are the same plates seen with TEM. Nanoparticles were found to align themselves to a large degree within the structure seen by the distinct dots in the diffraction pattern, but with distinct particles seen in the TEM as well as blurring in the diffraction pattern to confirm a slight variation in nanoparticle orientation within the structure.

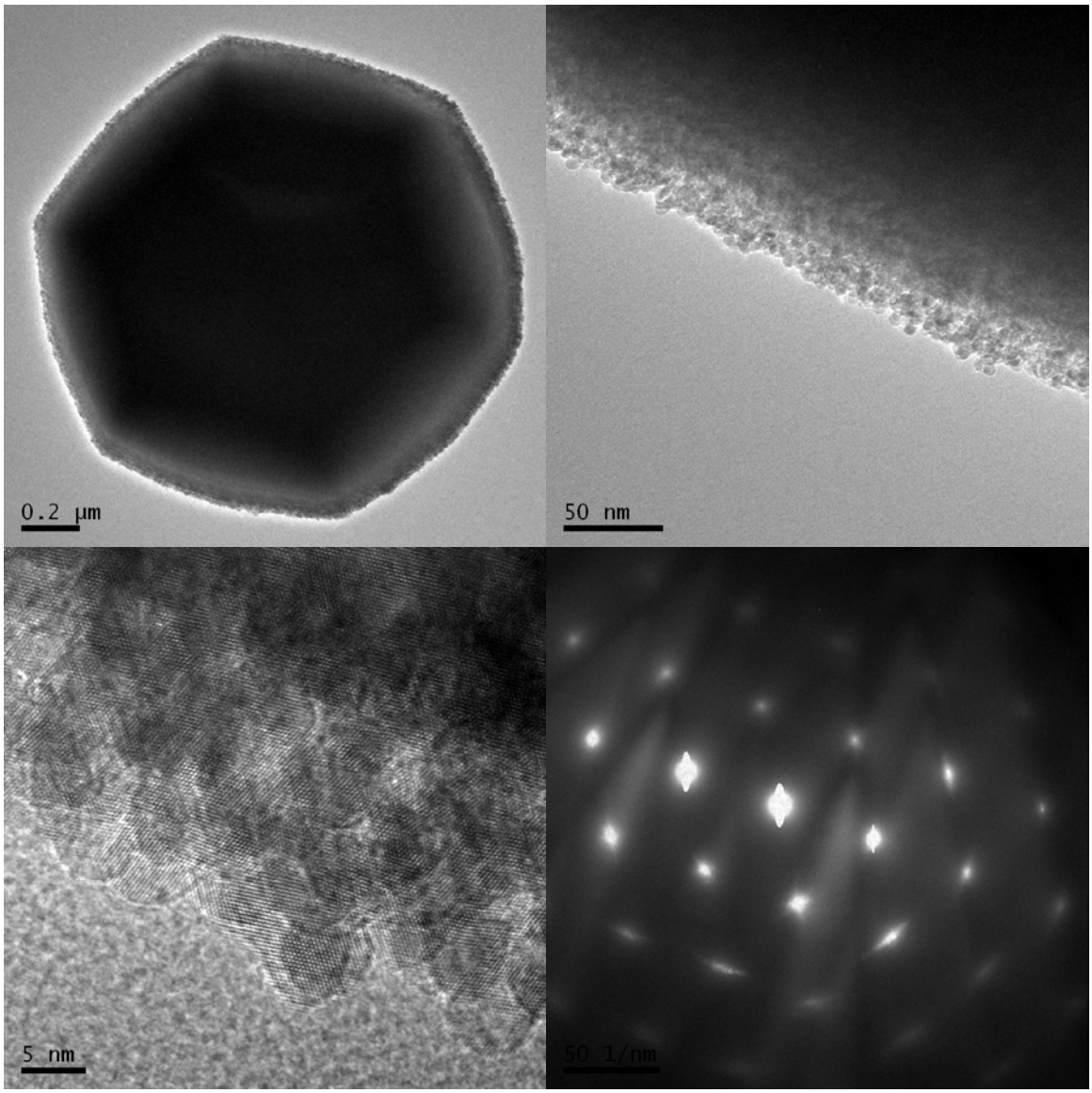

Figure 6. TEM images of hexagonal plates showing nanoparticle alignment with a diffraction pattern of a single crystal with blurring due to dislocation of nanoparti

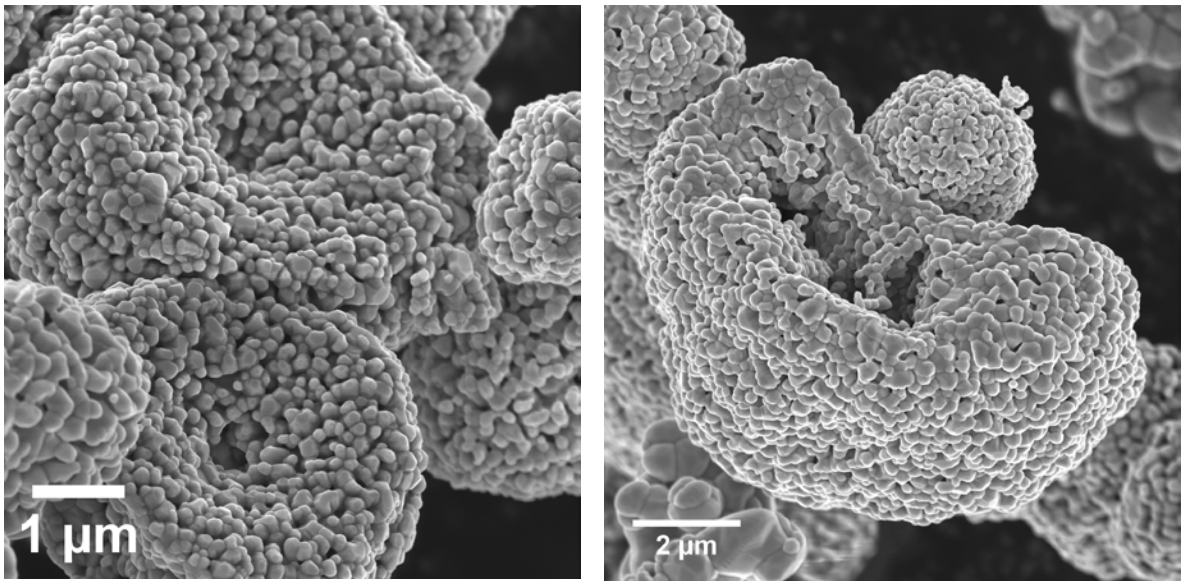

Figure 7. SEM images of ZnO sphere heated to 1000 ˚C to investigate thermal stability.

The ZnO hollow spheres prepared in Chapter 2 were heated at various temperatures to determine their stability and future use in catalytic applications. The material was heated at 100 degree intervals and an XRD analysis was performed. XRD showed growth of then nanoparticles but the material kept its ZnO hexagonal wurtzite cyrstal structure. Figure 7 are SEM images of the spheres after being heated to 1000 ˚C.

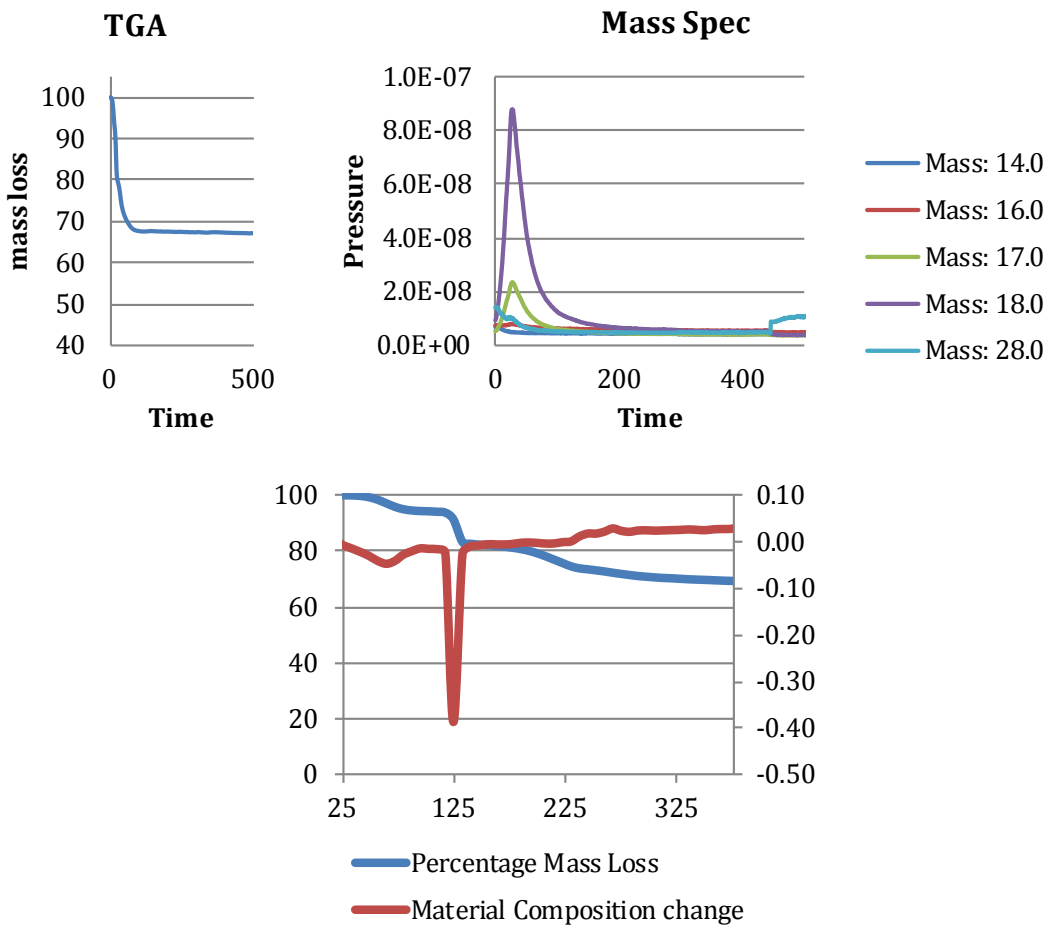

Figure 8. TGA of air dried gel showing a 33% water loss (top) and material change from zinc hyrdoxide acetate to zinc oxide at 125 ˚C (bottom).

Thermogravimetric analysis (TGA) was used to determine the amount of water in the air-dried samples as well as when the chemical change to ZnO would occur. Mass spectrometry analysis of the gases given off during heating confirms the water content.